Air Force Institute of Technology

AFIT Scholar

Theses and Dissertations

Student Graduate Works

3-9-2009

Retroreflector for Photonic Doppler Velocimetry

Thomas J. Lagoski

Follow this and additional works at: https://scholar.afit.edu/etd

Part of the Electromagnetics and Photonics Commons

Recommended Citation

Lagoski, Thomas J., "Retroreflector for Photonic Doppler Velocimetry" (2009). *Theses and Dissertations*. 2468.
https://scholar.afit.edu/etd/2468

This Thesis is brought to you for free and open access by the Student Graduate Works at AFIT Scholar. It has been accepted for inclusion in Theses and Dissertations by an authorized administrator of AFIT Scholar. For more information, please contact richard.mansfield@afit.edu.

Retroreflector for Photonic Doppler Velocimetry

THESIS

Thomas J. Lagoski, Captain, USAF

AFIT/EO/ENG/09-02

DEPARTMENT OF THE AIR FORCE
AIR UNIVERSITY

AIR FORCE INSTITUTE OF TECHNOLOGY

Wright-Patterson Air Force Base, Ohio

APPROVED FOR PUBLIC RELEASE; DISTRIBUTION UNLIMITED.

The views expressed in this thesis are those of the author and do not reflect the official policy or position of the United States Air Force, Department of Defense, or the United States Government.

AFIT/EO/ENG/09-02

Retroreflector for Photonic Doppler Velocimetry

THESIS

Presented to the Faculty

Department of Electrical and Computer Engineering

Graduate School of Engineering and Management

Air Force Institute of Technology

Air University

Air Education and Training Command

In Partial Fulfillment of the Requirements for the

Degree of Master of Science in Electrical Engineering

Thomas J. Lagoski, BSEE

Captain, USAF

March 2009

APPROVED FOR PUBLIC RELEASE; DISTRIBUTION UNLIMITED.

AFIT/EO/ENG/09-02

Retroreflector for Photonic Doppler Velocimetry

Thomas J. Lagoski, BSEE
Captain, USAF

Approved:

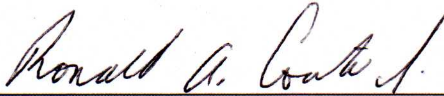

9 Mar 09

Lt Col Ronald A. Coutu, Jr., PhD
(Chairman)

Date

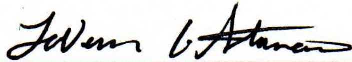

27 Feb 09

Maj LaVern A. Starman, PhD
(Member)

Date

27 Feb 09

Dr. Michael A. Marciniak
(Member)

Date

AFIT/EO/ENG/09-02

Abstract

In order to meet the goals of the Department of Defense (DoD) for smaller and more accurate weapons, the Munitions Directorate of the Air Force Research Laboratory (AFRL/RW) has numerous projects investigating the miniaturization of weapons and munition fuze components. One of these efforts is to characterize the performance of small detonators. The velocity of the flyer, the key component needed to initiate a detonation sequence, can be measured using a photonic Doppler velocimeter (PDV). The purpose of this research was to develop a microelectromechanical system (MEMS) device that would act as an optimal retroreflective surface for the PDV. Two MEMS solutions were explored: one using the PolyMUMPs™ fabrication process and one in-house fabrication design using silicon on insulator (SOI) wafers. The in-house design consisted of an array of corner reflectors created using an SOI wafer. Each corner reflector consisted of three separate mirror plates which were self-assembled by photoresist pad hinges. When heated to a critical temperature (typically 140-160 °C), the photoresist pads melted and the resulting surface tension caused each mirror to rotate into place. The resulting array of corner reflectors was then coated with a thin layer of gold to increase reflectivity. Despite the successful assembly a PolyMUMPs™ corner reflector, assembling an array of these reflectors was found to be unfeasible. Although the SOI corner reflector design was completed, these devices were not fabricated in time for testing during this research. However, the bidirectional reflectance distribution function (BRDF) and optical cross section (OCS) of commercially available retroreflective tapes were measured. These results can be used as a baseline comparison for future testing of a fabricated SOI corner reflector array.

Acknowledgements

First and foremost, thank you to my parents for teaching me the value of an education. The sacrifices they made to achieve their academic goals showed me that anything is possible with the right amount of determination and hard work.

To my wife, I could never thank you enough for the love and support you have given me throughout this process. It wasn't always easy, but we managed to make it through together. More importantly, thank you for giving me the greatest gift I could ever receive, our wonderful son. It is truly amazing to see him discover this world one small piece at a time. I cannot imagine life without his smile.

To all of my instructors, thank you for sharing your wisdom with me. Special thanks to the members of my committee. To Dr. Michael Marciniak, thank you for giving me the optics knowledge needed to complete this research. In addition, as academic advisor you helped me navigate through the electro-optics program, which is not always the simplest task. To Maj LaVern Starman, thank you for sharing your MEMS expertise. Your dedication to your students and the microelectronics program is really astounding. Last, but definitely not least, thank you to my thesis advisor, Lt Col Ronald Coutu. Thank you for giving me the freedom to explore my ideas, but never letting me lose focus of the final goal.

Finally, thank you to my fellow students. There is no way I could have finished this program without you. More specifically, thanks to everyone in the MEMS group. I could not have asked for a more selfless group of peers. I have relied on each of you for guidance at some point in my research, and not once was I denied your help.

Thomas J. Lagoski

Table of Contents

Page

Abstract iv

Acknowledgements v

Table of Contents vi

List of Figures ix

List of Tables xii

List of Symbols xiii

List of Abbreviations xv

I. Introduction 1
  1.1 Motivation 1
  1.2 Objectives 2
  1.3 Contributions 3

II. Theory and Review 5
  2.1 Velocimetry Techniques 5
    2.1.1 Velocity Interferometer System for Any Reflector 5
    2.1.2 Fabry-Perot 7
    2.1.3 Photonic Doppler Velocimeter 7
  2.2 Radiometric Terms 10
    2.2.1 Solid Angle 10
    2.2.2 Radiometric Quantities 11
    2.2.3 Types of Surface Reflection 12
  2.3 Retroreflector Testing Methods 12
    2.3.1 Optical Cross Section 13
    2.3.2 Bidirectional Reflectance Distribution Function 15
  2.4 MEMS Fabrication Techniques 17
    2.4.1 Surface Micromachining 17
    2.4.2 Bulk Micromachining 18
    2.4.3 Microforming 18
    2.4.4 Silicon on Insulator 19
  2.5 MEMS Fabrication Tools 19
    2.5.1 Photoresist Application and Optical Lithography 20
    2.5.2 Deep Reactive Ion Etching 20

Page

2.5.3 Atomic Force Microscopy 22
2.5.4 Metal Sputtering 22
2.6 Possible Retroreflector Solutions 23
2.6.1 Retroreflective Tape 23
2.6.2 Metal Deposition on Commercial Retroreflectors 24
2.6.3 PolyMUMPs™ MEMS 26
2.6.4 Silicon on Insulator (SOI) Fabrication 28
2.7 Chapter Summary 32

III. Theoretical Analysis and Fabrication 33
3.1 Retroreflective Tape Designs 33
3.1.1 Spherical Element Retroreflective Tape Samples 33
3.1.2 Corner Element Retroreflective Tape Samples 34
3.2 Metal Deposition on Retroreflective Tape and Reflectors 35
3.3 MUMPs© Corner Reflector Design 36
3.3.1 MUMPs© Hinge Design 38
3.3.2 MUMPs© Residual Stress Help-Flip Cantilevers 40
3.3.3 MUMPs© Hinge Lock Mechanism 41
3.4 MUMPs© Corner Reflector Fabrication 43
3.5 SOI Corner Reflector Design 46
3.5.1 Triangular Corner Reflector Layout 46
3.5.2 Enhancements to Improve Basic Design 48
3.5.3 Surface Tension Self-Assembly Model 51
3.6 SOI Corner Reflector Fabrication 56
3.6.1 SOI Wafer 56
3.6.2 Device Layer Fabrication 57
3.6.3 Hinge Layer Fabrication 57
3.6.4 Release and Self-Assembly 59
3.6.5 Gold Sputter Coat 60
3.7 Factors Effecting Reflectivity of MEMS Corner Reflectors 60
3.7.1 Losses Due to Etch Holes 61
3.7.2 Losses Due to Surface Roughness 65
3.8 Optical Measurement Methodology 69
3.8.1 Optical Cross Section Methodology 69
3.8.2 Bidirectional Reflectance Distribution Methodology 72
3.9 Chapter Summary 72

Page

IV. Results and Analysis 74
  4.1 MUMPs© Mirror Curvature Measurements 74
  4.2 Roughness Measurements of PolyMUMPs™ and Sputtered Gold Layers 76
  4.3 Optical Cross Section Measurements 78
    4.3.1 OCS of Retroreflective Tapes 78
    4.3.2 OCS of Gold Plated Reflector 79
    4.3.3 OCS of PolyMUMPs™ Corner Reflector 81
    4.3.4 OCS of SOI Triangular Corner Reflectors 81
  4.4 Bidirectional Reflectance Distribution Measurements 81
    4.4.1 BRDF of Retroreflective Tapes 81
    4.4.2 BRDF of Gold Plated Reflector 84
    4.4.3 BRDF of PolyMUMPs™ Corner Reflector 86
    4.4.4 BRDF of SOI Triangular Corner Reflectors 86
  4.5 Analysis of the Retroreflective Tape Protective Coatings 86
  4.6 Chapter Summary 89

V. Conclusions 90
  5.1 Conclusions 90
  5.2 Follow-on Work 91

Bibliography 94

List of Figures

Figure		Page
2.1	Michelson and Fabry-Perot interferometers	6
2.2	Photonic Doppler velocimeter layout illustration	8
2.3	Photonic Doppler velocimeter design with the 3-port circulator	9
2.4	Comparison of Fabry-Perot and photonic Doppler velocimeter setups	10
2.5	Depiction of the planar angle and the solid angle	11
2.6	Specular and diffuse reflection	13
2.7	Light interaction with matter	15
2.8	Geometry of the BRDF	17
2.9	BRDF models for specular, diffuse, and retroreflective materials	17
2.10	MEMS fabrication techniques	19
2.11	Silicon on insulator (SOI) wafer illustration	20
2.12	Schematic of optical shadow contact printing	21
2.13	Reactive ion etching illustration	21
2.14	Metal sputtering illustration	23
2.15	Ray trace through spherical and corner retroreflectors	24
2.16	Retroreflective tape samples at increasing magnifications	25
2.17	Telemecanique RF30 round retroreflector	25
2.18	Cross sectional layout of the PolyMUMPs™ process	26
2.19	MUMPs© corner cube reflector before and after assembly	27
2.20	MUMPs© hinge lock mechanism	28
2.21	Self-assembly process sequence for SOI structures	30
2.22	Improved SOI hinge structure using keying holes	31
2.23	SOI corner reflector mask layout and completed device	32
3.1	Illustration of reflective tape element geometries	33
3.2	Reflective tape samples used	34
3.3	Backside view of reflective tapes	35

Figure		Page

3.4 Sputtering gold onto RF30 reflector 36
3.5 MUMPs© corner reflector layouts. 37
3.6 MUMPs© rotating mirror curvature model 38
3.7 Cross section of MUMPs© hinge 40
3.8 MUMPs© corner reflector hinge design 40
3.9 PolyMUMPs™ mirror help-flip cantilever. 41
3.10 MUMPs© mirror hinge lock mechanisms. 42
3.11 Close-up and model of MUMPs© hinge lock mechanism 43
3.12 Unhinged MUMPs© corner reflector locking mechanism 44
3.13 Failure of the hinged style locking mechanism 45
3.14 Assembled MUMPs© corner reflector 45
3.15 Assembled MUMPs© corner reflector locking mechanisms 46
3.16 An example triangular corner reflector 47
3.17 Triangular corner reflector layout design process 49
3.18 SOI triangular corner reflector designs 50
3.19 Two-dimensional geometry for surface tension powered self-assembly 52
3.20 Variation of pad height with final angle 54
3.21 Geometry of simple trapezoid model 55
3.22 Four triangular corner reflector sizes 56
3.23 Masks used for patterning of SOI devices 58
3.24 SOI device after DRIE and hinge deposition 59
3.25 MEMS micromirror etch hole layout 61
3.26 Amplitude transmittance functions for MEMS micromirrors 62
3.27 Diffraction pattern of a square flat mirror 64
3.28 Diffraction pattern of a square mirror with etch holes 65
3.29 Example cross section of a surface profile measurement 68
3.30 Optical cross section (OCS) measurement setup 69
3.31 Reflected power and irradiance charts for OCS setup 70

Figure | Page

3.32 CASI BRDF measurement setup 73

4.1 MUMPs© mirror curvature measurements 75

4.2 Cross section of MUMPs© mirror curvatures 75

4.3 Gold layer surface profile cross sections 77

4.4 OCS data for retroreflective tapes and gold sputtered reflector . . . 80

4.5 BRDF of Telemecanique RF7590 retroreflective tape 82

4.6 BRDF of Telemecanique RF7610 retroreflective tape 82

4.7 BRDF of Telemecanique RF3870 retroreflective tape 83

4.8 BRDF of 3M 3000X retroreflective tape 83

4.9 BRDF of Telemecanique XUZB11 retroreflective tape 84

4.10 BRDF density plots of Telemecanique RF7590 and RF7610 85

4.11 BRDF of gold coated Telemecanique RF30 reflector 85

4.12 BRDF density plots of Telemecanique XUZB11 and gold coated RF30 86

4.13 Specular reflectance curve for Telemecanique RF7590 87

5.1 Effective area of trihedral corner reflector 92

List of Tables

Table		Page
2.1	Radiometric quantities	12
3.1	Retroreflective tape sample characteristics	35
3.2	Triangular corner reflector design dimensions.	56
3.3	Theoretical loss components for mirrors with varying etch hole dimensions and constant etch hole spacing.	66
3.4	Theoretical loss components for mirrors with varying etch hole spacing constant etch hole dimension.	66
4.1	Gold layer surface roughness measurements	76
4.2	Indexes of refraction for retroreflective tape protective coatings	88

List of Symbols

Symbol		Page
f_0	laser light frequency	8
f_d	Doppler-shifted light frequency	8
f_b	beat frequency	8
v	velocity of moving target	8
c	speed of light	8
λ_0	laser wavelength	8
Ω	solid angle	10
$\theta_{1/2}$	half-angle	11
Φ_e	radiant flux	11
I_e	radiant intensity	11
E_e	radiant irradiance	12
M_e	radiant exitance	12
L_e	radiance	12
σ	optical cross section	14
I_{e-refl}	radiant intensity reflected by a target	14
E_{e-tar}	uniform irradiance at a target	14
σ_{tar}	optical cross section of a target	14
Φ_{e-refl}	radiant flux reflected by a target	14
Ω_{refl}	solid angle into which radiant flux is reflected off a target	14
a_{tar}	radius of target	14
a_{rcv}	radius of receiver collecting aperture	14
L_o	radiance reflected off a surface	16
E_i	radiant irradiance incident upon a surface	16
$d\Omega_i$	differential solid angle	16
L_i	radiance incident upon a surface	16
F_γ	surface tension force	51

Symbol Page

F_p force due to Laplace pressure 51

θ_e equilibrium rotation angle 51

γ surface tension coefficient 52

T_γ torque per unit length due to the surface tension force 52

P Laplace pressure 52

T_p torque per unit length due to Laplace pressure 52

η normalized pad height 53

T_0 initial meltable pad torque 54

T_f torque due to weight of micromirror 54

t_A amplitude transmittance function 62

R_{spec} specular surface reflectance 67

R_0 total surface reflectance 67

δ root-mean-square surface roughness 67

δ_{AV} average root-mean-square surface roughness 68

κ curvature 74

R_s reflectance for s-polarized light 87

R_p reflectance for p-polarized light 87

θ_B Brewster's angle 87

List of Abbreviations

Abbreviation		Page
PDV	Photonic Doppler Velocimetry	1
AFRL	Air Force Research Laboratory	1
LEEFI	Low Energy Exploding Foil Initiator	1
MEMS	Microelectromechanical Systems	2
VISAR	Velocity Interferometer System for Any Reflector	5
HetV	Heterodyne Velocimeter	7
OCS	Optical Cross Section	13
BRDF	Bidirectional Reflectance Distribution Function	13
TOCS	Total Optical Cross Section	14
DOCS	Differential Optical Cross Section	14
SOI	Silicon on Insulator	17
LIGA	Lithography, Galvanoformung, and Abformung	18
SIMOX	Separation by Implantation of Oxygen	19
RIE	Reactive Ion Etching	20
RF	Radio Frequency	20
DRIE	Deep Reactive Ion Etching	21
SPM	Scanning Probe Microscopy	22
AFM	Atomic Force Microscopy	22
COTS	Commercial-Off-The-Shelf	23
MUMPs©	Multi-User MEMS Processes	26
LPCVD	Low Pressure Chemical Vapor Deposition	26
PSG	Phosphosilicate Glass	26
HF	Hydrofluoric Acid	30
rms	root-mean-square	67
POCS	Perceived Optical Cross Section	71
CASI	Complete Angle Scatter Instrument	72

RETROREFLECTOR FOR
PHOTONIC DOPPLER VELOCIMETRY

I. Introduction

The goal of this research project is to develop a simple optical device to provide retroreflection for a photonic Doppler velocimetry (PDV) system. The device must be optimized for a wavelength of 1550 nm and be able to provide a coherent, planar return of the incident light. This device should be a rigid, small (1 mm^2 to 5 mm^2), planar surface that can be stuck to a curved surface without losing its shape.

1.1 Motivation

The sponsor for this research is the Munitions Directorate of the Air Force Research Laboratory (AFRL). They have been using a PDV system to perform velocity measurements of small detonators. The goal of this project is to create a retroreflective surface optimized for the PDV laser wavelength (1550 nm) used by the sponsor.

Currently, AFRL's PDV employs a single-channel (and therefore single-axis) setup. A retroreflective surface (such as a corner mirror) reflects all incoming rays along their original direction. The purpose for using a retroreflector with the PDV system is to allow the addition of two more PDV channels along two additional axes. With a total of three independent PDV channels, it would be possible to extract triaxial velocity measurements of the target.

There are three main requirements for the retroreflector device. First, the retroreflector must be optimized for a wavelength of 1550 nm. This is the wavelength currently used by the Munitions Directorate's PDV system. Second, the entire retroreflector device (including packaging) must be small (1 mm^2 to 5 mm^2). This size requirement is driven by the intended application. These retroreflectors will be attached to a small detonator such as a Low Energy Exploding Foil Initiator (LEEFI). However, they may also be attached to curved surfaces such as bomb bodies with a

superglue-like adhesive. In this case, the device must be small in order to accurately represent the tangent of this curved surface. The final requirement is that the retroreflector provide a coherent, planar return of the incident light. More importantly, a perfect retroreflector would reflect all the incident light back to its source, minimizing any unwanted specular or diffuse reflections. These unwanted reflections could lead to crosstalk between the three PDV channels, reducing velocity measurement accuracy.

1.2 Objectives

The primary objective of this research is to find a reasonable retroreflector design that can be attached to a small, flat surface. A reasonable design must meet the device requirements stated in the previous section. However, it must also be sufficiently robust in order to survive the high accelerations and velocities found in detonation events.

This thesis focusses on four possible solutions in order to meet the above requirements. The first is to apply commercially available retroreflective tapes to a rigid surface. These tapes are typically inexpensive, and therefore expendable. This makes them ideal for small detonator testing since any device used would be susceptible to damage. However, these tapes may not perform as well as a more expensive solution.

Another possible inexpensive solution would be to use commercially available reflectors. These reflectors are often made of plastic corner cube arrays. Depositing a thin layer of gold on these reflectors can significantly improve their retroreflective capabilities.

Because of their small size, microelectromechanical systems (MEMS) are an obvious choice. In addition, MEMS are typically attached to a rigid substrate, satisfying the requirement for the device to remain flat. MEMS corner mirrors have been designed and fabricated in many different configurations. In this research, surface micromachining is used to create MEMS corner mirrors. Surface micromachining is a process where structural layers are deposited and etched on top of the silicon sub-

strate. MEMS mirrors can be built by creating a flat polysilicon surface under a reflective metallic layer. These mirrors can then be released and assembled in a way that creates a corner reflector.

An additional MEMS solution can be created using silicon on insulator (SOI) wafers. With these wafers, it is possible to create rotating mirrors out of the top layer of silicon. These mirrors can then be rotated out of the substrate plane to create corner reflectors.

In this research, the four above solutions are acquired or fabricated, then tested to determine which solution best meets the sponsor's needs. In order to do this, appropriate optical testing techniques are determined. Two optical tests are used to measure the retroreflection of each device in such a way that the performance of each device can be compared. Optical cross section (OCS) measurements provide retroreflection data as a function of incident beam angle. Secondly, bidirectional reflectance distribution function (BRDF) data for each device unveils any specular or diffuse reflections which could lead to crosstalk between channels of the triaxial PDV setup.

1.3 Contributions

In this work, several significant contributions have been made. First, a MUMPs© corner reflector has been designed, fabricated, and assembled. Achieving this required reliable hinge structures to allow the mirrors to rotate out of plane. Locking mechanisms were also designed to hold the mirrors in place once rotated into position. Both of these mechanisms worked as designed to create a MUMPs© corner reflector.

Second, an SOI corner reflector has been designed. The corner of this design is in the substrate plane, while the three mirrors are rotated out of the substrate plane. This allows for maximum three-bounce retroreflection from an incident beam normal to the substrate. Most MEMS corner reflectors (like the MUMPs© reflector discussed previously) are built with one mirror anchored to the substrate, and two

mirrors rotating 90° out of the substrate plane. This creates a corner reflector with maximum three-bounce retroreflection 45° from the surface normal. This new SOI design allows the device to provide maximum retroreflection normal to the surface which it is attached.

Factors effecting the reflectivity of MEMS micromirrors are also explored. Surface roughness measurements are made for the PolyMUMPs™ gold layer and a sputtered gold deposition layer. Reflectivity loss due to these roughness measurements is calculated. Losses due to etch holes are also calculated. These etch hole losses are caused by diffraction as well as the loss of mirror surface area.

Finally, optical measurements are used to characterize retroreflectivity. These tests can be repeated for additional MEMS retroreflector design iterations.

II. Theory and Review

This work combines ideas from the fields of optics and microelectronics. This section reviews the theories from both fields which are used in this research. The principles of velocimetry in shock physics are introduced first, followed by the testing methods employed in this work. Next, microelectronic fabrication techniques and structures are briefly discussed. Finally, the retroreflector solutions explored in this research are presented.

2.1 Velocimetry Techniques

Laser-based velocimetry is an important measurement technique in the world of shock physics. Optical velocimeters using laser Doppler shift were first used in this field in the 1960s, soon after the invention of the laser [28]. The Doppler shift is the difference between the frequency at which sound or light waves leave a source and the frequency seen by the observer. This difference is caused by the relative motion between the source and observer. Laser light reflected off a stationary surface has the same frequency (or wavelength) as the incident light. If the surface is moving, a Doppler shift occurs, changing the frequency of the reflected light. As the surface moves, this shift in frequency of the reflected light is proportional to the velocity of the illuminated surface. A greater Doppler shift corresponds to a greater frequency change, indicating a larger surface velocity [15].

The range of velocities measured in shock physics often exceed 1000 m/s [36]. To measure velocities in the kilometer-per-second range, three techniques are typically used. These techniques, which will be discussed in the following sections, are the Velocity Interferometer System for Any Reflector (VISAR), the Fabry-Perot based system, and the PDV.

2.1.1 Velocity Interferometer System for Any Reflector. A VISAR uses the concept of interferometry to measure velocity. An interferometer is any optical device which utilizes the effect of interference. A simplified illustration of a common

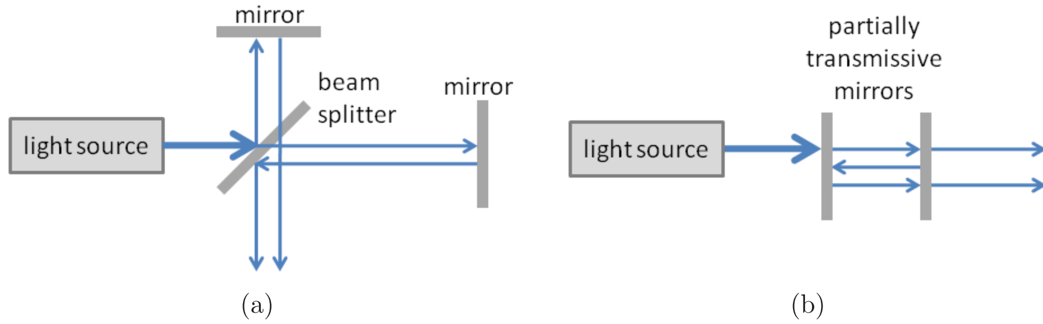

Figure 2.1: Illustrations of (a) a Michelson interferometer and (b) a Fabry-Perot interferometer.

interferometer called a Michelson interferometer is shown in Figure 2.1(a). This device starts with a uniform beam of light, which is then split into two beams by a beam splitter. One of the beams is then exposed to some external influence, such as a change in refractive index or any other change in optical path length. Often this influence is created by making one of the mirrors movable. The beams are then recombined through the beam splitter, and the resulting beam can be used for a measurement [31].

The VISAR was the first laser-based velocimetry technique to be used in the field of shock physics. The first VISAR consisted of an unequal leg Michelson interferometer in which monochromatic light reflected off a target is split and traverses two legs. One of the legs had a longer or shorter delay time depending on the movable mirror so that interference was produced when the beams were recombined at the beam splitter. The interferometer then measured the Doppler-induced changes in frequency of the light beam reflected off the moving target. This system was able to achieve accuracies of 2% or better for peak surface velocities of 200 m/s [3].

The laser interferometer used in a VISAR requires very precise alignment and adjustment of the optical elements. Most VISARs are built on optical tables and use commercial mounts for the optical components. Frequent adjustment of these components is required in order to maintain good interference signals. A simplified VISAR system was created that used a fixed cavity design in which the critical elements were aligned and then fixed so that no further adjustment was necessary [38]. While this

system was easier to operate, fixing the critical elements meant it only allowed for a narrow range of velocity measurements. Because of their size, VISAR systems are not easily portable, and the optics used are susceptible to misalignment [6].

2.1.2 Fabry-Perot. A Fabry-Perot interferometer consists of two parallel, partially transmissive mirrors, allowing multiple round trips of light. Figure 2.1(b) shows a simplified illustration of a Fabry-Perot interferometer. In this depiction, the light source would be the light reflected off the target. This light enters the system from the left and is reflected multiple times by the partially transmissive mirrors of the interferometer. The rays exiting the interferometer are then brought to a focus by a spherical lens onto the slit of a streak camera, which records the fringe motion generated by the interferometer [28].

A Fabry-Perot setup allows the motion of surfaces of reflectivity of at least 1% to be measured with a precision of 0.5%. However, the components required to build a Fabry-Perot setup are costly, complex, require maintenance and operator setup, require a custom-built optical table and occupy a considerable volume. While the Fabry-Perot does provide excellent data, the number of data channels is severely limited by the system's complexity and cost [23]. In addition, the Fabry-Perot mirror spacing must be determined based on the expected acceleration pulse and final velocity of the target.

2.1.3 Photonic Doppler Velocimeter. A photonic Doppler velocimeter, sometimes referred to as a Heterodyne Velocimeter (HetV), uses hardware that was originally developed for the telecommunications industry. PDV setups have been able to measure surface velocities ranging from centimeters per second to kilometers per second by making use of the Doppler shift.

The basic PDV setup was reported by Strand et al. in 2005 [36]. A 1550 nm fiber laser and a single mode fiber deliver the light to and from the target. Figure 2.2 shows a conceptual layout of the velocimeter. At the target end of the fiber, a probe with

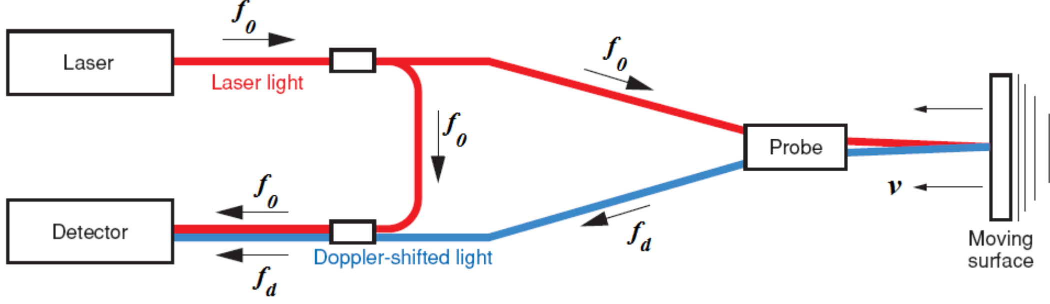

Figure 2.2: The PDV detects the beat frequency between two slightly different frequencies of light . Laser light from the probe, f_0, illuminates the moving surface. The Doppler shifted light, f_d, is then collected by the probe and sent to the detector. At the same time, a portion of the original light is sent to the same detector. The difference between these two frequencies (the beat frequency) can be used to determine to velocity, v, of the moving surface. [15]

a lens focuses the light onto the moving surface and also collects light reflected from the surface. This collected Doppler shifted light is transported back to the detector. At the same time, a portion of the non-Doppler shifted light is also transported to the detector and mixed with the Doppler shifted light from the target.

In Figure 2.2, the laser emits light at a frequency f_0, and the Doppler shifted light is at frequency f_d. The beat frequency generated at the detector is equal to the difference between the Doppler-shifted frequency and the un-shifted light frequency. This frequency, f_b, is given by:

$$f_b = f_d - f_0 = 2\left(\frac{v}{c}\right) f_0 \tag{2.1}$$

Where v is the velocity of the target and c is the speed of light. Since the speed of light is $c = f_0\lambda_0$, where λ_0 is the laser wavelength, the velocity of the moving surface is:

$$v = \left(\frac{\lambda_0}{2}\right) f_b \tag{2.2}$$

For the laser wavelength of 1550 nm, the velocity is then

$$v \text{ (m/s)} = 775 f_b \text{ (GHz)} \tag{2.3}$$

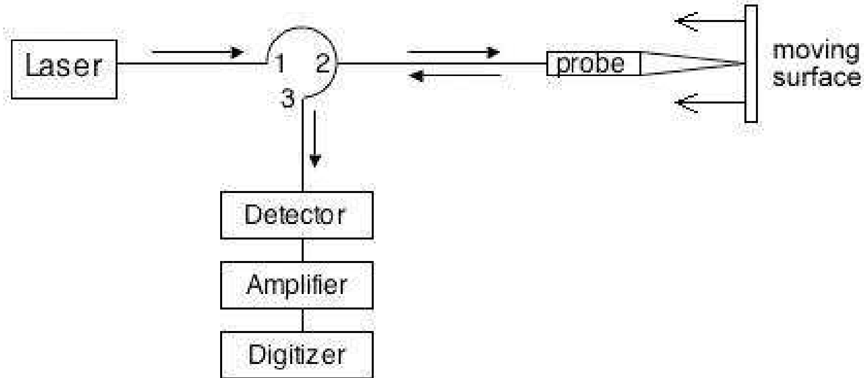

Figure 2.3: PDV design with the 3-port circulator. The 3-port circulator has the property that any light injected into port 1 will be emitted out port 2, and light injected into port 2 will be emitted out port 3. [36]

The PDV utilizes many components from the telecommunications industry. These components have the advantage of being relatively abundant and low-cost. The most important of these components is called a 3-port circulator (see Figure 2.3). A 3-port circulator can separate bi-directional light, allowing the Doppler-shifted light to be separated from the un-shifted light. The un-shifted light that interferes with the Doppler-shifted light is actually obtained from the back-reflectance of the probe. The beat frequency is measured by a high-bandwidth photodiode, connected to a digitizing oscilloscope. For a target moving at 1000 m/s, this beat frequency would be approximately 1.29 GHz [15]. Until recently, recording digitized data at this frequency would be impossible. However, the availability of extremely fast digitizers now make it possible to sample this frequency data. The PDV built by Strand et al. [36] used a digitizer sampling at 20 GHz.

The PDV has several advantages over the VISAR and Fabry-Perot systems discussed previously. First, it is capable of resolving multiple frequencies simultaneously. The maximum target velocity that can be measured is limited only by the recording digitizer. A PDV is a much simpler device to setup and use. Figure 2.4 shows the difference in complexity between a Fabry-Perot setup and a PDV. The PDV is rack-mountable and portable, allowing users to take PDV measurements at remote locations or in the field. Because a PDV is constructed from mostly standard telecom-

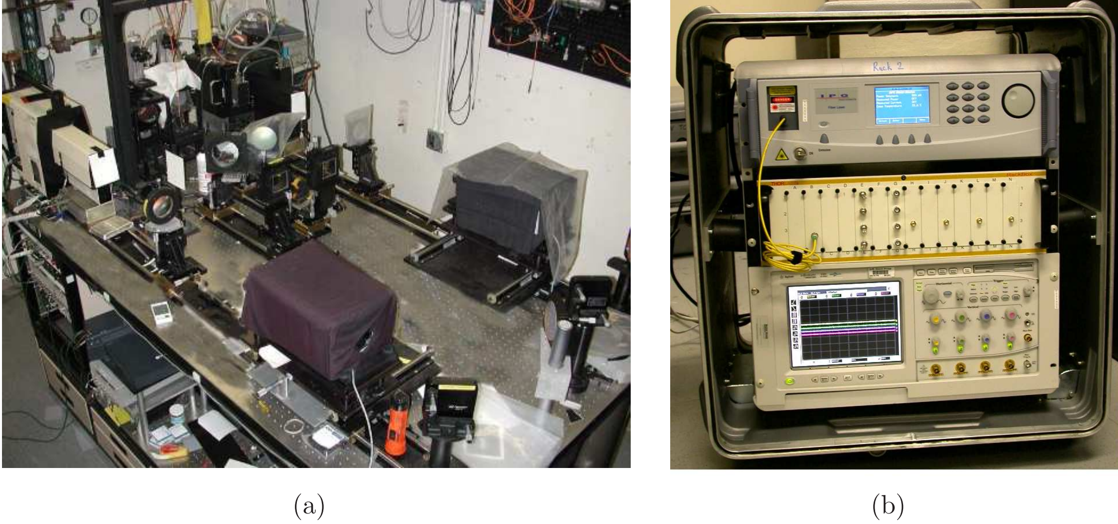

(a) (b)

Figure 2.4: Comparison of Fabry-Perot and PDV systems. (a) The Fabry-Perot setup requires a custom built optical table, occupies a considerable volume, and requires components that are costly and complex. (b) The PDV is contained in a small, rackmount chassis and can be transported and set up much more easily than the Fabry-Perot system. [16]

munications optical fiber components, the cost is relatively inexpensive. The PDV developed by Maisey and Bowden [25] cost approximately $35,000.

2.2 Radiometric Terms

Before discussing the testing methods used in this research, it is first necessary to introduce some key radiometric terms that will be used.

2.2.1 Solid Angle. The solid angle is a key concept in radiometry. To understand the solid angle, it is helpful to think back to radians from planar geometry. In Figure 2.5(a), the two-dimensional angle, θ, is the ratio of the arc length on a circle to the radius, s/r, and is defined in radians (rad). Similarly, in three dimensions [Figure 2.5(b)] the solid angle, Ω, is the ratio of an area on the surface of a sphere to the square of the radius, defined in steradians (sr), or

$$\Omega = \frac{A}{r^2} \text{ (sr)} \tag{2.4}$$

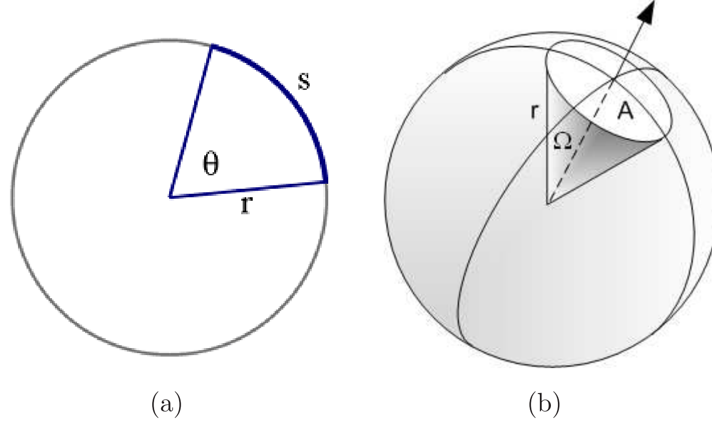

(a) (b)

Figure 2.5: (a) Planar angle θ is measured in radians, and is equal to s/r. (b) Solid angle Ω is measured in steradians, and is equal to A/r^2. [13]

Just as a circle has a circumference of 2π radians, a sphere contains $4\pi r^2/r^2 = 4\pi$ steradians. The cross-sectional area, A, can be written as

$$A = \pi r^2 \sin^2(\theta/2) \tag{2.5}$$

Using the small-angle approximation and substituting in the half-angle, $\theta_{1/2}= \theta/2$, this can be reduced to

$$A \approx \pi r^2 \theta_{1/2}^2 \tag{2.6}$$

Combining Equations 2.4 and 2.6, the solid angle can be rewritten as

$$\Omega \approx \pi \theta_{1/2}^2 \tag{2.7}$$

2.2.2 Radiometric Quantities. In order to measure retroreflection, it is necessary to define the radiometric quantities that will be used when describing radiant sources. These quantities, along with their symbols and units are given in Table 2.1. The basic quantity used is flux, Φ_e, the measure of total power emitted from a source or landing on a particular surface in units of watts. Intensity, I_e, is then defined as power, or flux, per unit solid angle. Intensity is used to specify the amount of radiation emitted from a point source. Light is often measured in terms of flow through

an area, or energy per unit surface area. Irradiance, E_e, is the amount of power per unit area that falls on a surface. Exitance, M_e, is the amount of power per unit area that leaves a surface. Finally, radiance, L_e, describes the amount of light that passes through or is emitted from a particular area, and falls within a given solid angle [8].

2.2.3 Types of Surface Reflection. There are two ways that light reflects off a surface. These two types of reflections, specular and diffuse, are illustrated in Figure 2.6. Specular reflection occurs when light bounces off a very smooth surface. This is the mirror-like reflection most people are familiar with. Specular reflection is characterized by the fact that the incident ray, reflected ray, and surface normal are all in the same plane. Also, the angle made by the incident ray to the normal is the same as the angle made by the reflected ray to the normal. Diffuse reflection occurs when light reflects off a rough surface. Because of microscopic irregularities in the surface, light bounces off in all directions. Most surface reflections are some combination of the specular and diffuse type.

2.3 Retroreflector Testing Methods

To determine which retroreflector solution best suits the sponsor's needs, it is important to make some retroreflectivity measurements. First, it is necessary to determine how far away from the retroreflector's surface normal the incident radiation can illuminate the target and still give an acceptable return. Typically, the amount of light returned to the source decreases as the incident radiation's angle

Table 2.1: Radiometric quantities

Symbol	Quantity	Units
Φ_e	Flux	watt
I_e	Intensity	watt/sr
E_e	Irradiance	watt/cm^2
M_e	Exitance	watt/cm^2
L_e	Radiance	watt/(cm^2 sr)

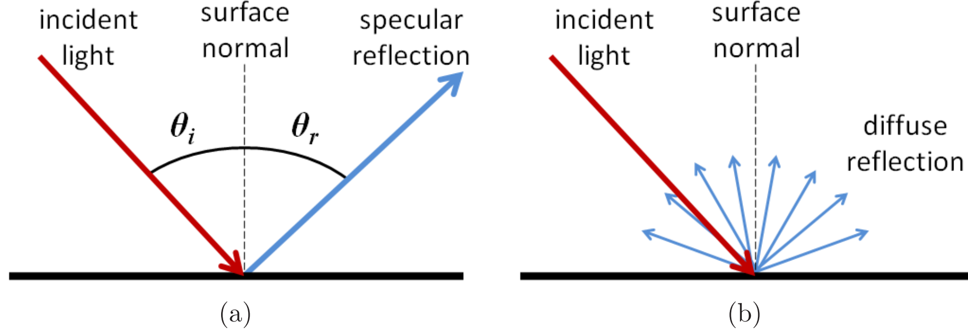

Figure 2.6: (a) Specular reflection reflects the incident ray so that $\theta_i = \theta_r$. (b) Diffuse reflection scatters light in all directions.

from the retroreflector's surface normal increases. At a large enough incident angle, the returned light will be too low to generate a decent beat frequency at the PDV's detector. The optical cross section (OCS) of the retroreflectors can be measured at increasing angles from the surface normal to determine their effective angular range of operation.

A more important measurement for the retroreflectors in this research is the amount of scattering created. Optical scattering refers to the amount of light not reflected in the desired direction. In this case, scattering is any light that is not reflected back to the source. Scattering must be kept to a minimum for a multiple-channel PDV setup in order to reduce crosstalk between channels. Any light that is not reflected back at its source could potentially be reflected at another source, interfering with reflection data in that channel. Scattering from a retroreflector sample can be accounted for by determining its bidirectional reflectance distribution function (BRDF).

The following two sections explain the OCS and BRDF and how they will be used in this research.

2.3.1 Optical Cross Section. A target's OCS describes the light scattered in a given direction when the target is irradiated by a uniform collimated beam [32]. It is comparable to a radar cross section, which is a measure of a target's ability to

reflect energy to a radar receiving antenna [4]. OCS, σ, can be defined as

$$\sigma = \frac{\text{reflected intensity}}{\text{incident irradiance}} = \frac{I_{e-refl}}{E_{e-tar}} \ (\text{m}^2/\text{sr}) \tag{2.8}$$

where I_{e-refl} is the radiant intensity reflected by the target and E_{e-tar} is the uniform irradiance at the target [2]. From Table 2.1 it can be shown that the radiant intensity can also be written as the radiant flux per solid angle, or $I_e = \Phi_e/\Omega$. The OCS of the target, σ_{tar}, then becomes

$$\sigma_{tar} = \frac{\Phi_{e-refl}/\Omega_{refl}}{E_{e-tar}} \tag{2.9}$$

where Φ_{e-refl} is the radiant flux reflected by the target into the solid angle, Ω_{refl}. OCS is written in units of m^2/sr and is a good description of how large a target looks to a detector. OCS can be used to show how retroreflective a material is as its angle from the surface normal is increased.

When measuring the OCS of a target, it is important that the interrogating laser beam meet certain requirements. The beam must be collimated and spatially coherent. If the source is not in the TEM_{00} mode (the fundamental transverse mode of the laser resonator), it must be spatially filtered. Spatial filtering can also be used to improve the beam quality by removing aberrations due to imperfections in the optics or gain medium of the laser. The beam must also be sufficiently uniform, with beam power not deviating by more than 15% of the mean over the entire target area [1].

There are two types of OCS, the total OCS (TOCS) and the differential OCS (DOCS). It is important to know the conditions where each is appropriate. The difference between the TOCS and the DOCS has to do with the power collected by a receiver in the diffraction pattern of the target. The size of the target's diffraction pattern is approximately $\frac{R\lambda}{a_{tar}}$, where R is the distance from the target to the receiver optic and a_{tar} is the radius of the target. If the diffraction pattern is much greater than the radius of the receiver collecting aperture, a_{rcv}, or $\frac{R\lambda}{a_{tar}} \gg a_{rcv}$, the receiver only sees a small fraction of the pattern. This portion of the pattern is essentially

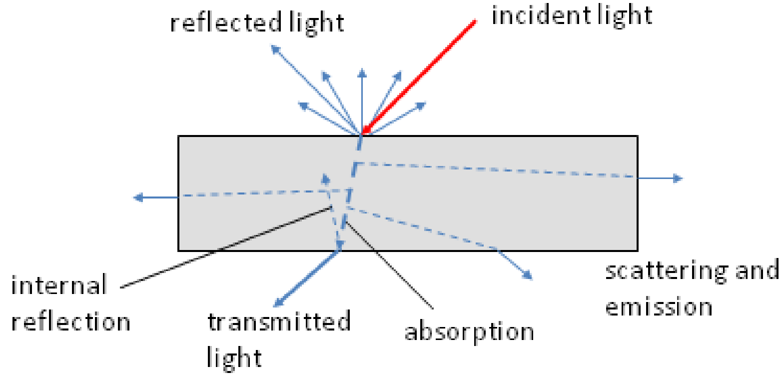

Figure 2.7: Light interaction with matter. Some of the incident light is reflected, some is transmitted, and some is absorbed. [33]

constant over the receiver aperture, and in this case it is appropriate to use the DOCS. On the other hand, if $\frac{R\lambda}{a_{tar}} \ll a_{rcv}$, the TOCS must be used [2].

2.3.2 Bidirectional Reflectance Distribution Function. When light contacts a material, three types of interactions can occur. In Figure 2.7, a portion of the incident light is reflected, some of the light is transmitted, and the rest is absorbed by the material. The reflected light is what an observer sees when viewing an illuminated surface. Different materials reflect incident light in different ways. For instance, a rough opaque material such as sandpaper reflects light differently than a smooth surface like a mirror. The BRDF describes how light is reflected off a material.

The BRDF is a function of the viewer's, as well as the incident light's position relative to the surface normal and tangent. In addition, varying wavelengths of light can reflect off a material differently depending on its physical structure. Because of this, the BRDF is also a function of wavelength. Light also interacts with different regions of a surface. The ring patterns in wood demonstrate that the BRDF for wood varies with surface position [47]. For simplification purposes, the assumption is made that the properties of the materials tested in this research do not vary with surface position ("uniformity assumption"). The BRDF can be written in notation as $BRDF_\lambda(\theta_i, \phi_i, \theta_r, \phi_r)$, where θ_i and ϕ_i represent the incoming light direction in

spherical coordinates and θ_r and ϕ_r represent the outgoing reflected light direction in spherical coordinates.

The BRDF is the ratio of reflected radiance at (θ_r,ϕ_r) to the irradiance on the surface from (θ_i,ϕ_i). If the radiance of reflected light at (θ_r,ϕ_r) is L_o and the irradiance from (θ_i,ϕ_i) is E_i, the BRDF is then

$$BRDF_\lambda(\theta_i, \phi_i, \theta_r, \phi_r) = \frac{L_o(\theta_r, \phi_r)}{E_i(\theta_i, \phi_i)} \ \ (\mathrm{sr}^{-1}) \tag{2.10}$$

Figure 2.8 shows a small surface element, dA, which is illuminated by an incident light. The amount of incident light from (θ_i,ϕ_i) is proportional to the amount of light arriving at the differential solid angle, $d\Omega_i$. The differential solid angle is very small, so the assumption can be made that $d\Omega_i$ is uniformly illuminated by some quantity of light, L_i over its entire region. The total incident light coming through the region is then $L_i d\Omega_i$. This quantity of light can then be projected onto the surface element, dA, as

$$dE_i = L_i(\theta_i, \phi_i) \cos\theta_i \ d\Omega_i \tag{2.11}$$

Combining Equations 2.10 and 2.11, the BRDF can be written in the form

$$BRDF_\lambda(\theta_i, \phi_i, \theta_r, \phi_r) = \frac{L_o(\theta_r, \phi_r)}{\int\limits_{\Delta\Omega_i} L_i(\theta_i, \phi_i) \cos\theta_i \ d\Omega_i} \ \ (\mathrm{sr}^{-1}) \tag{2.12}$$

Because the BRDF can illustrate how objects will look from different angles when illuminated from different directions, it is most often used by the computer graphics industry for realistic scene rendering. Figure 2.9 shows typical BRDF models for generic specular, diffuse, and retroreflective materials. Retroreflectivity of a material can be seen in the BRDF by looking at how much of the reflected signal is directed toward the source. The BRDF is also a good measure of light scattering. The diffuse example shows perfect scattering, as the incident light is reflected in all directions. A good retroreflector will have little to no scattering.

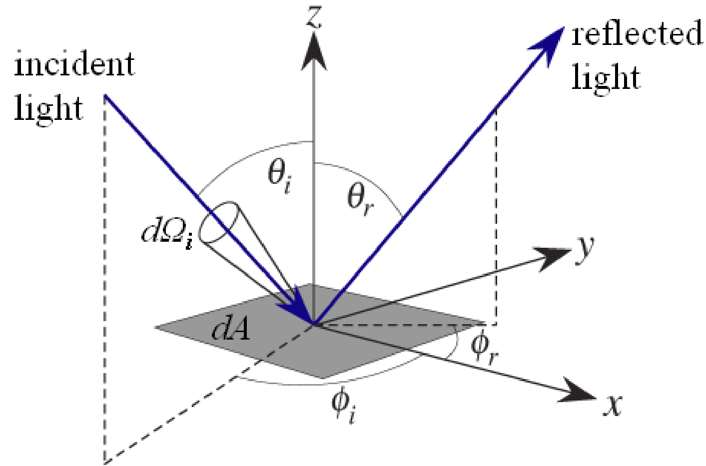

Figure 2.8: Geometry of the BRDF. For a given material, the BRDF relates incident light in a given direction to reflected light along a second direction. [14]

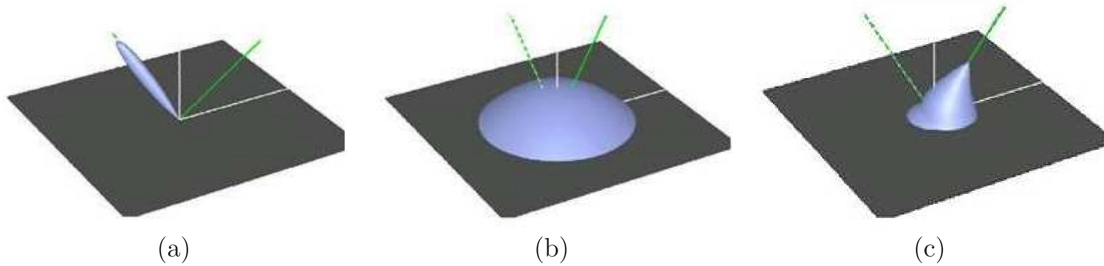

Figure 2.9: BRDF models of generic (a) specular, (b) diffuse, and (c) retroreflective materials. For a retroreflective material, most of the reflected light is directed back at the source. [34]

2.4 MEMS Fabrication Techniques

There are three types of MEMS fabrication processes: surface micromachining, bulk micromachining, and microforming. These processes are briefly discussed in the following sections, along with an introduction to silicon on insulator (SOI) technology.

2.4.1 Surface Micromachining. Surface micromachining is known as an additive process since structural layers are grown on top of the substrate. These layers are then patterned using photolithography, followed by either a wet etch involving an acid or a dry etch using ionized gas or plasma. Surface micromachining can involve as many layers as necessary, but each layer requires a new mask to produce the different

pattern for each layer. To create movable parts, structural layers are separated by sacrificial layers. The sacrificial layers are removed at the end of the fabrication process, releasing the movable structures. An example of a structure fabricated from surface micromachining can be seen in Figure 2.10(a).

2.4.2 Bulk Micromachining. Unlike surface micromachining, bulk micromachining is a subtractive process. Structures built with this process are defined by etching into the substrate. While surface micromachining is used to create structures on top of a substrate, bulk micromachining is used to create structures into a substrate. Like in surface micromachining, the process begins with a substrate which is patterned with photolithography and etched using either a wet or dry etch. In bulk micromachining, a wet etch is typically used to take advantage of the substrate's crystal structure. In a crystal, atoms are arranged periodically in lines and planes. Some planes etch faster than others, which can result in an etch that produces pits with angled walls. The angle of these walls is a function of the substrate's crystal structure. An example of a structure fabricated from bulk micromachining can be seen in Figure 2.10(b).

For this research, it was originally thought that bulk micromachining could be employed to etch trihedral corner reflectors into a substrate. However, as seen in Figure 2.10(b), the pyramidal pits created in bulk micromachining have four sides. None of these sides are orthogonal to their adjacent side. An effective trihedral corner reflector needs three sides, each orthogonal to both adjacent sides.

2.4.3 Microforming. Surface micromachined structures have limited aspect ratios due to the relatively thin layers that can be deposited. In microforming, devices are built on top of the substrate like surface micromachining, but with much larger aspect ratios. One microforming process, called LIGA [lithography, galvanoformung (electroplating), and abformung (molding)], uses thick photoresists as molds which are filled via metal plating processes [19]. These devices typically have thicknesses

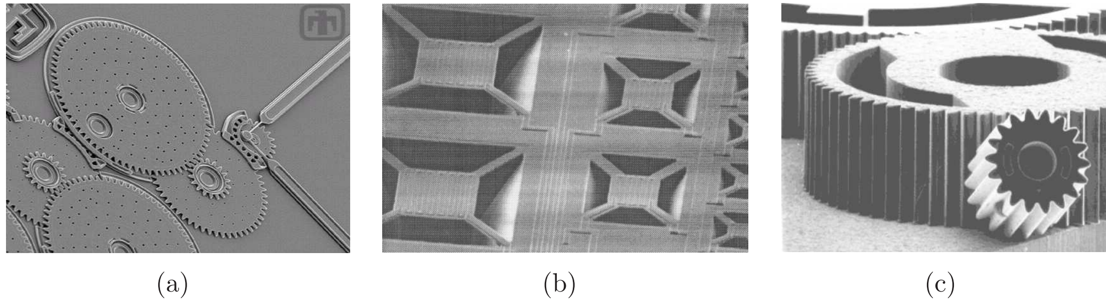

(a) (b) (c)

Figure 2.10: MEMS fabrication techniques. (a) Surface micromachined structures are grown on top of the substrate. (b) Bulk micromachined structures are built by etching away the substrate. (c) Microforming creates high aspect ratio structures. [35]

of 50 μm to 500 μm [12]. An example of a microformed structure can be seen in Figure 2.10(c).

2.4.4 Silicon on Insulator. SOI wafers consist of a thin oxide layer sandwiched between a thick silicon substrate (handle wafer) and a top layer of bonded silicon (device layer). There are two main manufacturing methods for creating SOI wafers: SIMOX and wafer bonding.

Separation by Implantation of Oxygen (SIMOX) uses high-energy ion implantation to place oxygen atoms well below the surface of a silicon wafer. The wafer is then annealed at high temperature to produce a buried oxide layer below the silicon surface [19].

In silicon wafer-to-wafer bonding, a silicon wafer is oxidized to form a SiO_2 layer. A second silicon wafer is then placed in contact with this oxidized surface. The two wafers are annealed at high temperature to form a bond. After bonding, the top silicon layer is thinned by chemical etching until it reaches the desired device level thickness [19]. This type of SOI wafer is illustrated in Figure 2.11

2.5 MEMS Fabrication Tools

This section introduces the MEMS fabrication technologies used in this research.

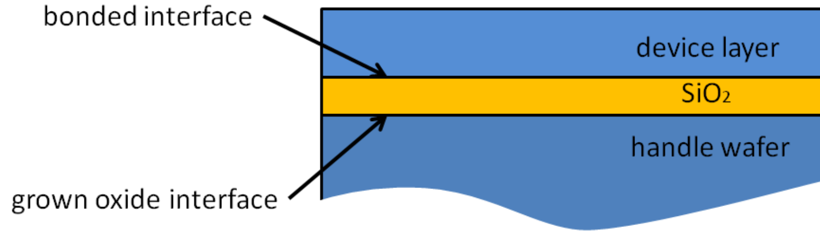

Figure 2.11: Bonded silicon on insulator (SOI) wafer illustration. SiO_2 is grown on the handle wafer which is then bonded to the device layer.

2.5.1 Photoresist Application and Optical Lithography. Before any lithography steps, any contaminants on the wafer surface are removed by a wet chemical treatment. Typically, this involves spraying the wafer with acetone and methanol, then hotplate drying. After cleaning, a uniform layer of photoresist is spun onto the wafer. The photoresist-coated wafer is then prebaked on a hot plate to improve adhesion and to remove any excess solvent. After prebaking, the wafer is placed in a mask aligner and exposed through a mask to high-intensity ultraviolet light (see Figure 2.12). The mask is usually a glass plate with a patterned chrome film on one side. During exposure, the complex pattern of the mask is transferred to the photoresist. For a positive photoresist, any resist that is exposed can then be washed away with a developer solution. For a negative photoresist, any resist that is exposed will stick to the wafer, while any unexposed resist is then washed away with developer. The pattern left in the photoresist leaves openings to the layer beneath the photoresist which can then be etched using various etching techniques.

2.5.2 Deep Reactive Ion Etching. Reactive ion etching (RIE) uses chemically reactive plasma to remove material deposited on a wafer surface or the wafer surface itself. A typical RIE system consists of a vacuum chamber with a top and bottom electrode. The sample wafer sits on the bottom electrode. Gas enters through the top of the chamber and exits through the bottom. A strong radio frequency (RF) electromagnetic field ionizes the gas molecules by stripping them of electrons, creating a plasma in the chamber. These ions then attack the wafer surface. Sulfur hexafluoride

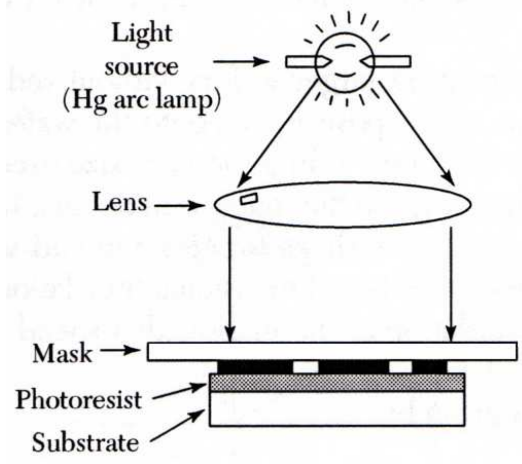

Figure 2.12: Schematic of optical shadow contact printing. The photoresist is exposed to the portion of light that shines through the mask. [27]

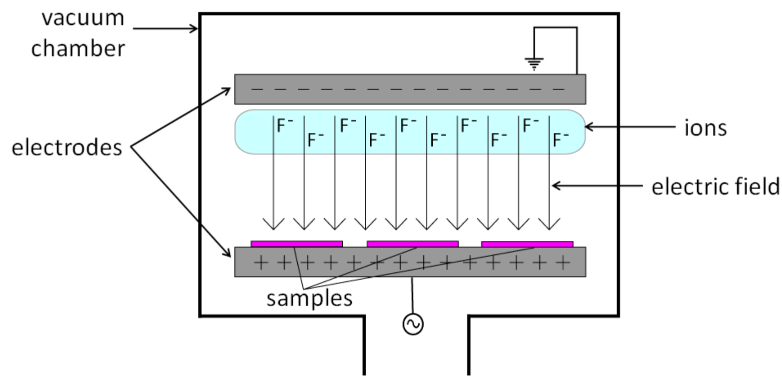

Figure 2.13: Illustration of a typical RIE setup. The two electrodes create an electric field which accelerates ions toward the samples. [9]

(SF_6) is a gas source commonly used for etching silicon in plasma systems [19]. An example RIE illustration is shown in Figure 2.13.

Deep reactive ion etching (DRIE) is used to produce structures with high aspect ratios. This process alternates between etching and polymer deposition phases. The deposited polymers reduce the sidewall etch rate, resulting in vertical sidewalls. A DRIE etches silicon much faster than photoresist and SiO_2. Because of this, an SOI wafer has a built-in etch stop.

2.5.3 Atomic Force Microscopy. Scanning probe microscopy (SPM) is an area of microscopy where a sharp probe is scanned across a surface while the probe/surface interaction is monitored. Atomic force microscopy (AFM) is one type of SPM. AFM consists of three primary modes: contact mode, non-contact mode, and tapping mode.

Contact mode AFM scans a tip attached to a cantilever directly across the sample surface while monitoring the cantilever deflection with a split photodiode detector. In non-contact mode, the cantilever is oscillated at a frequency slightly above the cantilever's resonance frequency. The tip never contacts the sample surface during scanning, but instead oscillates above the adsorbed fluid layer on the surface. The cantilever's resonance frequency is decreased by Van der Waals forces (as well as other long range forces extending above the surface) which causes the amplitude of oscillation to decrease. Tapping mode AFM is similar to non-contact mode, except the cantilever is oscillated below its resonance frequency. When scanning, the tip periodically taps lightly on the sample surface at the bottom of its swing [46].

While contact mode AFM gives a better resolution image, the tip does exert force on the sample surface which leads to scratching. Non-contact mode AFM avoids any scratching, but this typically leads to very low resolution. Tapping mode AFM combines these two modes, giving a high resolution on most samples with no scratching.

2.5.4 Metal Sputtering. Sputter coating is a method of film deposition where material is sputtered, or ejected, from a target and then deposited on a substrate (see Figure 2.14). In the absence of a sputtering gas, the ejected target ions can travel ballistically from the target to the sample in a straight line. At higher gas pressures, the target ions collide with the gas atoms and move diffusely. When sputtering gold, the sputtering gas is typically argon. The atomic weight of the sputtering gas and the target should be close to allow for efficient exchange of momentum. Sputtering films generally have better adhesion to a substrate than evaporated films, and the

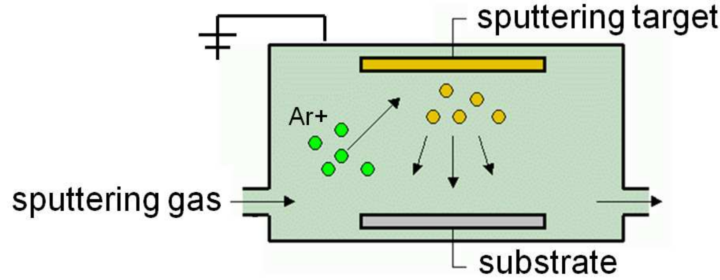

Figure 2.14: Illustration of a metal sputtering setup. Material is sputtered from the target and deposited on the substrate. [26]

process is low temperature. The target atoms provide an even, multidirectional, and conformal coating on the substrate [10].

2.6 Possible Retroreflector Solutions

This thesis will focus on four possible solutions, which will be discussed in detail in the following sections. The first solution is to use commercial-off-the-shelf (COTS) retroreflective tape mounted to a rigid surface. A second solution involves the deposition of a thin reflective metal on a COTS retroreflector. The final two solutions involve fabrication of MEMS corner reflectors using two different processes.

2.6.1 Retroreflective Tape. This solution is really the control experiment in this study. Retroreflective tapes are low-cost and readily available. While they are not rigid, they could easily be attached to a hard, flat surface. The success of the other possible solutions will be dependent on their performance versus these retroreflective tape samples.

There are two main types of retroreflective tape currently on the market. One type is made of very small spherical (often called cat's eye) reflecting elements stuck to the surface of the tape. The principle of operation for these spherical reflectors is shown in Figure 2.15(a). Incident light is bent through the first surface of the sphere, bounces off the back of the sphere, and is then bent back to its original orientation as it leaves the sphere. The other type of retroreflective tape tested is made of small corner

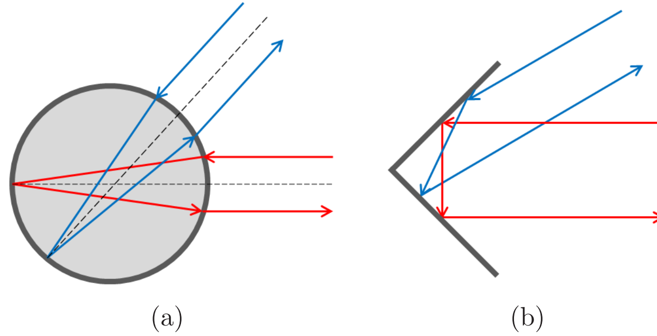

Figure 2.15: Ray trace through (a) a spherical and (b) a corner retroreflector.

elements. The principle of operation for a corner reflector is shown in Figure 2.15(b). Incident light bounces off the surfaces of the corner and is then bent back to its original orientation as it leaves the corner.

Examples of commercially available spherical and corner element retroreflective tapes are shown at increasing degrees of magnification in Figure 2.16. Telemecanique RF3870 retroreflective tape consists of tiny spherical (cat's eye) reflectors imbedded in an adhesive. These spherical elements range in size from approximately 30-70 μm in diameter. 3M 3000X tape is made of tiny triangular-faced trihedral corner elements measuring about 210 μm on each side.

2.6.2 Metal Deposition on Commercial Retroreflectors. Most COTS retroreflectors are made of two plastic pieces. One piece is usually an array of small, transparent plastic corner cubes as shown in Figure 2.17(a). The other piece is an opaque flat plate. The transparent piece is fixed to the opaque plate with the corner cubes facing the opaque plate. This creates a retroreflector with a flat surface like the Telemecanique RF30 in Figure 2.17(b).

While these retroreflectors work well for their intended application, their flat front surfaces produce a great amount of specular reflection. The corner cubes on the backside of the clear plastic could be used as a retroreflector. However, the clear plastic transmits most incident visible light. To create an effective retroreflector in the visible and near-infrared spectrum, a reflective material must be deposited onto

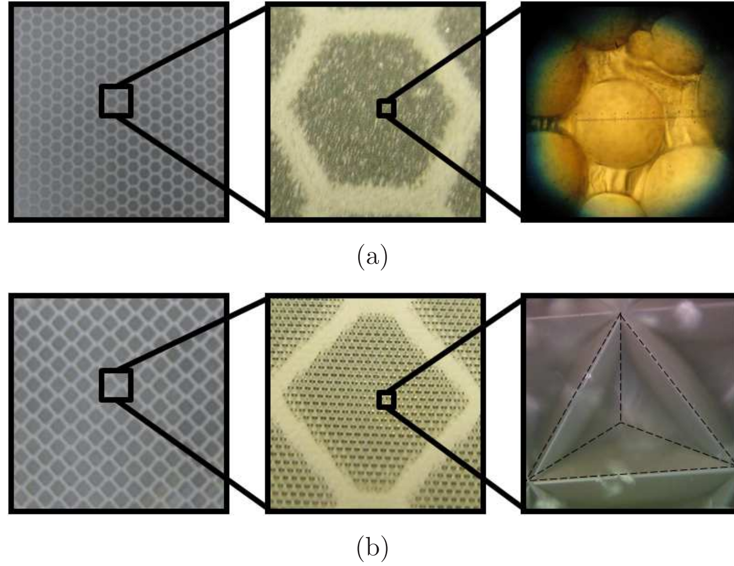
(a)
(b)

Figure 2.16: Retroreflective tape samples at increasing magnifications. (a) Telemecanique RF3870. The diameter of the sphere on the far right is ∼70 μm. (b) 3M 3000X. Each side of the triangular corner element on the far right is ∼210 μm.

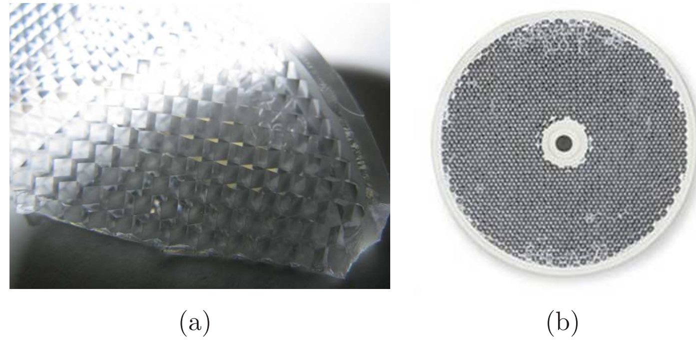
(a) (b)

Figure 2.17: (a) Broken sample of the RF30 retroreflector. The underside of the transparent plastic is shaped as an array of corner cubes. (b)Telemecanique RF30 round retroreflector.

the transparent corner cubes. Gold can be deposited on these plastic reflectors using a sputter coater. Sputter coating (discussed in an earlier section) is a low-temperature deposition process, which would provide an even layer of gold on the plastic corner cubes without melting them.

It may also be possible to sputter coat reflective material on the corner cube arrays used in 3M 3000X retroreflective tape. This tape is fabricated in a similar

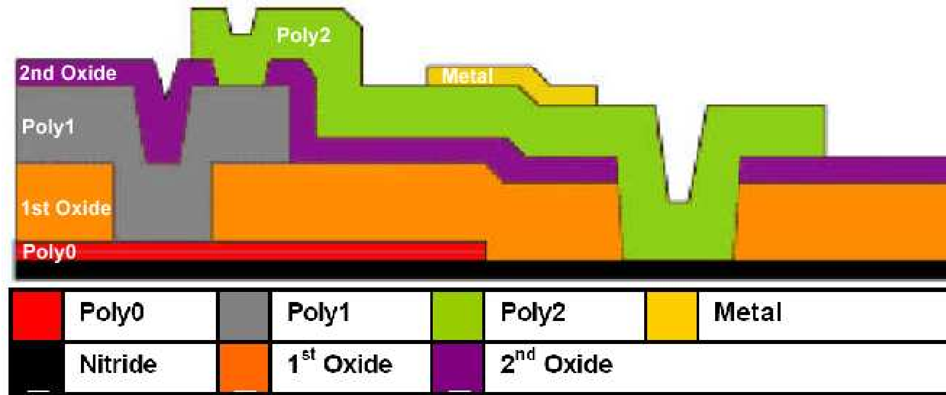

Figure 2.18: Cross sectional layout of the seven PolyMUMPs^{TM} process layers (not to scale). The nitride layer is the foundation for the MEMS structure. The oxide layers are sacrificial layers. The process uses a (100) silicon wafer. [22]

fashion to the RF30 reflector, in that a transparent array of corner cubes is fixed to an opaque backing. By removing the backing, the tiny plastic corner cubes are exposed, and could be coated with reflective material.

2.6.3 PolyMUMPs^{TM} MEMS. The Multi-User MEMS Processes (MUMPs$^{©}$) is a commercial program that provides cost-effective, proof-of-concept MEMS fabrication. This process is designed to be very general in order to support many different designs on a single wafer. PolyMUMPs^{TM} is a three-layer surface micromachining process that uses two sacrificial silicon dioxide layers to provide separation between the polysilicon layers (see Figure 2.18).

The process begins with a (100) n-type doped silicon wafer. A 0.6 μm silicon nitride layer is then deposited on the wafer as an electrical isolation layer using low pressure chemical vapor deposition (LPCVD). Next, a 0.5 μm LPCVD polysilicon film, Poly0, is deposited and patterned using photolithography. After photoresist patterning, the Poly0 layer is etched in an RIE system. A 2.0 μm layer of phosphosilicate glass (PSG), known as 1st Oxide, is deposited by LPCVD. The 1st Oxide is patterned and etched, then the first structural layer of polysilicon, Poly1, is deposited with a thickness of 2.0 μm. After Poly1 is etched, a 0.75 μm PSG layer (2nd Ox-

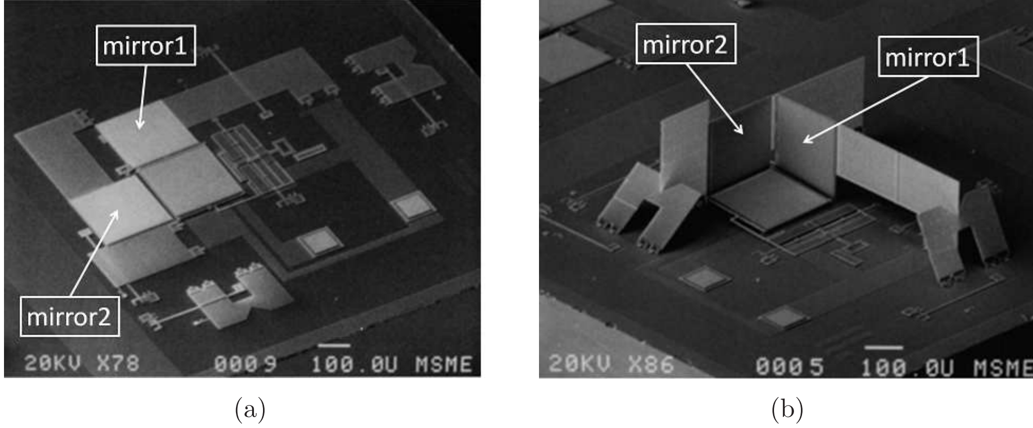

(a) (b)

Figure 2.19: A corner reflector fabricated with the MUMPs© process (a) before assembly and (b) after assembly. Mirror1 and mirror2 rotate on hinges, and are locked in place during assembly to stay orthogonal to the anchored mirror. [18]

ide) is deposited and patterned, followed by a 1.5 μm Poly2 layer. The final layer to be deposited is a 0.5 μm gold layer which provides electrical connections for probing, bonding, or electrical routing. This metal layer can also be used as a reflective layer for optical mirror surfaces. After fabrication, the sacrificial layers (1st and 2nd Oxides) are removed with a release etch. This release etch frees the two polysilicon structural layers (Poly1 and Poly2) [22].

The PolyMUMPs™ process can be used to create corner reflectors. Most MUMPs© corner reflector designs are similar to the design by Hsu et al. in Figure 2.19 [18]. This design consists of three gold coated square mirrors, each 250 μm on a side. The gold coating can be deposited during the MUMPs© process, or sputtered onto the devices after release. The first mirror is created from Poly2 and is anchored to the substrate. Two additional mirrors (mirror1 and mirror2) are also created from Poly2. These mirrors are not attached to the substrate, but instead rotate on hinges attached to one side. By rotating these two mirrors into positions orthogonal to the substrate, a corner reflector is formed. However, MUMPs© flip-up mirrors such as these cannot stay upright without added support. To overcome this, these mirrors are accompanied by flip-lock mechanisms to hold them in place.

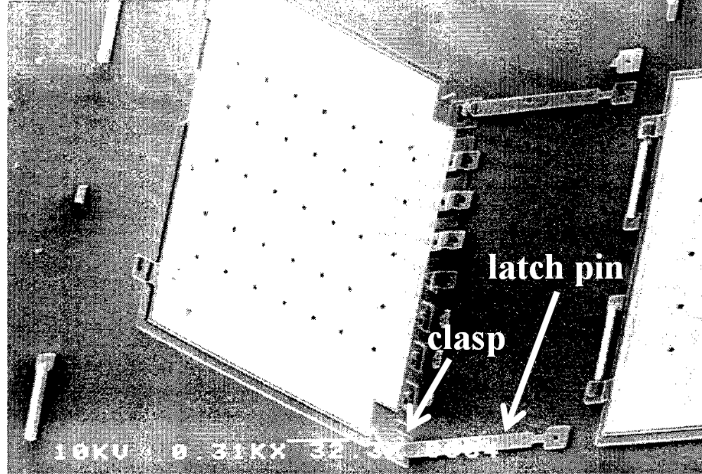

Figure 2.20: MUMPs© hinge lock mechanism. The latch pin is designed to lock into the clasp when the mirror is orthogonal to the substrate. [37]

Although this design is good for building one corner reflector, the flip-lock mechanisms used to hold the rotating mirrors in place occupy a large amount of chip surface area. If the goal is to create an array of corner reflectors, conservation of non-mirror areas is critical. By using elements from a design by Stringer [37], it may be possible to greatly reduce the size of the rotating mirror locking mechanisms. Stringer used MUMPs© latches consisting of a Poly1 clasp and a Poly2 latch pin (see Figure 2.20). The clasp is connected to the side of the mirror and has a T-shaped hole where the latch pin is inserted and locked down. The length of the latch pin is designed to lock into the clasp when the mirror is orthogonal to the substrate. Therefore, the latch pin forms the hypotenuse of a right triangle and the dimensions of the latch pin can be calculated using the Pythagorean theorem.

2.6.4 Silicon on Insulator (SOI) Fabrication. While the PolyMUMPs™ process is useful for the fabrication of MEMS designs, it has two distinct disadvantages with regards to this research project. First, there is no feasible way to automatically assemble an array of corner reflectors. It would not be difficult to incorporate self-assembly mechanisms to rotate the mirrors into the orthogonal position. However, these mechanisms would not only require power but would also occupy a large surface

area, reducing the percentage of devices devoted to corner reflectors. In order to create a more densely packed array of MUMPs© corner reflectors, each individual corner reflector would need to be manually assembled. For large numbers of corner reflectors, this quickly becomes unreasonably time consuming. Second, the PolyMUMPs™ fabrication process currently has a turnaround time of three months. This constraint would only allow for the fabrication of two design layouts during the time permitted for this research. AFIT, along with AFRL, have fabrication facilities that are capable of creating SOI MEMS corner reflectors. Fabricating the devices in-house allows for a quicker turnaround time, which then gives the opportunity for more design revisions.

In 1999, Syms [41] demonstrated a new process for surface tension powered self-assembly of silicon-based MEMS mirrors. These devices were formed from a bonded SOI wafer and rotated out of plane. The device layer provides the silicon for the mirror plates, while the buried oxide layer acts as the sacrificial material. The SOI wafer makes it possible to avoid any complicated multilayer processing.

The mirror plates are rotated into place using surface tension self-assembly. To do this, small pads of meltable material are deposited in such a way to link the edges of a fixed and a movable object which are both originally in the same plane. Before being melted, the pads have a rectangular cross section. When melted, these pads take on a semi-cylindrical cross section. This change in shape results in a torque that can rotate the movable object out of plane. Often, small solder balls are used for this type of self-assembly. However, for this design it was discovered that small pads of thick photoresist (Hoechst AZ4562) were the best solution. When heated, the surface tension of the melting photoresist pads power the out of plane rotation.

Figure 2.21 shows the process sequence used to create the self-assembled structures. The SOI wafers used consisted of a 4 in (100) Si handle layer, a 2 μm thick oxide layer, and a 6 μm thick device layer. To define the moving mechanical parts, a hard mask was created from a 0.7 μm thick layer of Cr metal which was patterned by conventional lithography and wet chemical etching. The mask pattern was transferred

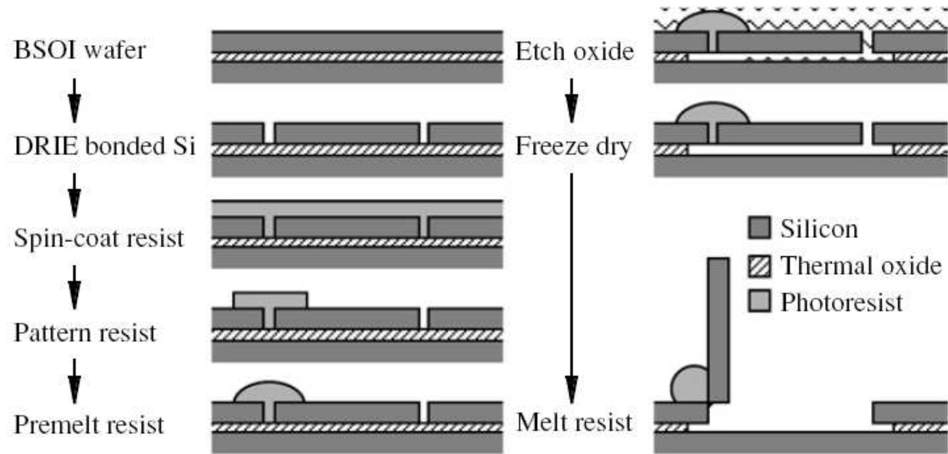

Figure 2.21: Process sequence for self-assembly of SOI microstructures. Out of plane rotation is powered by the surface tension of the heated photoresist. [17]

to the device layer by RIE to a depth of 7 μm, and then the Cr mask is removed with wet etching. DRIE can also be used to improve feature size control, which will be discussed in greater detail later. The etched wafer was then spin-coated with photoresist, patterned, and developed to create the hinge driver pads. The photoresist pads were then premelted to improve adhesion during the release process. Device release was accomplished by wet etching the sacrificial oxide layer in buffered hydrofluoric acid (HF). The wafer was then rinsed and freeze-dried in a mixture of methanol and distilled water. Finally, the devices are assembled by melting the photoresist pads in an oven at 130-150 °C, then sputtered with a thin layer of metal to improve reflectivity.

In a later paper, Syms et al. [39] describe enhancements to the above process in order to improve yield. One improvement was to form the movable parts in the device layer using stop-on-oxide DRIE instead of RIE. While DRIE can achieve a deeper etch, it was important in this design because it allowed for tighter control of feature sizes. Using DRIE improved feature size control from 2 μm to 0.2 μm. This improvement in dimension control increased the accuracy of the fabricated structures. The stop-on-oxide etch also increased uniformity across the device, and prevented any photoresist from sticking to the substrate.

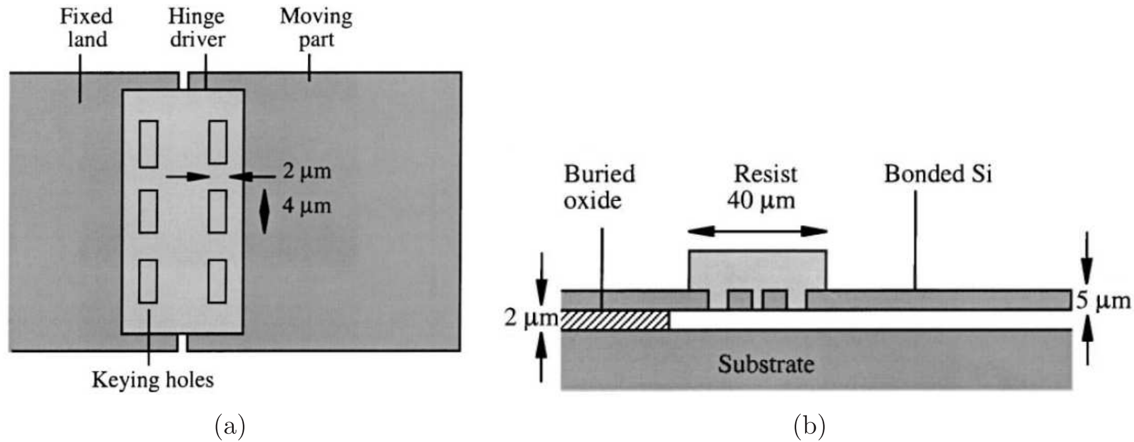

Figure 2.22: (a) Top-down and (b) cross-sectional layout views of the improved SOI hinge structure using keying holes. The holes are filled with the hinge pad photoresist to pin the movable and fixed parts together during release. [39]

It was also found that many of the movable parts separated and were lost during the long buffered HF release. This problem was fixed by etching 2 μm $\times$ 4 μm keying holes into the silicon device layer under the hinge pad locations (see Figure 2.22). During the spin-coating process, these holes were filled by photoresist. When the photoresist hardened, it pinned the movable and fixed parts together during the release etch.

Hong et al. [17] used this SOI design to create corner reflectors. Like the MUMPs© corner reflector, this design uses three orthogonal mirrors. However, in this design all three mirrors rotate. Figure 2.23 shows this device and its mask layout. Two of the mirrors rotate 45° while one long mirror rotates 90°. Each 45° mirror carries an interlocking latch which mechanically stops it from rotating further than 45°. The 90° mirror is mechanically stopped by the two 45° mirrors. The narrow "land" area between the 45° mirrors separates their respective hinge driver pads. These devices were shown to self-assemble very accurately, with mirror angles within 0.18° of their target values. In addition, this design allows for the layout and fabrication of corner reflector arrays which can be self-assembled.

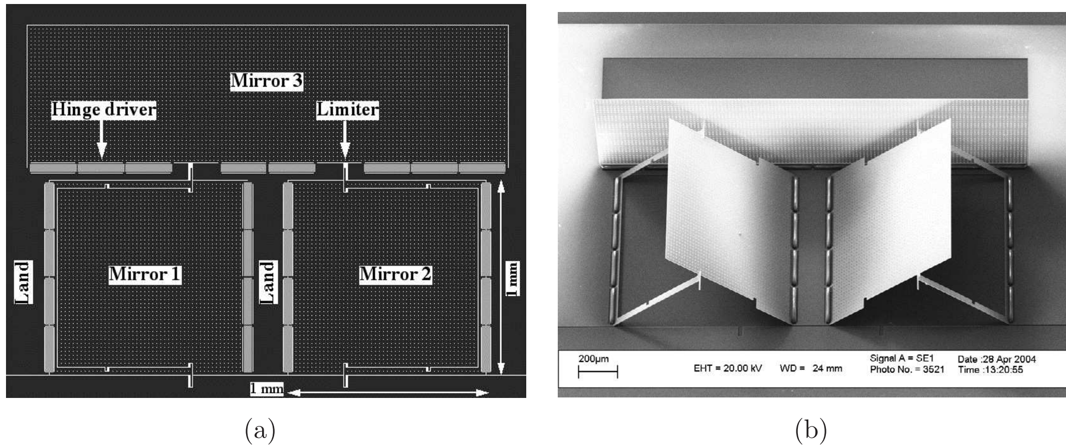

(a) (b)

Figure 2.23: (a) SOI corner reflector mask layout. (b) Fabricated SOI corner reflector after self-assembly. [17]

2.7 Chapter Summary

In this chapter, theories from the fields of optics and microelectronics were reviewed. Typical velocimetry techniques used in the field of shock physics were briefly discussed, which led to a discussion of the PDV system. Next, the OCS and BRDF optical measurements were introduced, as well as the microelectronic fabrication techniques used in this research. Finally, the four retroreflector solutions explored in this research were presented.

III. Theoretical Analysis and Fabrication

This chapter discusses the methodology behind the design and testing of retroreflectors in this research. First, the retroreflective tape designs tested will be introduced, followed by an analysis of metal deposition on retroreflective tapes and commercial reflectors. Next, the MUMPs© and SOI corner reflector designs will be covered in detail, including an in-depth analysis of dimensions and materials used. Then, testing processes and expected results will be reviewed.

3.1 Retroreflective Tape Designs

The retroreflective tape samples used in this research all consist of thousands of tiny elements, which are either spheres or triangular-faced trihedral corner reflectors. The geometries of these elements are illustrated in Figure 3.1. The spherical elements have a diameter, a. The corner reflectors are typically isosceles triangles with side lengths, a and b.

3.1.1 Spherical Element Retroreflective Tape Samples. Three of the five retroreflective tape samples used in this research were comprised of spherical elements. These tapes were all made by Telemecanique, with model numbers RF7590, RF7610, and RF3870, shown in Figure 3.2(a), (b), and (c), respectively.

RF7590 and RF7610 appear very similar, but there are distinct differences between the two. RF7610 consists of closely packed spheres of varying sizes. Smaller

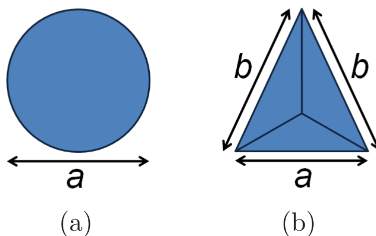

Figure 3.1: Illustration of reflective tape element geometries. (a) A spherical element of diameter a. (b) A triangular-faced trihedral corner element with side lengths a and b.

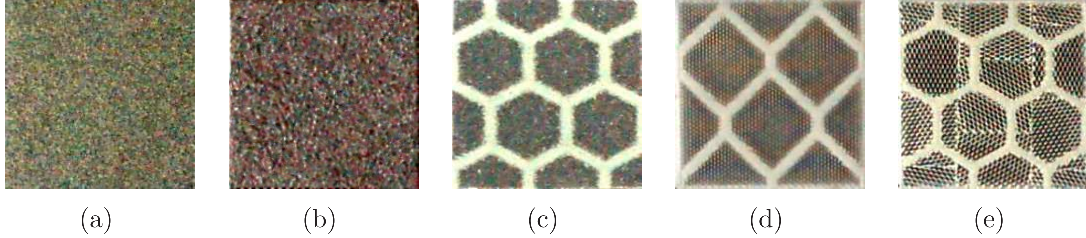

(a) (b) (c) (d) (e)

Figure 3.2: Reflective tape samples used. Sample sizes are all 10 mm × 10 mm. (a) Telemecanique RF7590. (b) Telemecanique RF7610. (c) Telemecanique RF3870. (d) 3M 3000X. (e) Telemecanique XUZB11.

spheres fill in the areas not covered by the larger spheres. On the other hand, all of the spherical elements in RF7590 are roughly the same size. Because of this, the spheres cannot be packed as densely as those in RF7610. RF3870 has a similar sphere size and packing density as RF7610, but the elements are clustered in a hexagonal honeycomb pattern. Both RF7590 and RF3870 have a polymer coating to protect them from damage. While this coating may be useful in some applications, it appears to create significant specular reflections. These reflections could lead to crosstalk in the triaxial PDV setup. RF7610 has no protective coating.

3.1.2 Corner Element Retroreflective Tape Samples. For a triangular-faced trihedral corner reflector, each of the three mutually orthogonal sides is an isosceles triangle. Two of the retroreflective tape samples tested consist of triangular-faced trihedral corner reflector elements. These samples are 3M 3000X and Telemecanique XUZB11, seen in Figure 3.2(d) and (e), respectively. The 3M sample is made of smaller corner elements, clustered in a diamond pattern. XUZB11 has slightly larger corner elements than the 3M tape, clustered in a honeycomb pattern similar to RF3870. Both of the corner element samples have a protective polymer coating.

A summary of the characteristics for all five retroreflective tape samples can be seen in Table 3.1.

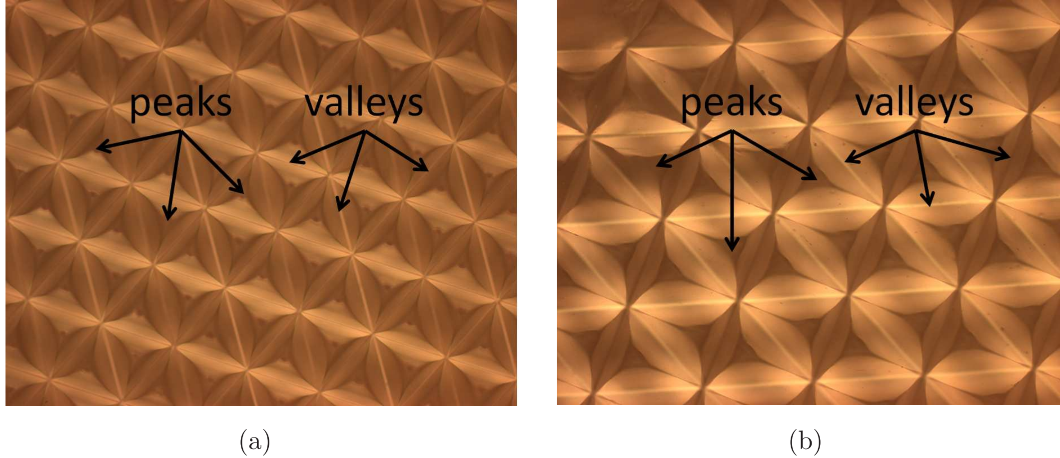

(a) (b)

Figure 3.3: Backside view of reflective tapes at 10x magnification. No two sides that form a valley are orthogonal. (a) 3M 3000X. (b) Telemecanique XUZB11.

3.2 Metal Deposition on Retroreflective Tape and Reflectors

It was quickly discovered that metal deposition on the back sides of the corner cube retroreflective tapes would not create effective retroreflectors. While the triangular faces create orthogonal angles on the front sides of the tapes, they do not correspond to orthogonal angles on the back sides. This is visible in Figure 3.3. No two sides that form a valley on the back sides of the tapes are orthogonal. Because of this, metal deposition on the back sides of these tapes was never done.

Gold sputtering was accomplished on the backside of the Telemecanique RF30. This reflector was first detached from its back plate to expose the corner cube array. It was cleaned with methanol and isopropyl alcohol to remove any dust and impurities

Table 3.1: Retroreflective tape sample characteristics

Design	Manufacturer	Model Number	Reflecting Element	Element a (μm)	Sizes b (μm)	Protective Coating
1	Telemecanique	RF7590	sphere	∼60	-	yes
2	Telemecanique	RF7610	sphere	30-70	-	no
3	Telemecanique	RF3870	sphere	30-70	-	yes
4	3M	3000X	corner	200	210	yes
5	Telemecanique	XUZB11	corner	260	300	yes

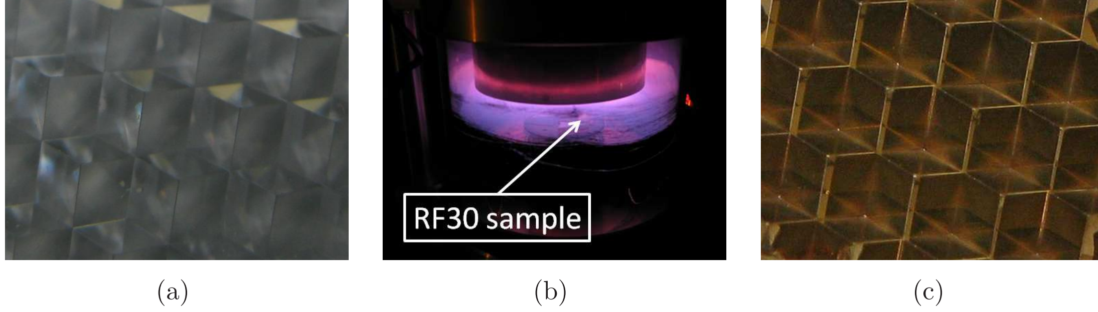

(a) (b) (c)

Figure 3.4: Sputtering gold onto RF30 reflector. (a) Backside of RF30 corner cube array before sputtering. (b) RF30 sample in the Ladd 30800 sputterer. (c) Backside of RF30 corner cube array after sputtering.

that would inhibit adhesion of the sputter coated gold. The reflector was then placed in a Ladd 30800 sputterer, which deposited an even gold layer approximately 100 nm thick. The RF30 sample used can be seen before, during, and after the sputtering process in Figure 3.4.

3.3 MUMPs© Corner Reflector Design

The MUMPs© corner reflectors in this design consist of one fixed mirror and two rotating mirror plates. The rotating mirrors flip up until orthogonal to the fixed mirror, and are then locked in place. The fixed mirror is created from a single anchored layer of Poly2. The rotating mirror plates are built from stacked Poly1 and Poly2 layers to increase mirror flatness and strength. L-Edit layout editor was used to design the MUMPs© corner reflectors. Figure 3.5 shows two completed MUMPs© corner reflector layouts. For these devices, the effective dimensions of the rotating mirrors are 170 μm × 170 μm.

During the MUMPs© fabrication, residual stresses build up between layers. When the devices are released, these layers tend to contract or expand into unstressed states. Stacked layers contract or deform at different rates, which causes bending in MUMPs© structures. The worst bending occurs between the Poly2 and Metal layers. This stress induced curvature leads to seriously degraded optical performance [17]. In order to increase mirror flatness, the Metal layer is not used in some of the

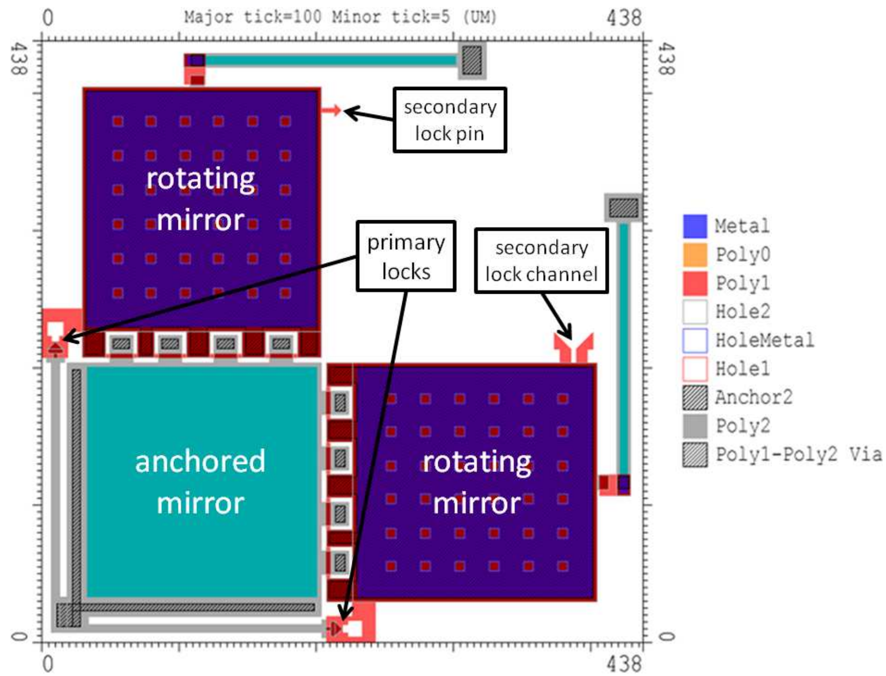

(a)

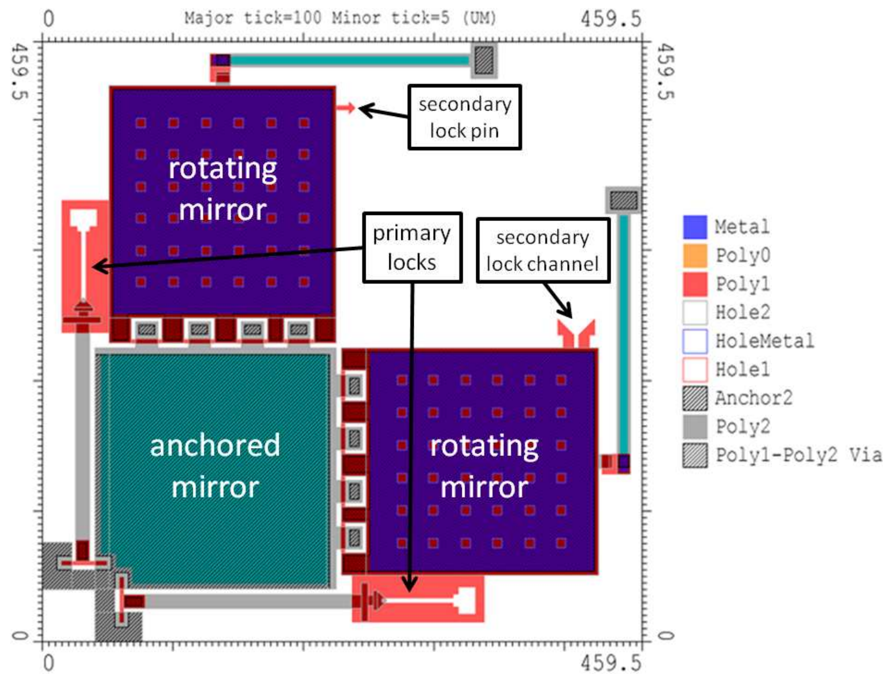

(b)

Figure 3.5: PolyMUMPs^{TM} corner reflector layouts. Each design is comprised of one fixed mirror and two movable mirrors. The movable mirrors are rotated until orthogonal with the fixed mirror, then locked in place. The two corner reflector layouts shown here have different primary locking mechanism designs.

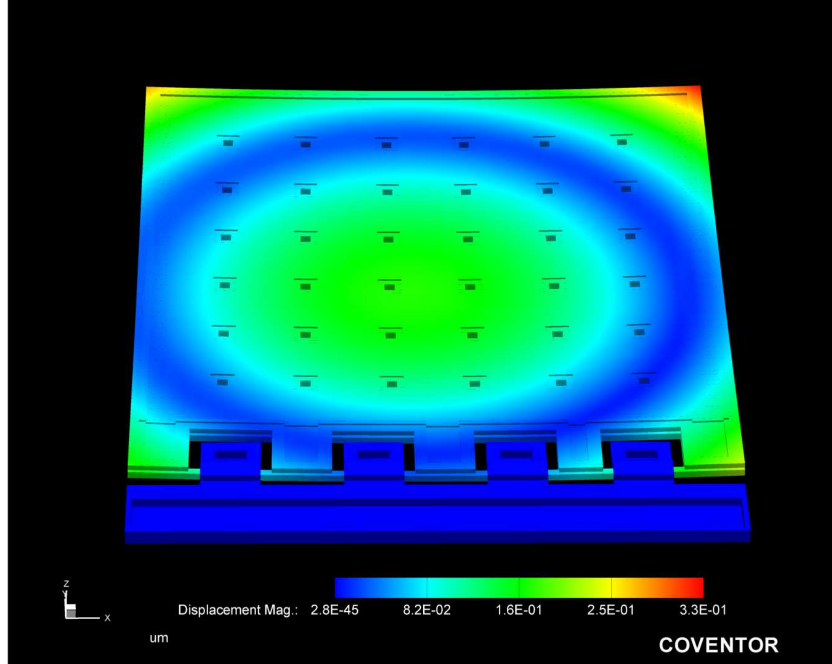

Figure 3.6: Coventorware model of a hinged mirror with the PolyMUMPs™ Metal layer. Residual stress built up between the gold and polysilicon layers causes bending of the mirror.

designs. For the MUMPs© devices without the Metal layer, gold will be deposited by a low temperature sputter coating process after release. The mirror with the PolyMUMPs™ Metal layer was modeled using Coventorware to illustrate the extent of mirror curvature. Figure 3.6 shows this model. For more information on the effects of MUMPs© mirror curvature on optical performance, see Hsu et al. [18].

The MUMPs© corner reflectors rely on three components to move the mirror plates into position. First, the hinges allow the mirror plates to rotate out of the substrate plane. Second, the help-flip cantilevers deflect upward to keep the mirror plates above the substrate. This eases assembly by allowing a microprobe to be slid under the mirror. Finally, the hinge locks prevent the mirrors from rotating past 90°. These three components will be discussed in further detail in the following subsections.

3.3.1 MUMPs© Hinge Design. MUMPs© hinges are constructed using the Poly1 and Poly2 layers. Due to the conformal nature of the MUMPs© process,

Poly2 will fill in areas where there is no Poly1. Figure 3.7 shows a cross section of a MUMPs© hinge design. A Poly1 hinge pin is partially encapsulated by Poly2. When the 1st Oxide is removed, the Poly1 hinge pin is free to rotate inside the Poly2 staple. In the figure, y is the combined thickness of 1st Oxide, Poly1, and 2nd Oxide, which is 4.75 μm for PolyMUMPs™. The Poly1 hinge pin thickness, h, is 2.0 μm. The hinge pin width, x, must be large enough to support whatever structure is attached to it. However, there is a limit to how wide the Poly1 pin can be, as seen in Figure 3.7(b). The Poly1 pin must clear the Poly2 staple at the maximum Poly1 hinge height. This limit, x_{max}, is found by making sure the hypotenuse of the triangle formed by x_{max} and h is less than y:

$$\sqrt{x_{max}^2 + h^2} < y \tag{3.1}$$

By plugging in the thicknesses for the PolyMUMPs™ layers, the maximum Poly1 hinge pin width is then

$$x_{max} < \sqrt{(4.75\mu\text{m})^2 - (2.0\mu\text{m})^2} = 4.308\mu\text{m} \tag{3.2}$$

In order for the Poly1 pin to clear the Poly2 staple, x_{max} must be less than 4.3 μm. Because of PolyMUMPs™ fabrication tolerances and common misalignment errors, the hinge pin width should probably be less than 3.5 μm to ensure proper function. To compensate for any PolyMUMPs™ design tolerances, a pin width of 2.5 μm was used in this design. This pin width was found to provide adequate support for the attached rotating mirror structures.

The MUMPs© corner reflector hinge design layout is shown in Figure 3.8(a). The Poly1 hinge pin is attached to the Poly1-Poly2 stacked mirror plate. The Poly2 staple comes off the fixed mirror, conforms around the Poly1 pin, and is then anchored to the nitride layer. The size of this Poly2 anchor is another critical design element. The anchor must be large enough to keep the Poly2 staple in place during rotation of the Poly1 hinge pin. For this research, the Poly2 hinge anchor is 12 μm $\times$ 7 μm.

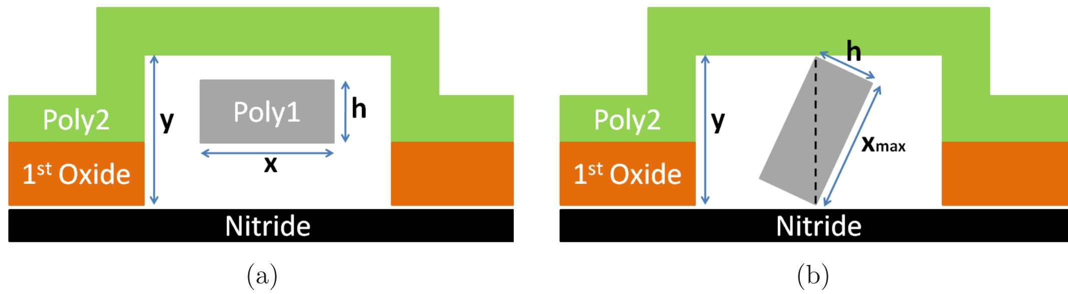

Figure 3.7: Cross section of MUMPs© hinge. For PolyMUMPs™, the thickness, y, is 4.75 μm. The hinge pin height, h, is 2.0 μm. (a) The hinge is partially encapsulated by Poly2 due to the conformal nature of the MUMPs© process. (b) The limiting constraint of the hinge pin width, x_{max}.

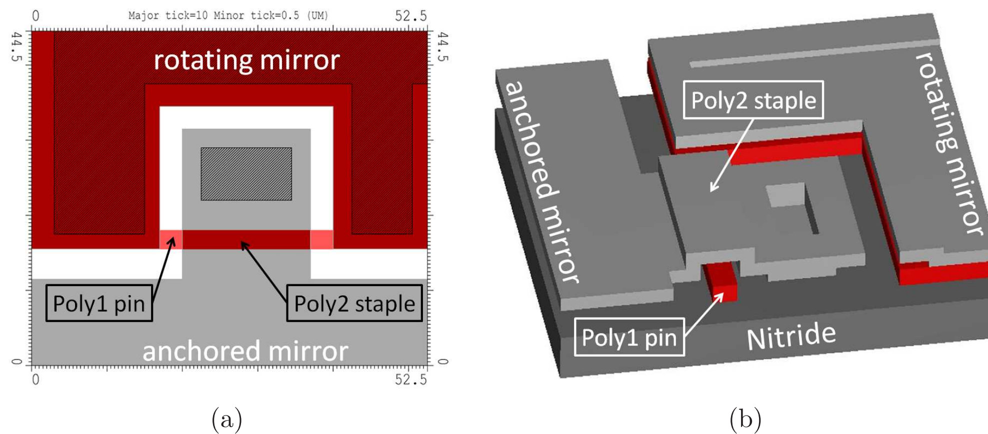

Figure 3.8: MUMPs© corner reflector hinge design. (a) L-Edit hinge layout (b) L-Edit 3-D model of hinge. This model shows that the Poly2 staple allows the Poly1 pin enough room to rotate.

Figure 3.8(b) shows a 3-D model of this hinge design. This model shows that the Poly2 staple leaves enough room for the Poly1 hinge pin to rotate fully.

3.3.2 MUMPs© Residual Stress Help-Flip Cantilevers. The MUMPs© residual stress help-flip cantilevers are designed to keep the rotating mirrors above the substrate. These cantilevers are placed at the top of each rotating mirror plate as seen in Figure 3.9. They are constructed of stacked Poly2 and Metal layers, which causes them to bend upward out of the substrate plane. This bending is due to the residual stresses built up between the Poly2 and Metal layers (the same effect was

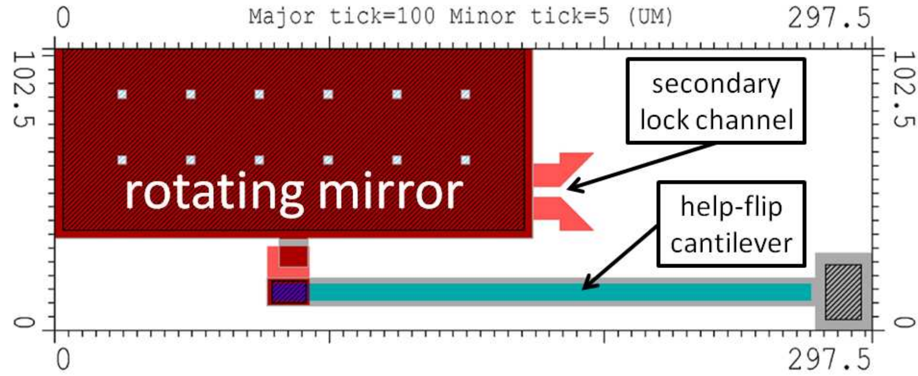

Figure 3.9: PolyMUMPs™ mirror help-flip cantilever. The Poly2-Metal stack cantilever bends upward out of the substrate plane to lift the mirror plate.

seen in the mirror warp of Figure 3.6). A tab of Poly1 is attached to the end of each cantilever. A Poly2 tab sticks out the top of each mirror plate. The Poly1 tabs of the help-flip cantilevers are under the Poly2 tabs of the mirrors, allowing the cantilevers to lift the mirror plates. These cantilever will not move the rotating mirrors into their final positions, but instead create a gap between the plate and substrate. A probe is then used to lift the rotating mirrors until they are orthogonal to the fixed mirror.

3.3.3 MUMPs© Hinge Lock Mechanism. The two primary hinge lock mechanisms used in this design are both similar to the one developed by Stringer [37]. This MUMPs© hinge lock consists of a Poly1 clasp and a Poly2 pin. The clasp is connected to the side of the mirror and has a T-shaped hole where the pin is inserted and locked down. The tip of the corresponding pin is I-shaped, with the width of the I-beam just smaller than the width of the T-shaped hole in the clasp. When the mirror is flipped up the I-shaped tip of the pin is inserted into the T-shaped hole in the clasp. When the mirror is orthogonal to the substrate, the I-pin slides down into the T-clasp, locking the mirror in place. The dimensions of the latch are calculated using the Pythagorean theorem. The length of the latch pin is designed to lock into the clasp when the mirror is orthogonal to the substrate. Therefore, the latch pin forms the hypotenuse of a right triangle.

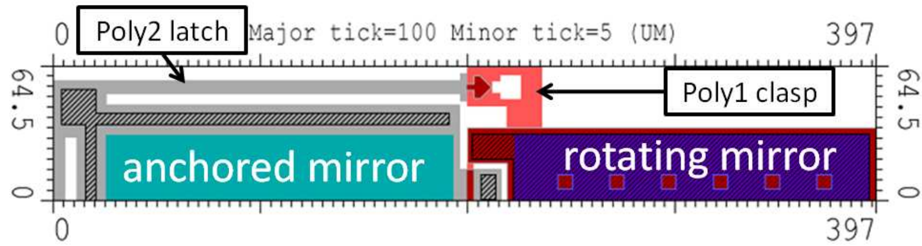

(a)

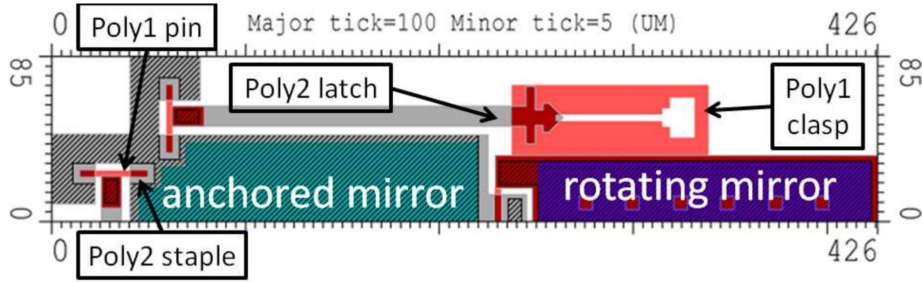

(b)

Figure 3.10: MUMPs© mirror hinge lock mechanism designs. (a) Cantilevered hinge lock. (b) Hinged hinge lock. In each design, when the mirror is flipped up the I-shaped tip of the Poly2 latch pin is inserted into the T-shaped hole in the Poly1 clasp.

The primary hinge lock designs used in this research are similar to the one just described, with a few modifications. The first design, seen in Figure 3.10(a), has a cantilevered latch mechanism . This design is the same as Stringer's, except the tip of the latch pin has been given a pointed end. This arrow design allows the latch to guide itself into the clasp, even if the two are slightly misaligned.

The second design is a hinged latch mechanism, seen in Figure 3.10(b). This design varies from Stringer's hinge lock in a few ways. First, the clasp is placed higher on the rotating mirror. This increases the torque applied to the clasp by the latch pin, increasing the overall stability of the mirror lock. However, this increases the angle between the latch pin and the substrate. If the fixed end of the latch pin remained anchored as in Stringer's design, the latch pin would most likely snap due to the large amount of bending it would experience. Because of this, the fixed end of the latch pin has been changed to a hinge. Like the cantilevered design, the tip of the latch

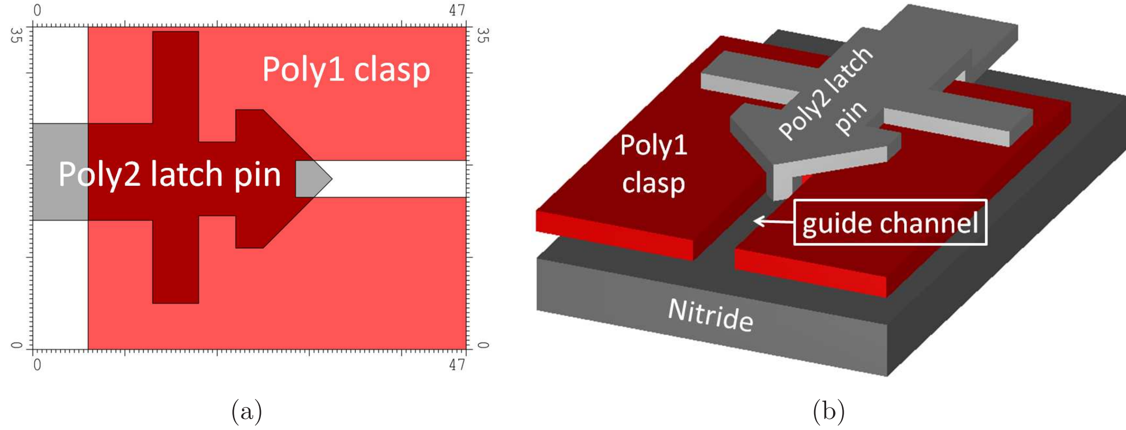

(a) (b)

Figure 3.11: (a) Close-up of the MUMPs© hinged locking mechanism. The tip of the Poly2 latch pin overlays a channel in the Poly1 clasp. (b) The 3-D model shows how the conformal nature of PolyMUMPs™ creates a guide for the latch pin.

pin has also been given a pointed end. By adding a long, thin channel to the clasp, the conformal nature of the PolyMUMPs™ process can be used to create a guide for the latch pin. The tip of the pointed latch pin is placed over the channel, as seen in Figure 3.11(a). This allows some of the Poly2 latch layer to be deposited inside the channel, as seen in the 3-D model of Figure 3.11(b). This design keeps the tip of the latch pin aligned with the clasp, as the channel guides the latch pin tip to the clasp hole.

A secondary locking mechanism is included on all designs. This lock consists of a pin attached to one of the rotating mirrors which is inserted into a channel on the other rotating mirror. These can be seen in the corner reflector layouts of Figure 3.5. The pin and channel mechanisms are each on opposite sides of the primary locks of their respective rotating mirrors.

3.4 MUMPs© Corner Reflector Fabrication

The MUMPs© corner reflectors were fabricated during the PolyMUMPs™ 84 run. Upon release, it was evident that the help-flip cantilevers had worked as designed. From visual inspection, it was clear that many of the mirrors had rotated out of the

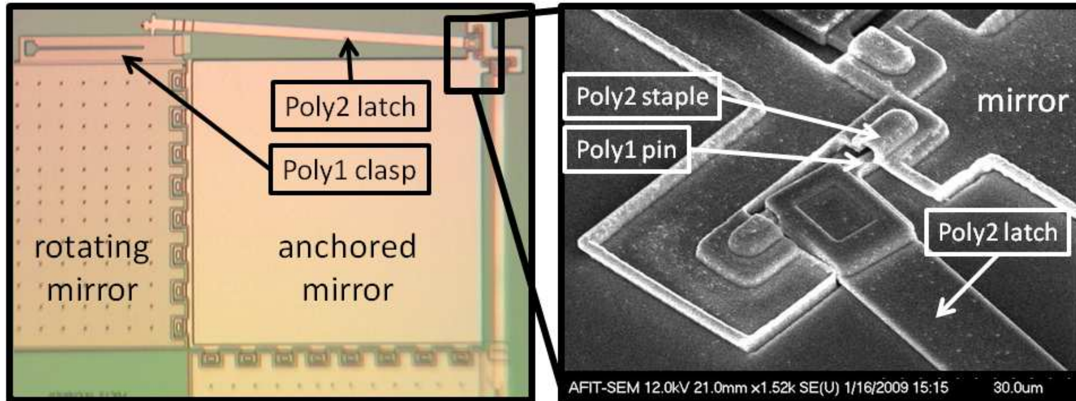

Figure 3.12: Unhinged MUMPs© corner reflector locking mechanism. A close up view of the unhinged portion of the locking mechanism reveals that the Poly1 pin is too narrow for the Poly2 staple, allowing the Poly2 latch to rotate laterally.

substrate plane. Almost all of the design elements survived the fabrication and release process, except for the hinged primary locking mechanisms.

Figure 3.12 shows a typical released device with the hinged primary locking mechanism design. The latch pin at the top of the figure has been knocked out of place, making it impossible to lock the mirror in place once assembled. Looking closer at the latch pin hinge in Figure 3.12, it is evident that the Poly1 hinge pin of the latch pin is too narrow for the Poly2 staple, allowing the latch to rotate sideways. This rotation moves the pointed end of the latch pin out of line with the clasp attached to the rotating mirror. This could be prevented by adding some Poly2 guides along the length of the latch pin to keep it from rotating sideways.

Another failure of the hinged locking mechanism is in the latch pin guide channel. From Figure 3.13, it appears that the pointed end of the latch pin is in the guide channel as designed. However, further magnification reveals that the guide channel is not wide enough to accommodate the tip of the latch pin. Because of this failure, it is possible for the latch pin to rotate sideways and out of line with the clasp.

While the hinged primary locking mechanism was not a success, the cantilevered primary lock design worked very well. Figure 3.14 shows an assembled corner reflector

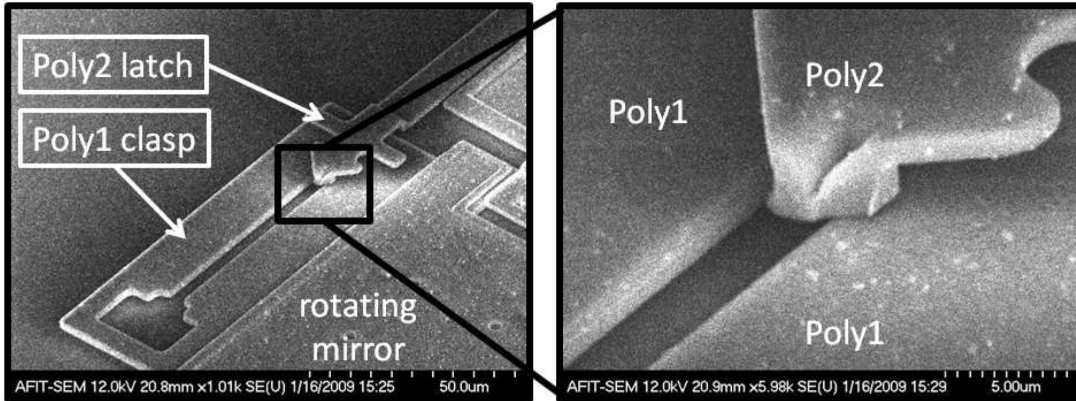

Figure 3.13: Failure of the hinged style locking mechanism. The pointed end of the latch pin appears to be in the groove as designed. However, the close up view shows that the tip of the locking mechanism is too large to fit in the groove.

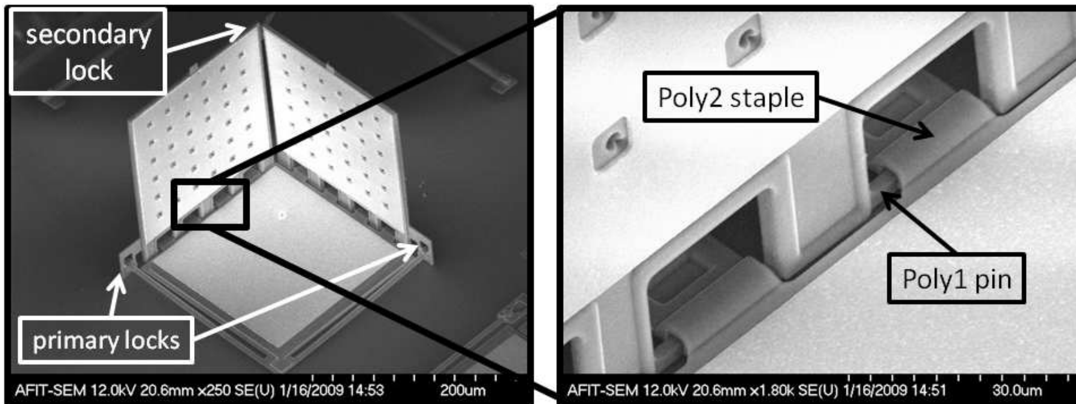

Figure 3.14: An assembled MUMPs© corner reflector. A close up view reveals that the hinges have worked as designed.

using the cantilevered locking mechanism. From this figure, it is clear that the hinges worked as modeled in Figure 3.8. This corner cube was assembled by first using a microprobe to rotate one of the mirrors until its cantilever lock engaged. Next, the second mirror was rotated with the probe until its cantilever lock engaged, as well as the secondary pin and channel lock. The engaging of the primary cantilevered locking mechanism, as well as the secondary pin and channel lock, are seen in Figure 3.15.

While it was shown that a corner reflector could be assembled using a microprobe, the time required for this assembly was long. Many other reflectors were

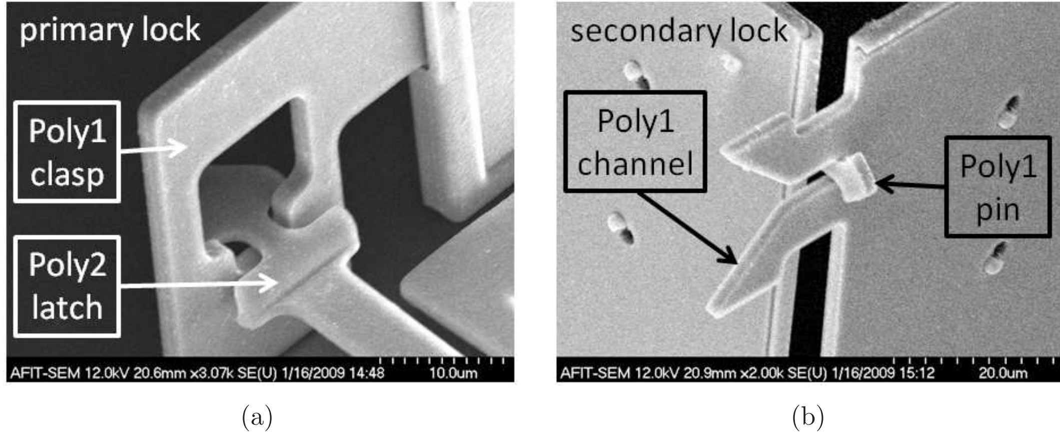

(a) (b)

Figure 3.15: Assembled MUMPs© corner reflector locking mechanisms. (a) Engaging of the cantilever style primary locking mechanism. (b) Engaging of the secondary locking mechanism at the top of each of the rotating mirrors.

damaged or broken during probe assembly attempts. Because of the time required and significantly low yield, it would be impractical to create an array of MUMPs© corner reflectors in this manner.

3.5 SOI Corner Reflector Design

The goal of this design is to create a triangular-faced trihedral corner reflector using an SOI wafer. This corner reflector features three rotating mirrors which lock into place orthogonally to each other. The mirror elements are created from the device layer of the SOI wafer, and are rotated by photoresist hinges. This section will discuss the design process for these devices.

3.5.1 Triangular Corner Reflector Layout. Triangular corner reflectors are typically used in radar systems more often than square sided corner reflectors because they are easier to build and have better angular response in the azimuthal plane [24]. An example of a triangular corner reflector can be seen in Figure 3.16. This particular reflector is part of the NASA Rosamond Calibration Array, which is used for calibration of the NASA AIRSAR and SIR-C missions. For the SOI design, the goal is to create a triangular corner reflector so that the apex of the reflector is normal

Figure 3.16: An example triangular corner reflector from the NASA Rosamond Calibration Array. [29]

to the substrate plane. In this orientation, light incident normal to the substrate plane would also be normal to the reflector. The resulting structure has three-fold rotational symmetry with respect to the surface normal. This symmetry is important because it allows the three rotating mirror plates to be identical in size as well as required rotation angle. This becomes important during the self-assembly process where the mirror plates must be nearly identical to ensure they properly lock each other into place.

In order to rotate the three mirror plates, there must be a flat, anchored surface at the center of the reflector. Without this surface, it would not be possible to create the photoresist hinges which will rotate the mirror plates into position. Unfortunately, this flat plate turns the center of the triangular corner reflector into a flat mirror, reducing the overall retroreflectivity of the device. Because of this, it is important to keep this center anchor as small as possible. The anchor must be large enough to support a photoresist hinge strong enough to lift the rotating plates, but small enough to maximize overall device retroreflectivity.

Figure 3.17 steps through the layout design process for the triangular corner reflector. The steps of this process are as follows:

1. An equilateral triangular with sides of length, b, is created as the center anchor.

2. Next, one rotating mirror plate is created by forming an isosceles right triangle whose apex is inside the anchor triangle and $b/2$ from the midpoint of one of the anchor triangle sides.
3. The portion of this right triangle inside the anchor triangle is then removed, as well as an additional 2.5 μm to create a trench for the photoresist hinge.
4. The top two corners of this resulting trapezoid are then removed to prevent them from interfering with the rotation of the other two rotating mirror plates.
5. The hinge driver mechanism for the mirror rotation is a strip of photoresist of width $(2w + 2.5\mu\text{m})$, and thickness h. The length of the photoresist strip is arbitrary, but should be as long as possible to ensure proper rotation of the mirror plate.
6. Steps 2 through 5 are then repeated to create the two additional rotating mirrors that complete the triangular corner reflector.

3.5.2 Enhancements to Improve Basic Design. Several enhancements have been made to the basic triangular corner reflector design discussed previously and can be seen in Figure 3.18. The first of these modifications is the addition of etch holes to the mirror plates. This is a basic design feature in micromachined mirrors. These etch holes will speed the release process of the mirrors by granting the releasing etchant more access to the oxide underneath. Unfortunately, these etch holes also decrease the effective area of the mirror plates, thus reducing their reflectivity. Additionally, these holes introduce diffraction losses to the system which also reduce reflectivity. Both of these losses will be discussed in a later section.

In a design by Syms et al. [39], it was found that mirror plates similar to the ones in this design separated and were lost during the release process. This problem was fixed by etching 2 μm $\times$ 4 μm keying holes into the silicon device layer under the hinge pad locations. During the spin-coating process, these holes were filled with photoresist. When the photoresist hardened, it pinned the movable and fixed parts

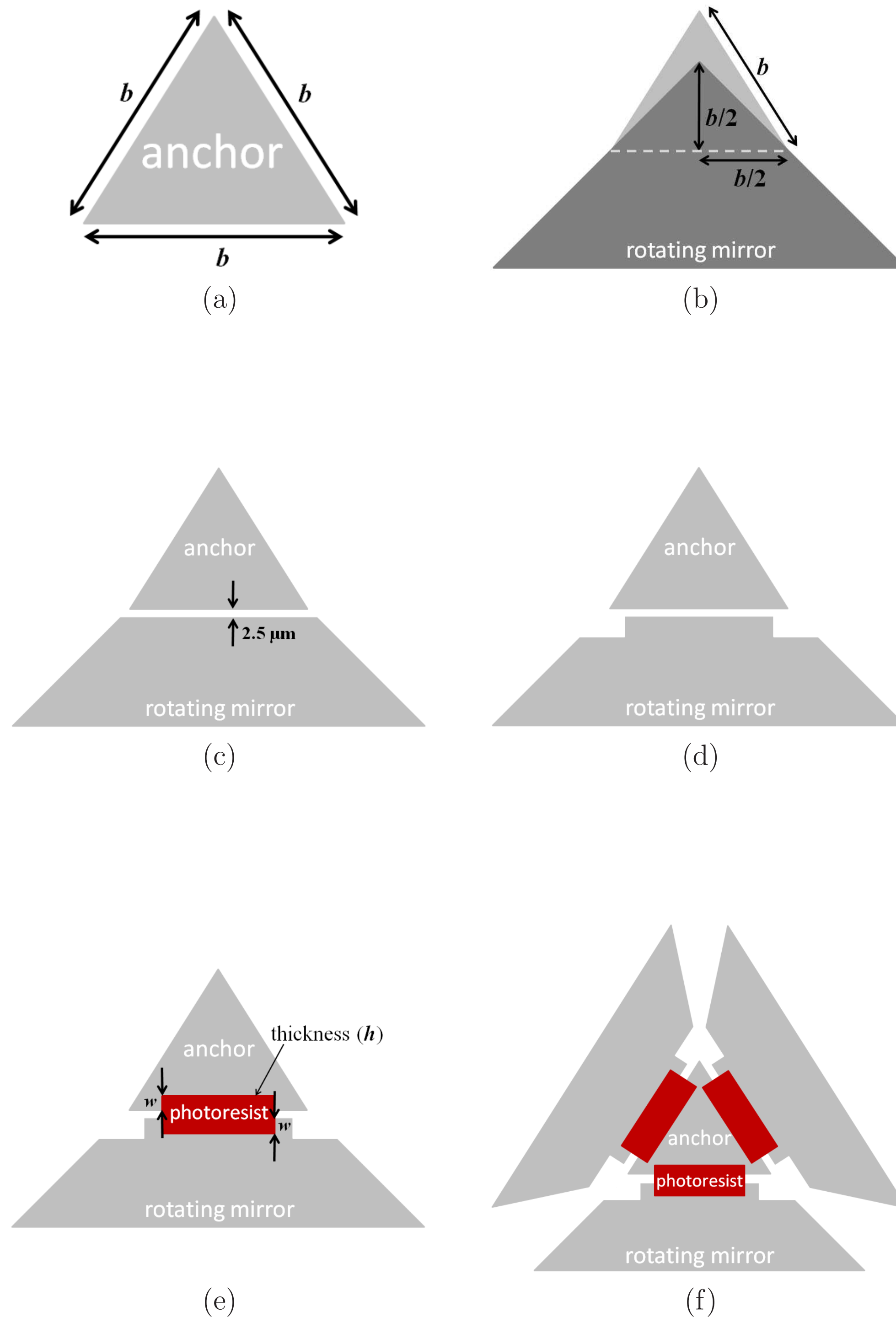

Figure 3.17: Triangular corner reflector layout design process. (a) An equilateral triangle acts as an anchor for the rotating mirrors. (b-d) Each rotating mirror is formed from an isosceles right triangle, which is then reduced to a trapezoid. (e) A photoresist pad links the anchor to the rotating mirror. (f) Steps (b-e) are repeated for the remaining two rotating mirrors.

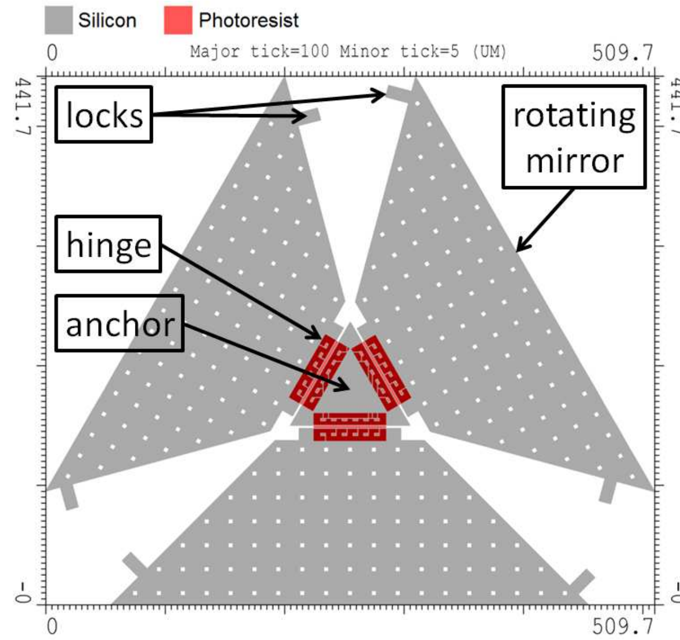

(a)

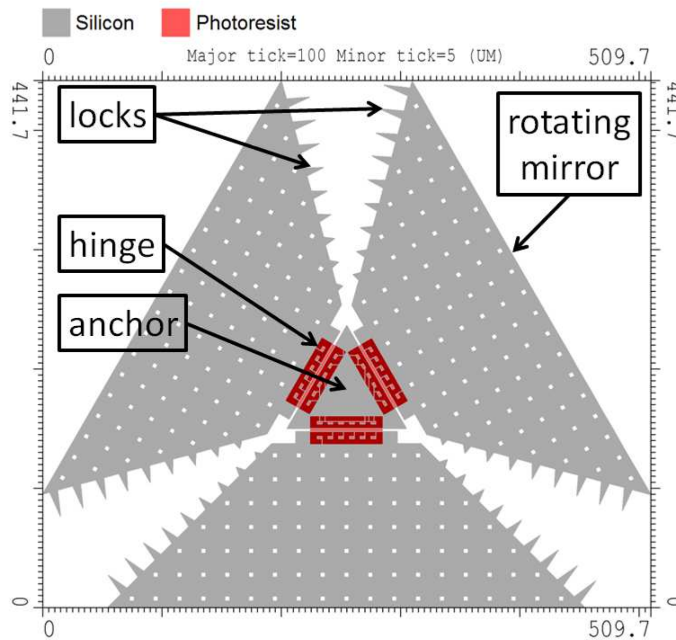

(b)

Figure 3.18: SOI triangular corner reflector designs. (a) The single-tab hinge-lock mechanism is designed to keep the mirror plates from moving past their desired rotation angle. (b) The multiple-tab hinge-lock mechanism works in the same way, but with multiple interlocking teeth.

together during the release wet etching. These same holes have been included in the triangular corner reflector design under the photoresist hinge pads.

Finally, it was necessary to add some sort of rotation limiting mechanism to prevent the mirror plates from rotating past their desired positions. The first of these simple hinge-lock mechanisms can be seen in Figure 3.18(a). In this design, tabs are added to the ends of each rotating mirror. As each mirror rotates out of the substrate plane, its edges become closer to the adjacent mirror plate edges. At the desired rotation angle for the mirror plates, adjacent edges will be perpendicular to each other. When this is true, these locking tabs will prevent each mirror plate from rotating further. The rotational force in the photoresist will keep the plates from rotating back toward the substrate, while these locking tabs will keep them from rotating too far. The hinge-lock mechanism in Figure 3.18(b) uses this same methodology, but with multiple tabs shaped as teeth. At the desired rotation angle, these teeth will interlock to prevent further rotation of the mirror plates.

3.5.3 Surface Tension Self-Assembly Model. In this research, the surface tension self-assembly is modeled as a 2-D system. Figure 3.19 shows the geometry used in this model. A rotating mirror is represented by a movable flap of thickness d. This flap is connected to an anchor by a meltable pad of width $2w$ and height h. For this design, the meltable pad is created by depositing and patterning photoresist.

Once deposited, the photoresist is melted as shown in Figure 3.19(b). The surface perimeter of this melted photoresist is s. As the photoresist is heated further, it moves toward a lower surface energy shape and the pad begins to form a sphere. This causes a reduction in the perimeter length, which results in rotation of the hinge as shown in Figure 3.19(c). Here, F_γ is the force due to surface tension and F_p is the force due to the Laplace pressure [43]. For rotation to occur, the resultant torque from these two forces must be larger than the torque needed to rotate the flap. The system will stabilize at a rotation angle of θ_e when there is a balance among these torques. At this point, the pad may be solidified by cooling as in Figure 3.19(d).

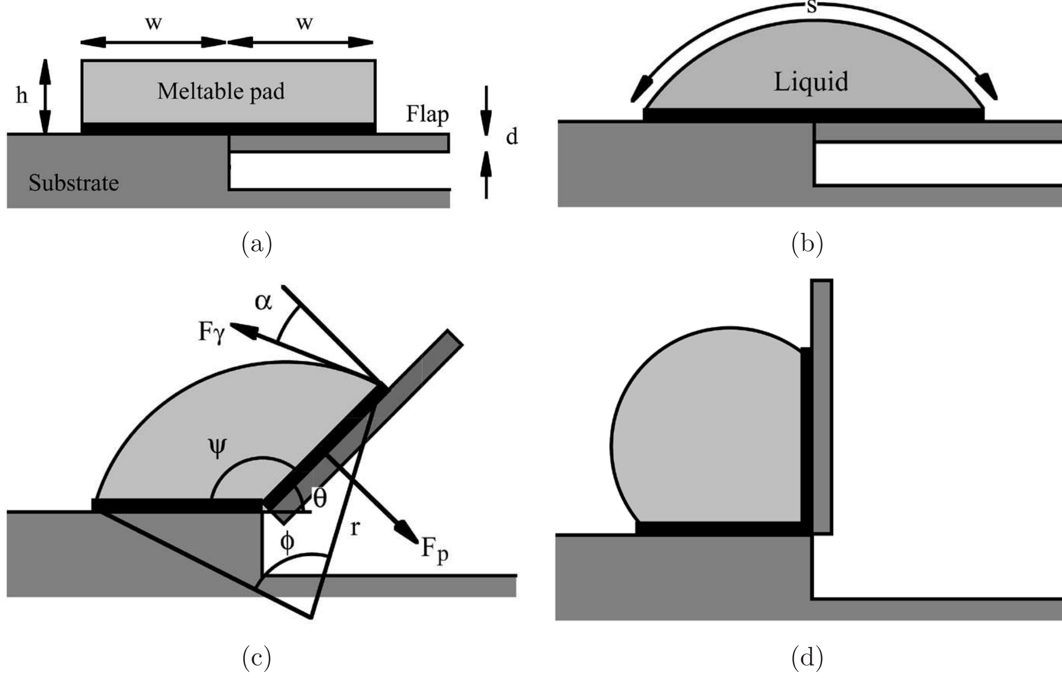

Figure 3.19: Two-dimensional geometry for surface tension powered self-assembly. For this research the meltable pad in (a) is photoresist and the substrate is the device layer of an SOI wafer. [43]

Torque on the hinge is caused by two forces. Surface tension attracts the surface portion of the photoresist to the top surface of the mirror. If γ is the surface tension coefficient of the meltable pad material, the torque per unit length due to the surface tension force, T_γ, is then

$$T_\gamma = \gamma\ w\ \cos(\alpha) \tag{3.3}$$

where α is the angle between F_γ and the surface normal of the rotating mirror. The Laplace pressure, P, is defined as the pressure difference between the inside and outside of a bubble. An excess pressure exists inside the photoresist bubble due to its curved boundary [42]. The torque per unit length due to the Laplace pressure, T_p, is

$$T_p = \frac{P\ w^2}{2} \tag{3.4}$$

The resultant torque is then $T_\gamma - T_p$. It can also be shown that $\alpha = (\pi - \theta - \phi)/2$ and $r = w\cos(\theta/2)/\sin(\phi/2)$, with θ and ϕ defined in Figure 3.19(c). Substituting

these equations into Equation 3.3 and Equation 3.4 gives the resultant torque per unit length as

$$T = \gamma\ w \left[\sin\left(\frac{\theta + \phi}{2}\right) - \frac{\sin(\phi/2)}{2\cos(\theta/2)} \right] \tag{3.5}$$

The terms θ, ϕ, and r in Figure 3.19(c) can be related by assuming that the liquid is incompressible [42]. With this assumption, the initial and final cross-sectional areas can then be set equal, giving

$$2\ w\ h = \frac{1}{2}\left[w^2 \sin(\theta) + \phi\ r^2 - r^2 \sin(\phi)\right] \tag{3.6}$$

Since $r\sin(\phi/2) = w\cos(\theta/2)$, this can be reduced to an equation that relates ϕ and θ

$$\cos^2(\theta/2)\left[\phi - \sin(\phi)\right] = \sin^2(\phi/2)\left[4\eta - \sin(\theta)\right] \tag{3.7}$$

where $\eta = h/w$ is the normalized pad height. This is an important parameter because it is comprised of the two dimensions of the meltable pad. By manipulating Equation 3.7 [40, 43], it is possible to relate the equilibrium angle, θ_e, with the normalized pad height, η

$$\eta(\theta_e) = \frac{\sin^3(\theta_e) + \left[1 + \cos(\theta_e)\right]\left[\pi - \theta_e + \sin(\theta_e)\cos(\theta_e)\right]}{4\sin^2(\theta_e)} \tag{3.8}$$

Figure 3.20 shows the variation of η with θ_e. From this curve, it is possible to determine values of h and w that are required to achieve a desired equilibrium angle. As the normalized pad height decreases, the final rotation angle increases.

For this design, the desired final angle for each rotating mirror plate is 54.7°. This is the angle each plate is required to rotate off the substrate to create a triangular-faced trihedral corner reflector. An angle of 54.7° corresponds to a normalized pad height of $\eta = 1.78$. However, it would be very difficult to fabricate the device with this exact η value and have it's final angle come out to be precisely 54.7°. It is more feasible to design for a larger final rotation angle and rely on the rotation stopping mechanisms described previously. In the layout of the triangular corner reflectors,

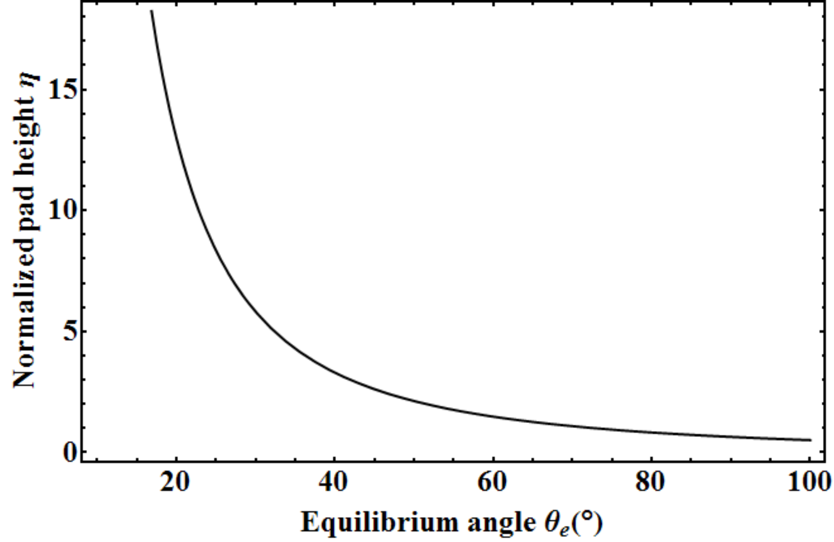

Figure 3.20: Variation of pad height with final angle.

$w = 10$ μm and h can be varied by depositing the photoresist at different thicknesses. For θ_e to be greater than 54.7°, h must be smaller than 17.8 μm.

After determining the value of η necessary for the desired rotation angle, it is important to make sure the meltable pad is long enough to rotate the mirror. The initial torque due to the surface tension of the meltable pad must be greater than the torque due to the weight of the mirror. The initial torque, T_0, occurs when $\theta = 0$ in Equation 3.5, giving

$$T_0 = l\left(\frac{\gamma\ w}{2}\right)\sin(\phi_0/2) \tag{3.9}$$

where l is the length of the meltable pad and ϕ_0 is the value of ϕ at $\theta = 0$. The maximum value of T_0 is then

$$T_{0-max} = l\frac{\gamma\ w}{2} \tag{3.10}$$

For a typical polymer photoresist, $\gamma = 0.041$ (N/m) [7]. For width $w = 10$ μm and length $l = 110$ μm, $T_{0-max} = 22.6$ pN.

The rotating mirror can be modeled as a simple trapezoid like the one shown in Figure 3.21. The torque due to the weight of the mirror, T_f, is simply the weight of the mirror times the distance from the origin, O, to the center of mass or $T_f = WR_y$.

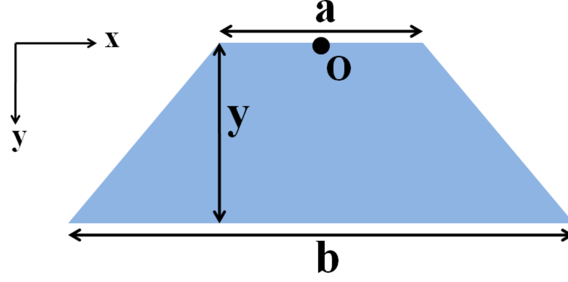

Figure 3.21: Geometry of simple trapezoid model for the rotating mirror.

The area of a trapezoid is $A = \frac{1}{2}(b + a)y$, and the volume is $V = Ad$ where d was given earlier as the thickness of the mirror plate. The weight of the trapezoid is then $W = \rho V g$, where ρ is the density of the mirror material and g is gravitational acceleration. The distance to the center of mass with respect to the origin can be shown to be

$$R_y = \frac{y(2b + a)}{3(b + a)} \tag{3.11}$$

Combining these equations, it is possible to get an expression for the torque due to the weight of the mirror in terms of a, b, y, and d as

$$T_f = \frac{1}{6}(a + 2b)d\ g\ y^2\ \rho \tag{3.12}$$

For this research, triangular corner reflectors were built using four different trapezoid sizes (see Figure 3.22) to determine which design was the best combination of size, reflectivity, ease of assembly, and robustness. The dimensions for these designs are given in Table 3.2.

For the reflectors seen earlier in Figure 3.18, the trapezoid corresponding to the photoresist pad length $l = 110$ μm (design #2) has values $a = 150$ μm, $b = 600$ μm, and $y = 225$ μm. The device layer thickness of the SOI wafer is $d = 5$ μm and the density of silicon is $\rho = 2.33 \times 10^3$ (kg/m^3). This gives a value for the torque due to the weight of the mirror as $T_f = 1.30$ pN. This torque is what the photoresist pad must overcome in order to rotate the mirror. For this design the initial available torque, found earlier to be $T_{0-max} = 22.6$ pN, is an order of magnitude greater than

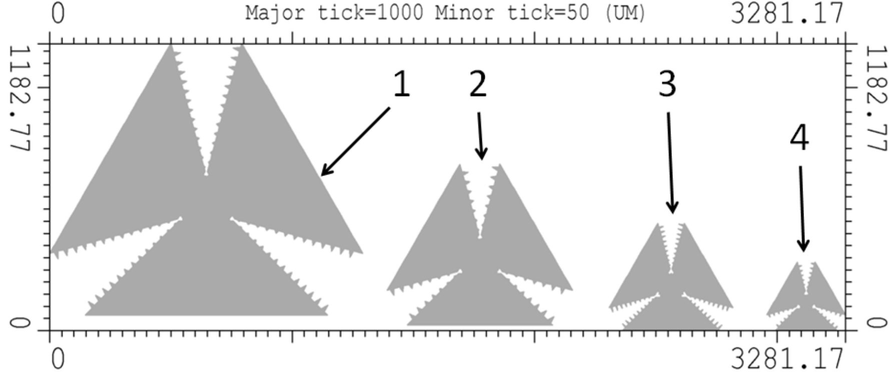

Figure 3.22: Four triangular corner reflectors designed with varying rotating mirror sizes. These designs were built to determine the best combination of size, reflectivity, ease of assembly, and robustness.

T_f. The results of these torque calculations for the other three triangular corner reflector designs can be seen in Table 3.2.

3.6 SOI Corner Reflector Fabrication

This section discusses the fabrication of corner reflectors on SOI wafers.

3.6.1 SOI Wafer. The SOI wafers for this research were obtained from Ultrasil Corporation. The device layer thickness for these wafers was 5 ± 0.5 μm, with a buried oxide layer thickness of 2 ± 0.1 μm. The handle wafer thickness was 650 ± 5 μm. The wafers come with both sides of the wafer polished, but the device layer side can be determined visually by looking for fringe lines. These fringes are

Table 3.2: Triangular corner reflector design dimensions.

Design	Mirror a (μm)	Mirror b (μm)	Mirror y (μm)	Hinge l (μm)	T_f (pN)	T_{0-max} (pN)
1	200	1000	400	160	6.70	32.8
2	150	600	225	110	1.30	22.6
3	100	400	150	60	0.386	12.3
4	50	250	100	30	0.105	6.15

caused by variations in the oxide layer thickness on the order of angstroms, and are visible in SOI wafers with device layer thicknesses less than 8 μm [45].

3.6.2 Device Layer Fabrication. The 150 mm SOI wafers were diced into 20 mm $\times$ 20 mm chips. Each chip was cleaned with acetone and methanol, then placed on a 110 °C hotplate for two minutes to bake off any remaining solvents. Next, a layer of Shipley 1805 photoresist was spun on at 4000 rpm for 30 seconds. The chip was then placed back on the 110 °C hotplate for 75 seconds to prebake the photoresist. The photoresist was patterned by exposing in a Karl Suss MJB3 mask aligner for 10 seconds, then developing for 25 seconds with a 1:5 solution of Shipley Microposit 351 developer. Layouts of the device layer masks used in this research can be seen in Figure 3.23. The mask in Figure 3.23(a) incorporates the four designs from Table 3.2. The mask in Figure 3.23(b) is used to build an array of similar devices (design #2 in Table 3.2).

At this point, the chips were sent to the AFRL Sensors Directorate for etching. This was accomplished with an Oerlikon Versaline ML DRIE, which was used to etch through the portions of the device layer not covered by photoresist. The DRIE etch process etches SiO_2 slowly enough that the oxide layer would not be substantially etched. During the DRIE process, the photoresist was often baked onto the devices. It was initially thought that Shipley 1165 photoresist stripper could remove this photoresist. However, even after one hour in 1165 (at a temperature greater than 80 °C), a thin layer of photoresist still remained. Figure 3.24(a) shows a device after the DRIE etch and a 60 minute 1165 bath. It was later found that flood exposing the chips directly after the DRIE step, then placing them in undiluted 351 developer for 10 minutes dissolved most of the baked-on 1805 photoresist. The chips were then placed in an Anatech SCE-106 barrel plasma asher to remove any residual photoresist.

3.6.3 Hinge Layer Fabrication. The hinges were created by first spinning on a layer of AZ P4620 photoresist at 2000 rpm for 60 seconds. This created a layer of photoresist approximately 10 μm thick. The photoresist was then prebaked on

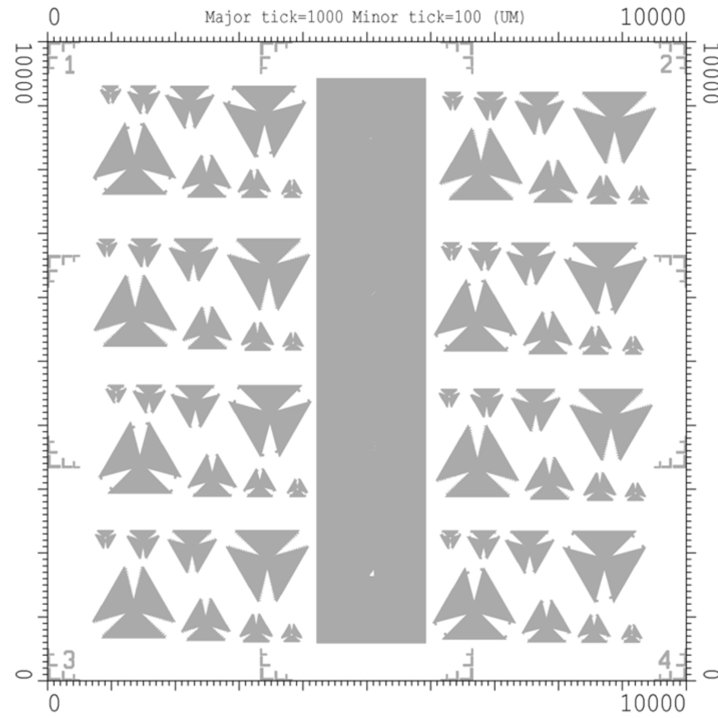

(a)

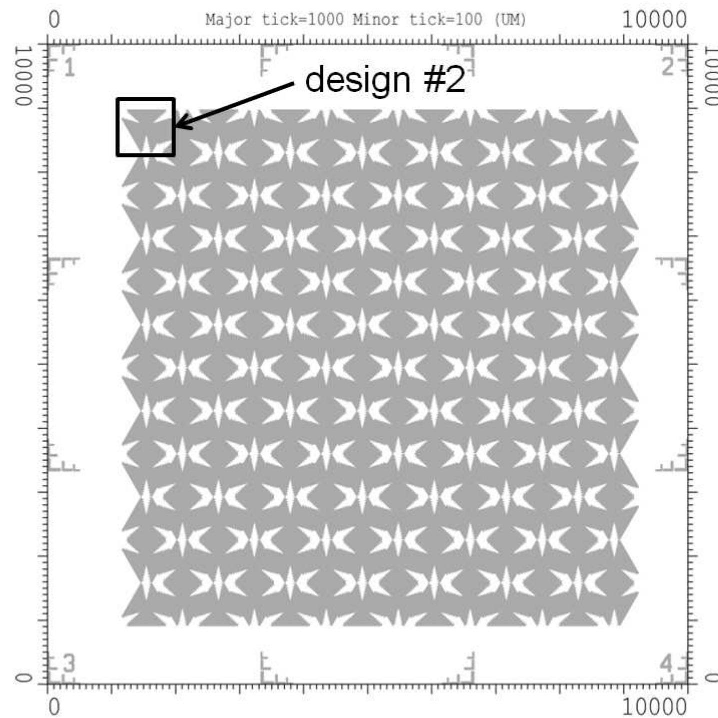

(b)

Figure 3.23: Masks used for patterning of SOI devices. (a) Device layer mask for the triangular corner reflector size test. (b) Device layer mask for the triangular corner reflector array.

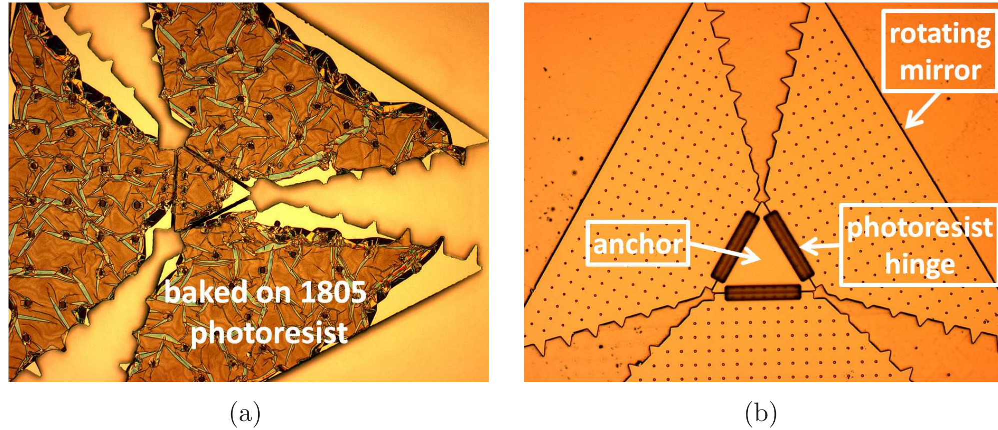

(a) (b)

Figure 3.24: (a) SOI device after DRIE etching of the device layer and a 60 minute bath in Shipley 1165 photoresist stripper. The DRIE has baked the photoresist mask, causing it to stick to the devices. (b) SOI device after patterning of the photoresist hinges.

a 110 °C hotplate for 85 seconds. Next, the photoresist was patterned with an EV Group EVG620 mask aligner at a constant dose of 200 mJ/cm^2 and developed with a 1:4 solution of AZ 400K for 90 seconds. To promote adhesion of the photoresist to the device layer silicon, the chips were then placed on a 100 °C hotplate for 30 minutes. Figure 3.24(b) shows a device at this step in the fabrication process.

3.6.4 Release and Self-Assembly. The completed devices were released in 49% HF for 15 minutes. Because the 4620 photoresist dissolves in solvents, the chips must be placed only in distilled water after the HF bath, then dried on a hotplate. Freeze drying in a CO_2 dryer was not possible because the 4620 photoresist would detach from the devices in methanol.

After the release, the photoresist hinges were expected to reflow at ∼150 °C, causing the mirrors to rotate into place. The chips were placed on a 150 °C hotplate for 10 minutes, but no rotation occurred. The temperature was increased every two minutes by 5 °C increments up to 250 °C, but there was never any rotation. Because the chips were dried on a hotplate and not in a CO_2 dryer, it is possible that stiction forces from remaining water molecules kept the mirrors from rotating.

Another chip was fabricated in the same manner, except SU-8 photoresist was used for the hinges instead of AZ P4620. SU-8 is a negative photoresist, while 4620 is a positive photoresist. In addition, SU-8 does not dissolve in solvents, allowing the released device to be freeze dried in a CO_2 dryer. After release and drying of these devices, it was apparent that the individual rotating mirror elements were slightly deflected. This indicated that the rotating mirrors were fully released. This initial deflection was never seen after releasing devices with AZ P4620 hinges.

Unfortunately, SU-8 does not make a good photoresist hinge for surface tension self-assembly because it does not necessarily reflow at higher temperatures. However, it seems that a negative photoresist may be a better hinge material. Upon further inspection of the device using 4620 hinges, it appears that some photoresist is still present in the rotating mirror etch holes. During exposure of the 4620, photoresist in these etch holes may not have been exposed enough to allow for removal during the development process. This photoresist prevents the flow of HF through the etch holes, keeping the mirrors from being properly released. While exposure dose could be increased, this would also reduce the size of the photoresist hinges. With a negative photoresist, any unexposed photoresist is easily washed away by developer. Etch hole photoresist removal is not related to exposure dose, as only the exposed hinges remain after development.

3.6.5 Gold Sputter Coat. Because the corner reflectors never assembled, the gold sputtering step was not completed.

3.7 Factors Effecting Reflectivity of MEMS Corner Reflectors

This section discusses the main causes of reflectivity losses in MEMS micromirrors. First, the losses due to etch holes in the mirrors are discussed. Etch holes in a mirror structure reduce the amount of reflective surface area. It is also necessary to consider diffraction losses caused by the etch holes and their spacing. Reflectivity loss due to surface roughness will also be discussed.

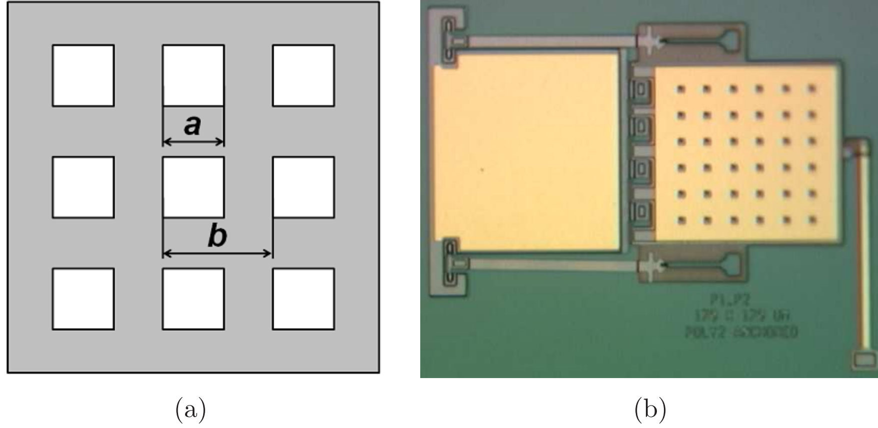

(a) (b)

Figure 3.25: Layout and image of a MEMS micromirror with square etch holes. (a) Layout of the periodic pattern of the etch holes. The etch hole size and spacing are represented by a and b, respectively. (b) An image of a MEMS micromirror with etch holes. For this mirror, $a = 3$ μm and $b = 25$ μm.

3.7.1 Losses Due to Etch Holes. The losses due to etch holes in a MEMS micromirror can be attributed to both the loss of mirror surface area and diffraction effects. A layout and image of a MEMS micromirror with square etch holes can be seen in Figure 3.25. In this case, the etch holes have sides of length a, and the period of the array is b. The filling factor, or the loss of mirror surface area due to the etch holes, is then a^2/b^2.

Determining the loss due to diffraction is not as straightforward. However, the problem can be simplified by using the Fraunhofer approximation. The diffraction caused by the etch hole array is analogous to the case where a uniform plane wave is diffracted by a crossed grating [44]. Using the Fraunhofer approximation, the diffracted intensity can be obtained by finding the Fourier transform of the 2-D etch hole array. This approximation is valid provided the "antenna designer's formula" is satisfied [11]. This formula states that for an aperture of linear dimension, D, the Fraunhofer approximation is valid if the observation distance, z, satisfies

$$z > \frac{2D^2}{\lambda} \tag{3.13}$$

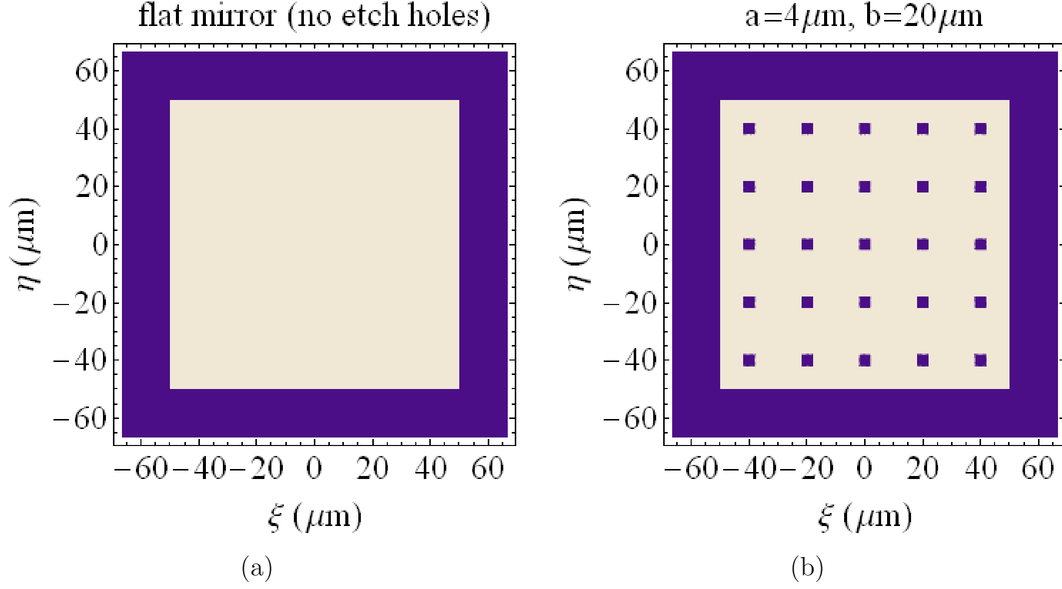

Figure 3.26: Amplitude transmittance functions for (a) a flat mirror and (b) a MEMS micromirror with etch holes.

For this reason, Fraunhofer diffraction is also known as far-field diffraction. In the case of a micromirror with sides of length, $D = 100$ μm, reflecting a wavelength, $\lambda = 632.8$ nm, z must be greater than 3.16 cm. In the case of the photonic Doppler velocimeter, $\lambda = 1550$ nm, requiring $z > 1.29$ cm.

First, it is necessary to consider the diffraction of a perfectly flat mirror. This mirror has no etch holes and its reflectance is $\rho = 1$. It can be modeled as a square aperture. The amplitude transmittance, t_A, is the same for a square mirror and a square aperture, and is given by

$$t_A(\xi, \eta) = \text{rect}\left(\frac{\xi}{D}\right) \text{rect}\left(\frac{\eta}{D}\right) \tag{3.14}$$

where D is the width of the mirror in the (ξ, η) plane. The model of this transmittance function can be seen in Figure 3.26(a). For this example, the mirror has sides of length $D = 100$ μm.

Assuming the mirror is illuminated at normal incidence by a monochromatic plane wave of unit amplitude, the field distribution, $U(\xi, \eta)$, is equal to the transmit-

tance function, $t_A(\xi, \eta)$. The Fraunhofer diffraction pattern is then

$$U(x,y) = \frac{e^{jkz} e^{j\frac{k}{2z}(x^2+y^2)}}{j\lambda z} \mathcal{F}[U(\xi,\eta)]_{f_X=x/\lambda z,\ f_Y=y/\lambda z} \tag{3.15}$$

where $U(x, y)$ is the field distribution in the (x, y) plane, which is a distance z from the (ξ, η) plane.

The terms in front of the Fourier transform pertain only to the amplitude of the field. Since the normalized intensity pattern is desired, these terms can be dropped for this derivation. In this case, the diffraction pattern is simply

$$U(x,y) = \mathcal{F}[U(\xi,\eta)]_{f_X=x/\lambda z,\ f_Y=y/\lambda z} \tag{3.16}$$

It can be shown that

$$\mathcal{F}[U(\xi,\eta)] = A \operatorname{sinc}(D\ f_X)\ \operatorname{sinc}(D\ f_Y) \tag{3.17}$$

where A is the area of the mirror. Once again, this term only pertains to the amplitude of the field and will be dropped, giving a field of

$$U(x,y) = \operatorname{sinc}\left(\frac{x\ D}{\lambda\ z}\right)\ \operatorname{sinc}\left(\frac{y\ D}{\lambda\ z}\right) \tag{3.18}$$

For a given field, the intensity is

$$I(x,y) = |U(x,y)|^2 \tag{3.19}$$

For the flat mirror, this gives an intensity distribution of

$$I(x,y) = \operatorname{sinc}^2\left(\frac{x\ D}{\lambda\ z}\right)\ \operatorname{sinc}^2\left(\frac{y\ D}{\lambda\ z}\right) \tag{3.20}$$

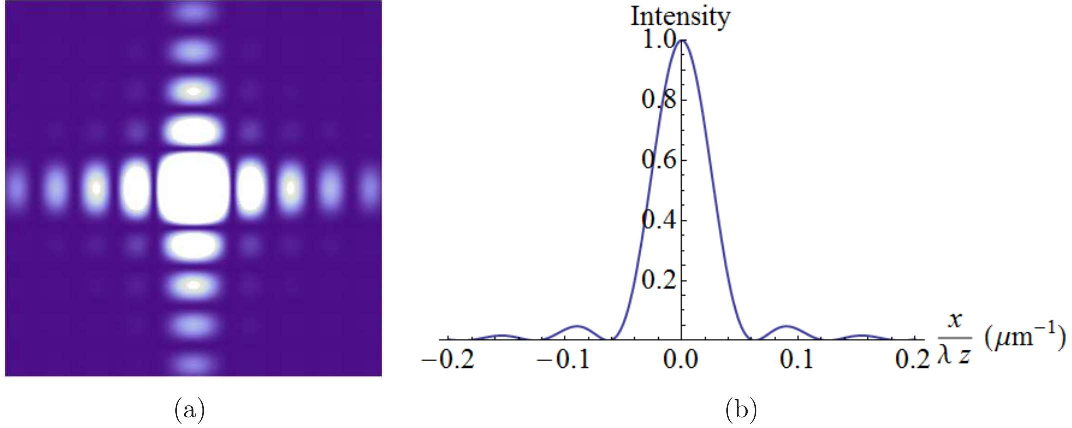

Figure 3.27: (a) Calculated Fraunhofer diffraction pattern of a square flat mirror with sides of length $D = 100$ μm. (b) Normalized intensity cross section of this diffraction pattern.

This diffraction pattern, along with its normalized intensity cross section, can be seen in Figure 3.27.

The amplitude transmittance (and field distribution) of the mirror with etch holes is only slightly more complicated than the flat mirror, and is represented by

$$\begin{aligned} t_A(\xi,\eta) &= \left[1 - \sum_{n=-N}^{N} \text{rect}\left(\frac{\xi + b\,n}{a}\right) \sum_{n=-N}^{N} \text{rect}\left(\frac{\eta + b\,n}{a}\right)\right] \\ &\quad \times \text{rect}\left(\frac{\xi}{D}\right) \text{rect}\left(\frac{\eta}{D}\right) \end{aligned} \tag{3.21}$$

where N is the number of etch holes in the ξ or η direction ($N = D/b$). The model of this transmittance function can be seen in Figure 3.26(b). For this example, like that of the flat mirror, $D = 100$ μm.

The intensity distribution for the mirror with etch holes is found the same way as the distribution for the flat mirror. However, the Fourier transform of the amplitude transmittance in Equation 3.21 is more complicated. This transform was calculated using Wolfram Mathematica® software and the resulting Fraunhofer diffraction pattern is shown in Figure 3.28(a). The cross section of this diffraction pattern can be

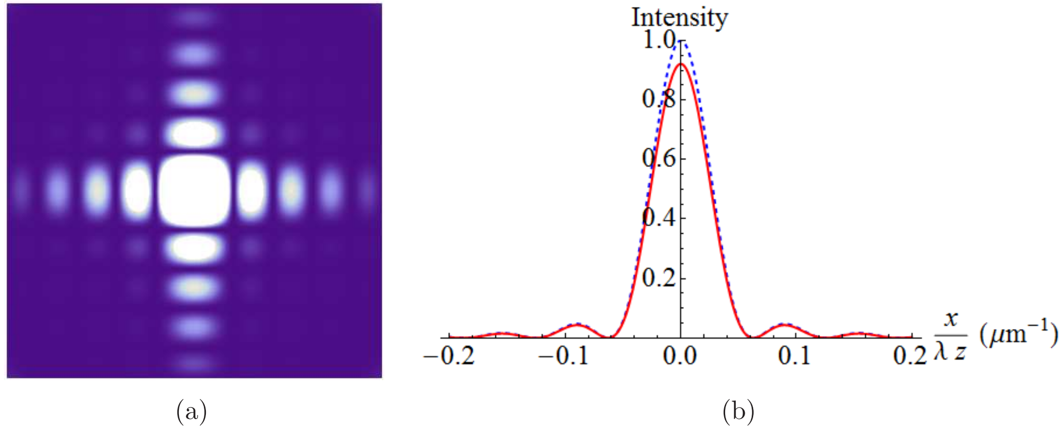

(a) (b)

Figure 3.28: (a) Calculated Fraunhofer diffraction pattern of a square mirror with etch holes and sides of length $D = 100\ \mu$m. (b) Cross section of this diffraction pattern (red line) normalized to the flat mirror intensity (dashed line).

seen in Figure 3.28(b). Here, it has been plotted normalized to the flat mirror cross section.

It is apparent in Figure 3.28(b) that there are losses in the mirror with etch holes when compared to the flat mirror. The loss due to the etch holes can be estimated by subtracting the area under the main peak of the mirror with etch holes from the area under the main peak of the flat mirror. This gives the total loss due to both diffraction and the filling factor. The diffraction loss can then be found by subtracting the filling factor loss from the total loss.

Theoretical loss components for mirrors with varying etch hole dimensions and constant etch hole spacing can be found in Table 3.3. Theoretical loss components for mirrors with varying etch hole spacing and constant etch hole dimensions can be seen in Table 3.4. From these tables, it can be seen that diffraction and filling factor losses decrease with smaller etch holes. While using smaller etch holes can increase micromirror reflectivity, it also increases the time required to completely release the device.

3.7.2 Losses Due to Surface Roughness. Surface roughness is a measure of the topographic relief of a surface [5]. Surface roughness can be caused by any

Table 3.3: Theoretical loss components for mirrors with varying etch hole dimensions and constant etch hole spacing.

Etch hole size (μm)	Etch hole spacing (μm)	Filling factor loss	Diffraction loss	Reflectivity vs. flat mirror
2	20	0.01	0.0102	0.9798
3	20	0.0225	0.0226	0.9549
4	20	0.04	0.0395	0.9205
6	20	0.09	0.0841	0.8259
8	20	0.16	0.1378	0.7022
10	20	0.25	0.1917	0.5583

Table 3.4: Theoretical loss components for mirrors with varying etch hole spacing constant etch hole dimension.

Etch hole spacing (μm)	Etch hole size (μm)	Filling factor loss	Diffraction loss	Reflectivity vs. flat mirror
10	4	0.16	0.1334	0.7066
12	4	0.1111	0.1141	0.7748
14	4	0.0816	0.0729	0.8455
16	4	0.0625	0.0720	0.8655
18	4	0.0494	0.0378	0.9128
20	4	0.04	0.0395	0.9205

deviation from a smooth surface. These variations from a perfectly smooth surface cause light to scatter off the surface, decreasing overall reflectivity. Scratches and dust particles are typically the most visible defects on a surface. However, in this research, the concern will be microirregularities such as polishing marks on optical surfaces or machining marks on machined surfaces.

Increased surface roughness leads to a decrease in specular reflectance. Using the scalar scattering theory [5], the specular surface reflectance, R_{spec}, can be estimated as

$$R_{spec} = R_0 \; e^{-(4\pi\delta \sin\theta_i/\lambda)^2} \tag{3.22}$$

where R_0 is the total reflectance from the surface, δ is the root-mean-square (rms) surface roughness, θ_i is the angle of the incident light from the surface normal, and λ is the incident wavelength.

It is important to notice that Equation 3.22 is highly dependent on the rms roughness, δ. This measurement can be obtained from a cross section measurement of a surface, like the one shown in Figure 3.29. The profile measurement is taken along a line of length, L. Variations in the surface height are measured perpendicular to L in the $\pm z$ directions, while the xy plane is the surface plane. The mean surface level along L is defined such that

$$\sum_{i=1}^{N} z_i = 0 \tag{3.23}$$

where N is the number of discrete, equally spaced, measured points along L.

The rms roughness, δ, is then defined as the square root of the mean value of the squares of the distances z_i of the points from the mean surface level [5], or

$$\delta = \sqrt{\frac{1}{N}\sum_{i=1}^{N} {z_i}^2} \tag{3.24}$$

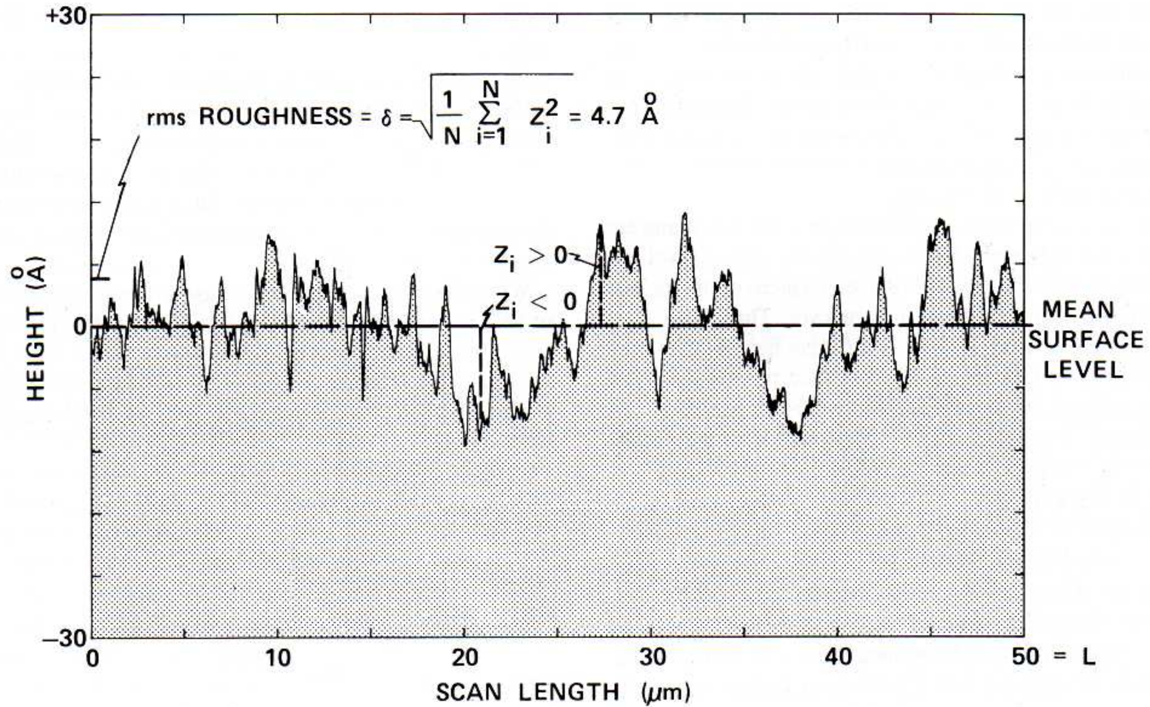

Figure 3.29: An example cross section of a surface profile measurement for a smooth surface. [5]

Notice that the mean surface level must be calculated first in order to calculate the rms surface roughness.

The rms surface roughness will vary depending on what location on the surface the cross-section profile was measured. Because of this, it is important to take multiple measurements and determine an average rms surface roughness, δ_{AV}. The average deviation is then

$$\text{Average deviation} = \frac{1}{N}\sum_{i=1}^{N} |\delta_i - \delta_{AV}| \tag{3.25}$$

It has been found [5] that for polished surfaces a typical ratio is

$$\text{Average deviation}/\delta_{AV} \approx 0.10 \text{ to } 0.20 \tag{3.26}$$

It is then necessary to take enough profile measurements to satisfy this criterion.

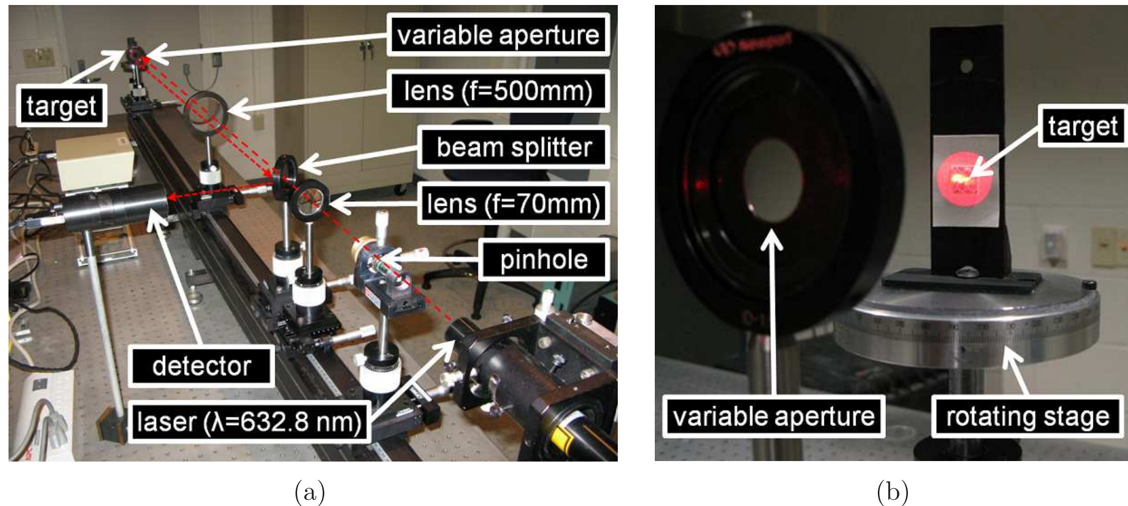

(a) (b)

Figure 3.30: (a) Optical cross section measurement setup. (b) Close up of the target and rotating stage.

3.8 Optical Measurement Methodology

This section describes the optical measurements used in this research. OCS measurement methodology is described first, including pictures of the optical test setup. The BRDF measurement methodology is then discussed.

3.8.1 Optical Cross Section Methodology.

The OCS measurement setup can be seen in Figure 3.30. A He:Ne laser beam is sent through a pinhole spatial filter. The beam is then collimated by the $f = 70$ mm and $f = 500$ mm lenses. At this point, the beam is sufficiently collimated, but only a small portion in the center is uniform enough to be used for OCS measurements. The variable aperture is set to allow only the portion of the beam that meets the uniformity requirements to illuminate the target plane. The target is placed on a rotating platform which displays its angle with respect to the incident beam. The target is at a rotation angle of 0° when it is normal to the beam propagation direction. The reflected beam is then bounced off a beam splitter to an EG&G 450 detector, which measures the reflected power (Φ_{e-refl}).

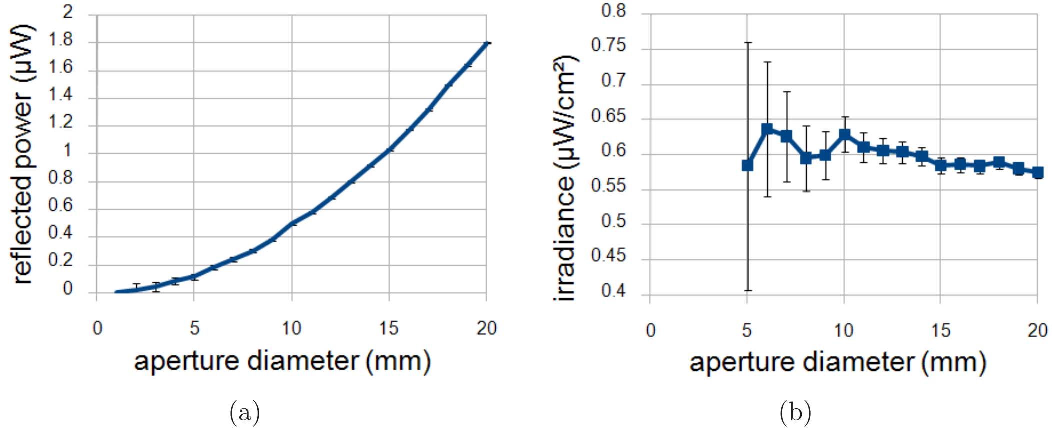

(a) (b)

Figure 3.31: (a) Reflected power vs. aperture diameter for a flat mirror ($\rho \approx 1$). (b) Calculated incident irradiance vs. aperture diameter for a flat mirror.

Before taking any OCS measurements, it was necessary to determine whether the differential OCS or total OCS was more appropriate. As stated in Chapter II, if the diffraction pattern is much greater than the receiver collecting aperture, or $\frac{R\lambda}{a_{tar}} \gg a_{rcv}$, it is appropriate to use the DOCS. If $\frac{R\lambda}{a_{tar}} \ll a_{rcv}$, the TOCS must be used. For this research, the reflective tape samples tested were all 10 mm $\times$ 10 mm, or $a_{tar} = 5$ mm. The size of the limiting receiver collecting aperture (the $f = 500$ mm lens) was $a_{rcv} = 4$ cm and the laser interrogation wavelength was $\lambda = 632.8$ nm. The required range to use the TOCS is then $R \ll 316$ m. Here, the distance from the target to the receiver collecting aperture was $R \approx 1$ m, so TOCS was appropriate.

To test the beam uniformity, a flat mirror ($\rho \approx 1$) was placed on the rotating stage at 0° (normal to the incident beam). The diameter of the variable aperture was then increased from 5 mm to 20 mm in 1 mm increments. The reflected power at the detector was recorded and plotted in Figure 3.31(a). The effective incident irradiance at the target (E_{e-tar}) can then be found by dividing the detected power by the aperture diameter. The irradiance calculated for each beam diameter is shown in Figure 3.31(b). The large error for smaller aperture diameters is due to the uncertainty in the aperture diameter measurement. This uncertainty becomes less of a factor as the aperture diameter increases.

As discussed in Chapter II, the beam irradiance must not deviate by more than 15% of the mean over the entire area. As expected, the deviation from the mean irradiance was greatest (4.49%) at an aperture diameter of 20 mm. This deviation is well below 15%, so the beam is sufficiently uniform at a diameter of 20 mm. At this diameter, the calculated mean irradiance is $E_{e-tar} = 0.6015\ \mu\text{W/cm}^2$.

From Equation 2.9, the three terms needed to calculate optical cross section are Φ_{e-refl}, Ω_{refl}, and E_{e-tar}. The detected power is Φ_{e-refl}, and E_{e-tar} was just calculated above. The final term required to calculate OCS is Ω_{refl}. This term can easily be found by using Equation 2.4, which states $\Omega = A/r^2$. For this measurement, A is the area of the collecting optic and r is the distance from the target to the collecting optic. The collecting optic is the $f = 500$ mm lens, which has a diameter $D_{opt} = 80 \pm 0.5$ mm. The distance from the target to the $f = 500$ mm lens was measured to be 122 ± 0.2 cm. The solid angle is then

$$\Omega_{refl} = \frac{\pi D_{opt}^2}{4r^2} = \frac{\pi(80 \pm 0.5\text{ mm})^2}{4(122 \pm 0.2\text{ cm})^2} = 3.4 \pm 0.04\text{ msr} \tag{3.27}$$

When measuring TOCS, Ω_{refl} is typically calculated by estimating the size of the diffraction pattern. In Equation 3.27, Ω_{refl} was calculated using the area of the limiting optic and the distance from the target. However, this calculation of Ω_{refl} would only be valid if DOCS was being measured. Since TOCS is being measured in this test setup, it has already been established that all of the retroreflected power is being collected by receiving optic. If D_{opt} were increased, there would be no increase in the collected power, Φ_{e-refl}. For this setup, a "perceived" OCS (POCS) can be obtained by disregarding the solid angle. This gives an expression for the target's POCS as

$$\text{POCS} = \frac{\Phi_{e-refl}}{E_{e-tar}}\ (\text{m}^2) \tag{3.28}$$

Equation 3.28 gives a more intuitive value for the samples tested in this research. For the case of a 10 mm × 10 mm perfectly flat mirror, the POCS would be 100 mm^2.

This POCS value is simply the cross sectional area of the mirror. The POCS measurements for any 10 mm $\times$ 10 mm retroreflector sample can then be looked at as the perceived cross sectional area of the sample. The POCS measurement allows for direct comparison of the performance of any retroreflector sample to a flat mirror of the same size.

As the samples are being rotated, the cross sectional area of the sample normal to the incident beam is being reduced. For a square sample, this cross sectional area is simply the sample area multiplied by $\cos\theta_i$. The sample's POCS measurements can then be normalized, written as

$$\text{POCS}_{norm} = \frac{\Phi_{e-refl}}{E_{e-tar}\cos\theta_i}\ (\text{m}^2) \tag{3.29}$$

3.8.2 Bidirectional Reflectance Distribution Methodology. The BRDF measurements for this research were completed using a Complete Angle Scatter Instrument (CASI) from Schmitt Measurement Systems, Inc. The CASI scatterometer uses laser light ($\lambda = 544$ nm for this setup) as a nondestructive probe which can be used to measure many material properties such as surface quality, smoothness, contamination, etc. Each retroreflector design can be tested individually using the CASI.

To measure the BRDF using the CASI, a sample is placed on a rotating stage. As the stage is rotated, a detector sweeps around the sample recording the measured light it sees at each rotation angle. While this process is completely automated, it is somewhat time intensive (4-8 hours). More time is required if a higher resolution measurement is desired. Figure 3.32 shows the CASI setup as it tested the gold coated RF30 reflector sample.

3.9 Chapter Summary

This chapter discussed the methodology behind the design and testing of retroreflectors used in this research. First, the COTS retroreflectors were analyzed, including the designs of both the retroreflective tape samples and the RF30 reflector. Metal

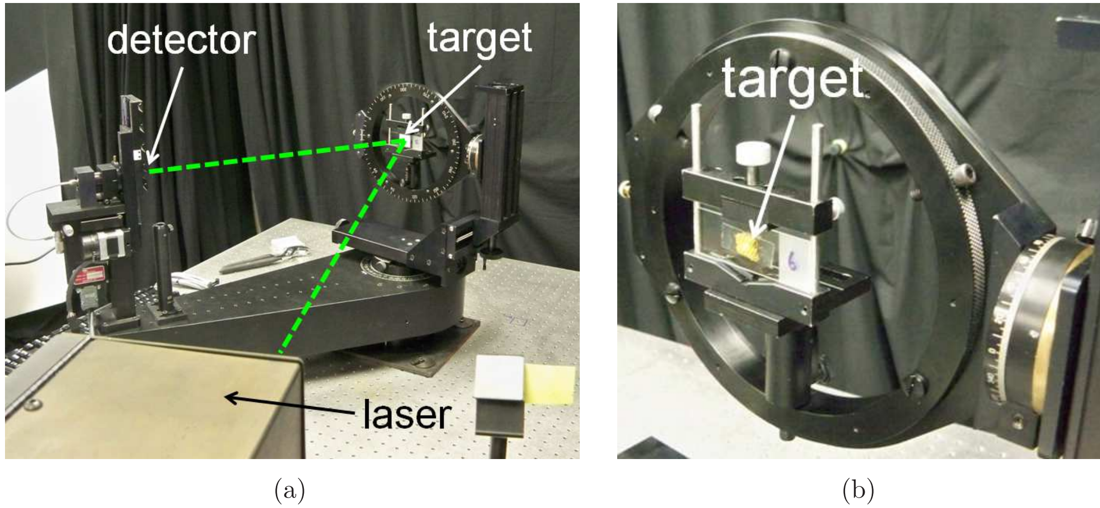

(a) (b)

Figure 3.32: Complete Angle Scattering Instrument (CASI) BRDF measurement setup. (a) The CASI laser illuminates the target as the detector stage rotates around the sample. (b) Close up of the target stage.

deposition on all COTS reflectors was then discussed. Next, both the MUMPs© and SOI corner reflector design and fabrication processes were covered in detail. Losses due to surface roughness and diffraction were then derived. Finally, the OCS and BRDF measurement test setups were described.

IV. Results and Analysis

This chapter presents the results of various tests performed on the retroreflective designs discussed in the previous chapters. These tests included curvature measurements of the MUMPs© mirrors (with and without the PolyMUMPs™ Metal layer), roughness measurements of sputtered coated gold, and OCS and BRDF measurements of all the possible retroreflector solutions.

4.1 MUMPs© Mirror Curvature Measurements

A Zygo white light interferometer was used to measure the curvature of the MUMPs© mirror modeled in Figure 3.6, as well as a MUMPs© mirror without the Metal layer. The results of these measurements can be seen in Figure 4.1. As expected from the model, the mirror with the PolyMUMPs™ Metal layer has very large curvature compared to the mirror without the Metal layer.

Cross sections of the surface profile data from the Zygo measurements are shown in Figure 4.2. From these figures, it is clear that the PolyMUMPs™ Metal layer has greatly increased the curvature of the mirror. The mirror without the Metal layer is relatively flat, and its curvature is almost within the noise margin of the Zygo.

From the cross section profiles in Figure 4.2, it is possible to extract an approximate radius of curvature for each mirror. For a plane curve given as $y = f(x)$, the curvature, κ, is defined as

$$\kappa = \frac{|y''|}{(1 + y'^2)^{3/2}} \tag{4.1}$$

In this case, the slope, y', is small compared with unity, so the curvature can be approximated as

$$\kappa \approx \left| \frac{d^2 y}{dx^2} \right| \tag{4.2}$$

The radius of curvature is then $R = 1/\kappa$. A least-squares fit to the profiles in Figure 4.2 was found as a function $y = f(x)$ for both mirrors. The resulting radii of curvature were 0.94 cm for the mirror with the Metal layer and 28 cm for the mirror without. According to Hsu et al. [18], corner reflector performance is significantly de-

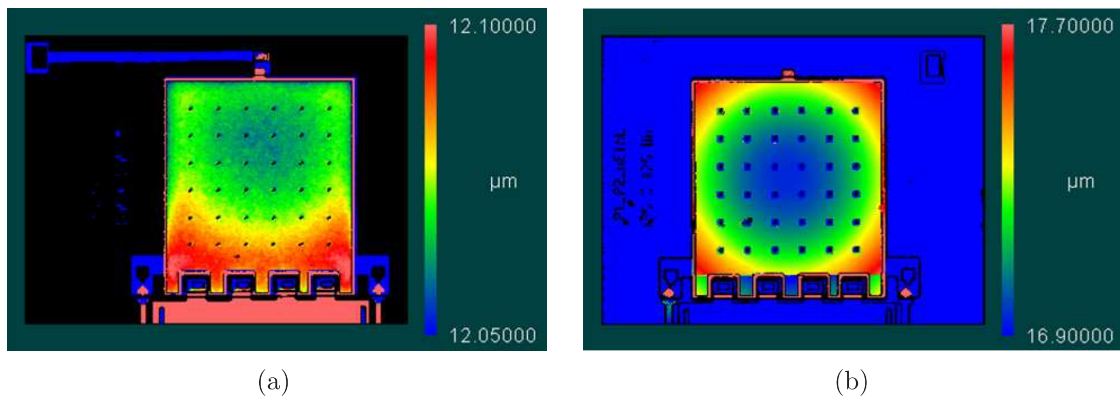

(a) (b)

Figure 4.1: MUMPs© mirror curvature measurements. (a) The mirror structure without the PolyMUMPs™ Metal layer. (b) The mirror with the PolyMUMPs™ Metal layer.

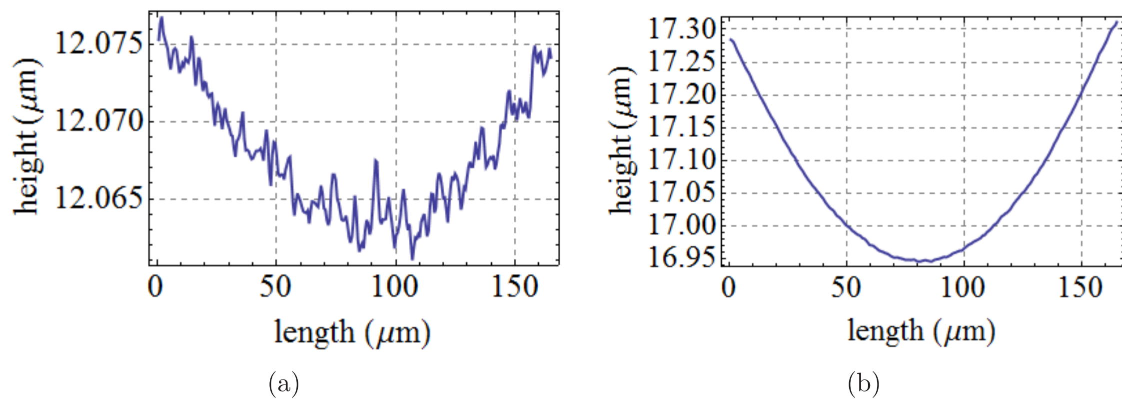

(a) (b)

Figure 4.2: Cross section of MUMPs© mirror curvature measurements. (a) The mirror structure without the PolyMUMPs™ Metal layer. (b) The mirror with the PolyMUMPs™ Metal layer.

graded when the radius of curvature falls below 20 cm. Therefore, the PolyMUMPs™ Metal layer is unacceptable for use on corner reflector mirrors.

4.2 Roughness Measurements of PolyMUMPs™ and Sputtered Gold Layers

Surface profiles of gold layers were taken with a Digital Instruments Dimension 3100 atomic force microscope in tapping mode. Among the items tested were a sample SOI wafer and a piece of the plastic RF30 reflector, both of which had been coated with 100 nm of sputtered gold. In addition, a MUMPs© mirror with the PolyMUMPs™ Metal layer was also tested to compare the roughnesses of sputter coated and PolyMUMPs™ gold layers. Each sample was given a surface profile scan in five random locations. An example profile measurement cross section for each test item is shown in Figure 4.3.

Results of surface roughness calculations for each sample can be found in Table 4.1. All of the surfaces were found to be relatively smooth. Because of this, reflectivity losses due to surface roughness (calculated for $\lambda = 632.8$ nm and an incident angle of 30° from the surface normal) were negligible. These losses are even smaller when calculated for the intended PDV wavelength of 1550 nm. However, the losses calculated here are only due to surface roughness on the micro level. Scratches, dust particles, and other larger imperfections can cause significant reflectivity losses.

Table 4.1: Gold layer surface roughness measurements (reflectivity losses calculated for $\lambda = 632.8$ nm).

Sample	# of Scans	Average Roughness (nm)	Average Deviation (nm)	Reflectivity Loss Due to Surface Roughness ($\theta_i = 30°$)
SOI (sputtered Au)	5	6.863	0.0708	0.0046
RF30 (sputtered Au)	5	11.21	0.0721	0.0123
PolyMUMPs™ Au	5	12.84	0.1261	0.0161

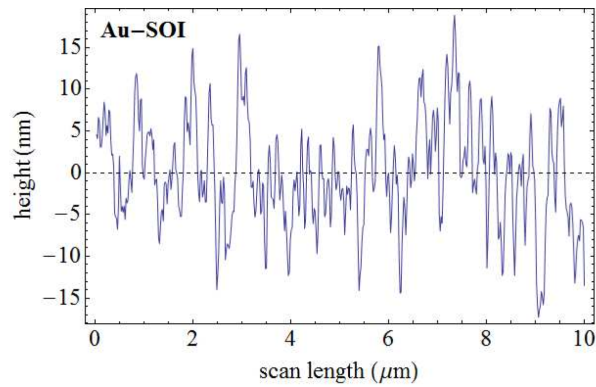

(a)

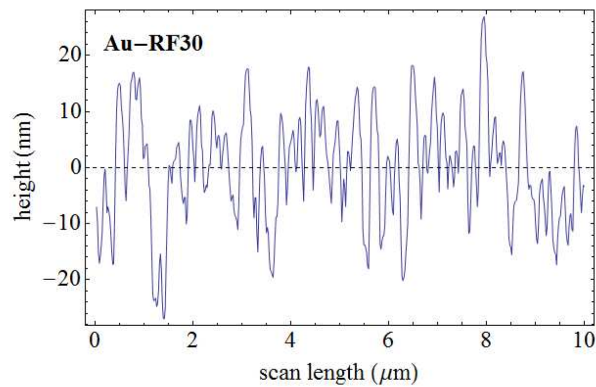

(b)

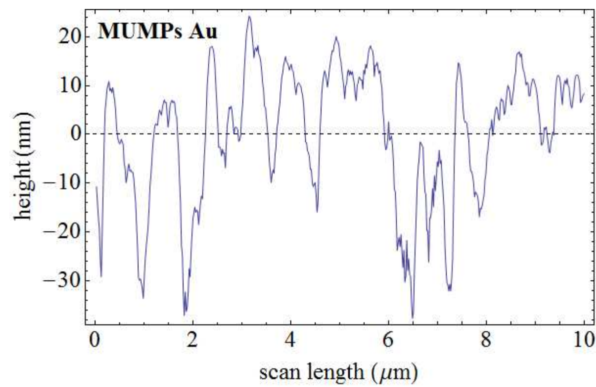

(c)

Figure 4.3: Gold layer surface profile cross sections. (a) Sputter coated gold on the device layer of a sample SOI wafer. (b) Sputter coated gold on a Telemecanique RF30 reflector. (c) PolyMUMPs™ gold layer on a micromirror.

4.3 Optical Cross Section Measurements

OCS measurements were performed using the test setup discussed in Chapter III (see Figure 3.30). Each sample was placed on the rotating stage and illuminated completely by the incident beam. As the sample was rotated, the detector reading was recorded at every 1° increment. Results from these tests are presented in this section.

4.3.1 OCS of Retroreflective Tapes. The retroreflective tape samples tested were shown in Figure 3.2. The samples were all 10 mm × 10 mm. The results of the normalized POCS measurements (see Equation 3.29) can be seen in Figure 4.4. It is immediately clear that the tapes using corner reflector elements (3M 3000X and Telemecanique XUZB11) are far more efficient at returning incident light near the surface normal. However, the spherical element tapes (Telemecanique RF7590, RF7610, and RF3870) remain sufficiently retroreflective at higher incident angles. In fact, RF7610 appears to become increasingly retroreflective until $\theta_i \approx \pm 25°$. This is most likely due to the effective fill factor density of the spherical elements (as seen by the incident beam) increasing with θ_i. As more of the incident light is collected by these spherical elements, more light is retroreflected. Retroreflection begins to decrease as θ_i becomes so large that the spherical elements begin to block incident light from each other. RF3870 displays this same phenomenon, although to a much lesser extent. However, RF7590 does not, possibly due to its very low spherical element density.

It is also easy to tell which tapes have a protective coating because these samples all have a reflection spike at normal incidence ($\theta_i = 0$). Here, the specular reflection of the coating propagates back to the detector along with the retroreflected return. This specular reflection is significant compared to the retroreflected return. Not only do these protective coatings cause unwanted specular reflections, but they also reduce retroreflectivity of the tapes. Any incident light that is reflected specularly can never

reach the retroreflective sphere or corner elements, thus reducing the retroreflected power.

The secondary spikes in the corner element tapes are caused by two-bounce and one-bounce reflections off the individual corner reflector sides. This phenomenon can also be seen in radar cross section measurements of trihedral corner reflectors (commonly called "Batman ears") [20]. Only the one-bounce spikes can be seen in the 3M 3000X, while both the one- and two-bounce spikes are seen with the XUZB11.

From these OCS measurements, the Telemecanique RF7610 would be the best tape solution for a triaxial PDV system due to its high retroreflection, large return vs. incident angle, and lack of specular reflection.

4.3.2 OCS of Gold Plated Reflector. The OCS measurement of the gold plated RF30 reflector is shown in Figure 4.4(f). It was expected that the sputter coated RF30 corner reflector array would yield a similar return to that of the corner element retroreflective tapes. However, this was not exactly the case. The maximum OCS of the RF30 was slightly less than either the 3M 3000X or the XUZB11 tape. In this case, the thickness of the sputtered gold layer (100 nm) was still thin enough to allow some transmission of the incident light through the transparent reflector. The reflectivity of each mirror was therefore reduced, as was the total retroreflected power.

Also, the return of the RF30 drops off more rapidly with incident angle. This may be due to the arrangement of the corner elements in the tapes. The individual corner reflectors in both tapes are arranged somewhat randomly so that all of the elements are not aligned. It is believed that this arrangement helps to spread out the retroreflective return with respect to incident angle. Because the RF30 corner elements are all aligned, its cross section measurement is markedly asymmetric. When the RF30 sample was flipped horizontally, the same OCS data was recorded, except the incident angles were inverted. In other words, the same waveform was seen, but flipped horizontally. Finally, the one- and two-bounce spikes are much larger for the gold coated RF30. It is believed that the arrangement of the tape elements, along

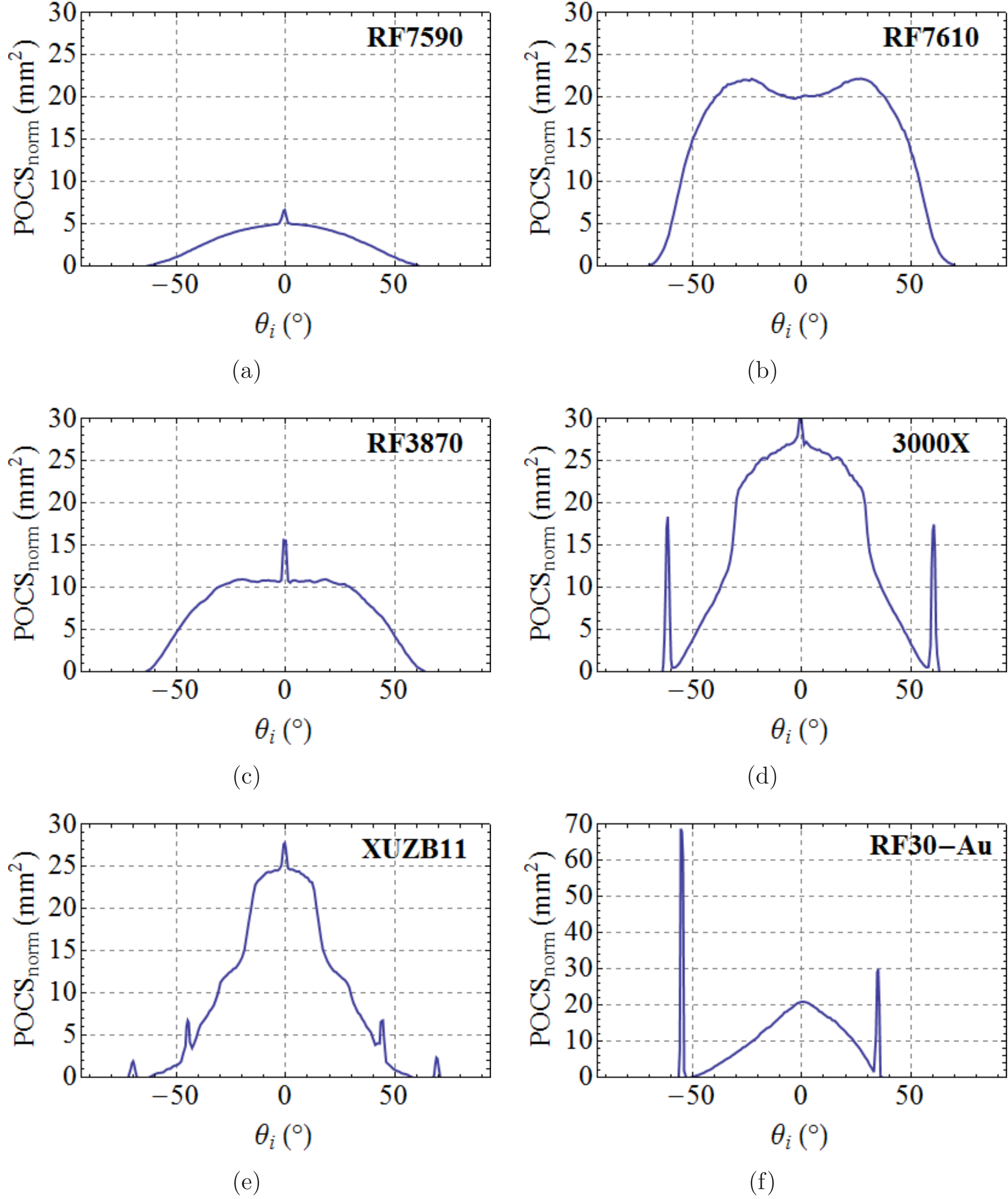

Figure 4.4: Normalized perceived optical cross section measurements for retroreflective tape samples and the gold sputtered RF30 reflector. (a) Telemecanique RF7590. (b) Telemecanique RF7610. (c) Telemecanique RF3870. (d) 3M 3000X. (e) Telemecanique XUZB11. (f) RF30 reflector with 100 nm thick layer of sputtered gold.

with losses in the protective coating, greatly reduce the one- and two-bounce spikes of the retroreflective tapes.

4.3.3 OCS of PolyMUMPs^{TM} Corner Reflector.

Due to the amount of time required to assemble just one MUMPs© corner reflector, assembling an array of corner reflectors was not practical. The returned power from the assembled MUMPs© corner reflector could not be detected. No OCS measurements were completed for the MUMPs© corner reflector.

4.3.4 OCS of SOI Triangular Corner Reflectors.

Self-assembly of the SOI corner reflectors was not successful. Because of this, an SOI corner reflector array was not available for OCS measurements.

4.4 Bidirectional Reflectance Distribution Measurements

BRDF measurements were completed by the CASI scatterometer setup described in Chapter III. Unfortunately, in this configuration the CASI cannot give retroreflection data. As the detector rotates through the incident angle, it blocks the interrogating laser. This causes data loss for approximately $\pm$ 4° about the incident angle. However, the CASI does provide accurate measurements for all other angles. This data shows the magnitude of specular reflections and other light scatter. Results from CASI BRDF measurements are presented in this section.

4.4.1 BRDF of Retroreflective Tapes.

The retroreflective tape samples used in the OCS measurements were also used in the CASI BRDF tests. Results of these tests are shown in Figures 4.5-4.9. As expected, the retroreflective returns are mostly unseen by the CASI due to the detector blocking the incident beam. More importantly, these figures show the large specular reflections caused by the protective coatings on all the tape samples except RF7610.

Figure 4.10 shows density plots of the Telemecanique RF7590 and RF7610 samples. Both of these tapes consist of spherical reflecting elements, but RF7590 has a

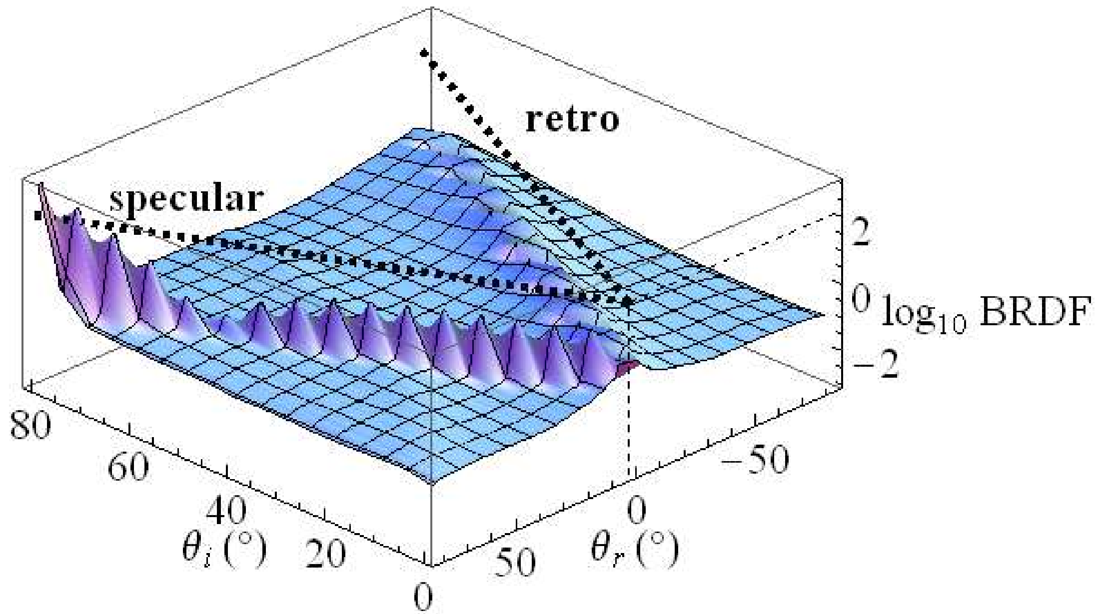

Figure 4.5: BRDF measurement of Telemecanique RF7590 reflective tape.

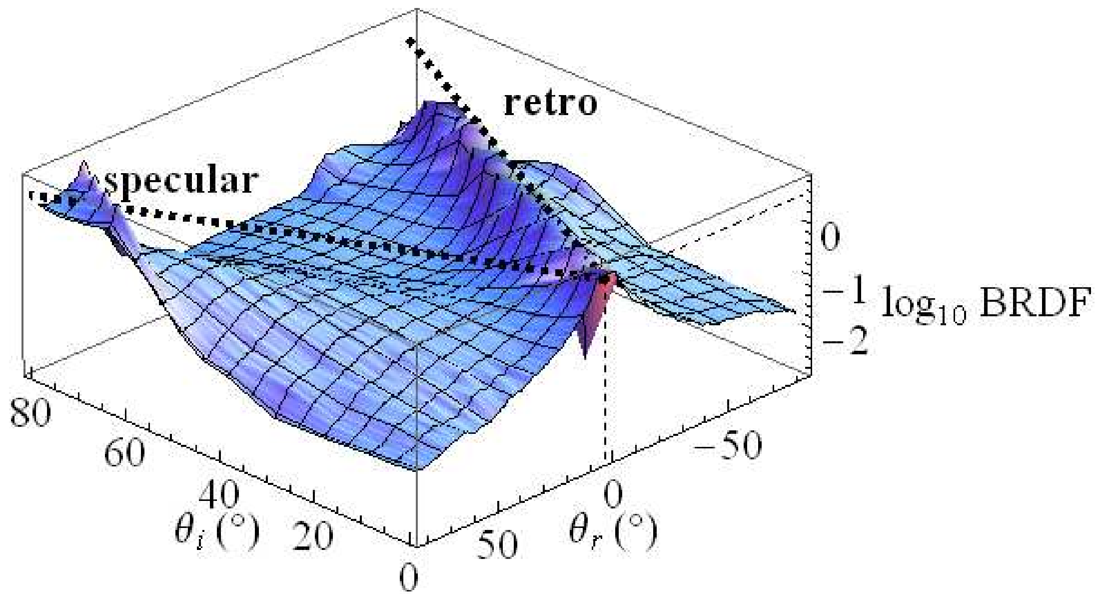

Figure 4.6: BRDF measurement of Telemecanique RF7610 reflective tape.

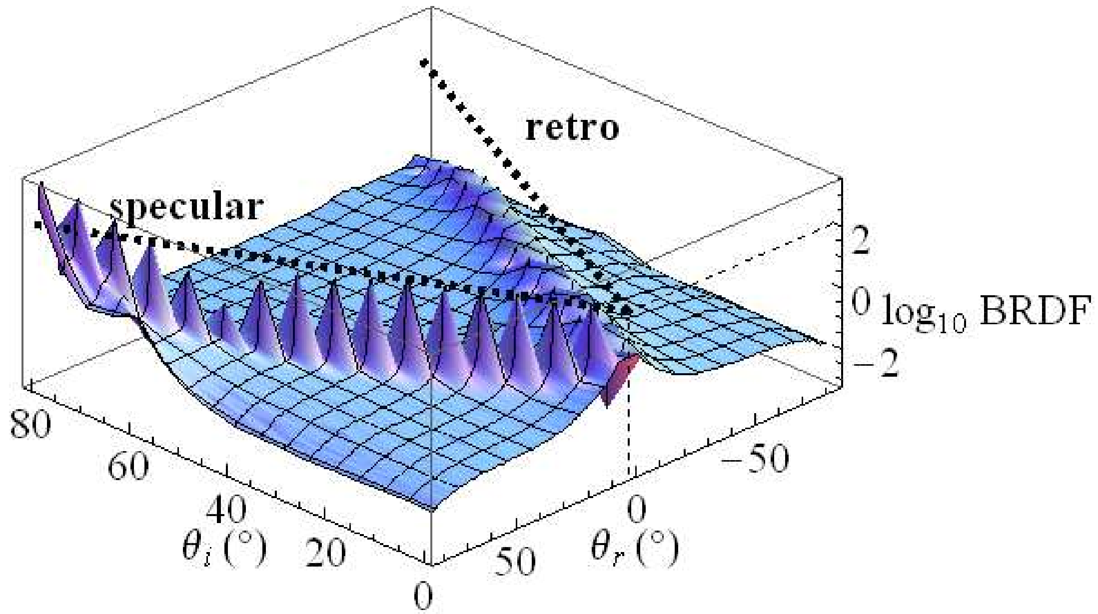

Figure 4.7: BRDF measurement of Telemecanique RF3870 reflective tape.

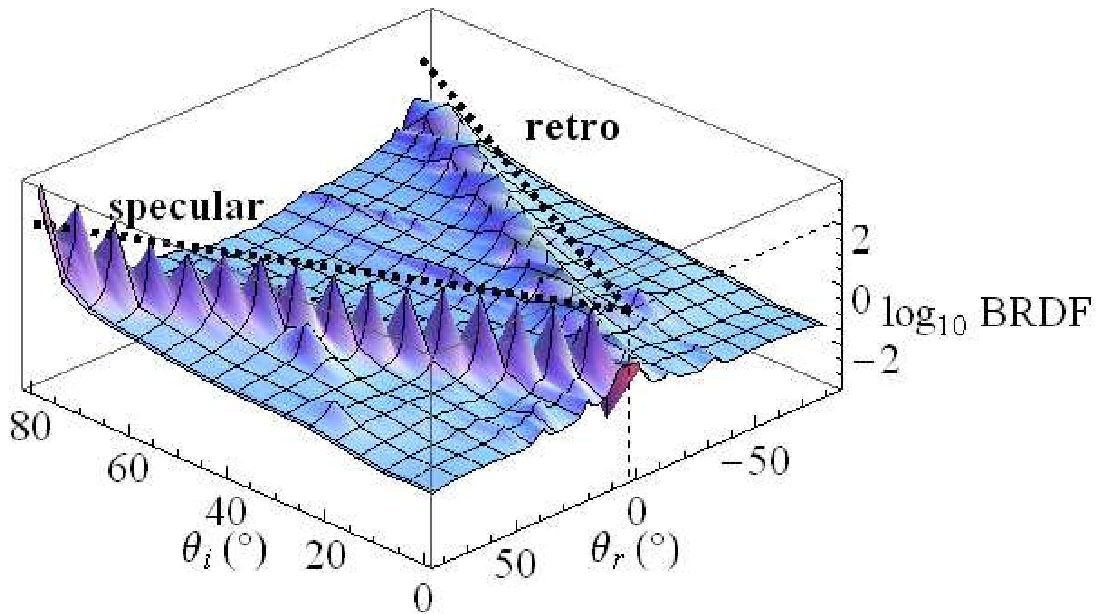

Figure 4.8: BRDF measurement of 3M 3000X reflective tape.

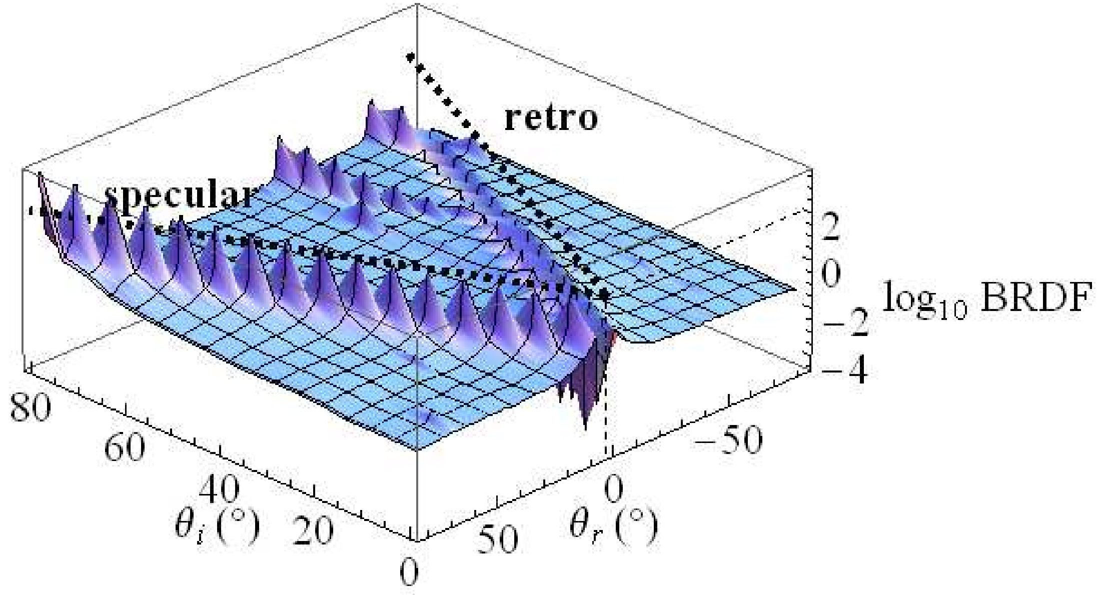

Figure 4.9: BRDF measurement of Telemecanique XUZB11 reflective tape.

protective coating while RF7610 does not. From Figure 4.10, it is apparent that this protective coating leads to a large specular reflection. This specular return appears to be significantly reduced at $\theta_r = 55°$. The reduced specular reflection at this particular angle is discussed in detail later.

4.4.2 BRDF of Gold Plated Reflector. The BRDF measurement of the gold plated RF30 reflector is seen in Figure 4.11. These results look similar to those of the corner reflector element tape samples. However, unlike the tape samples, there is no significant specular return.

Figure 4.12 shows density plots of the Telemecanique XUZB11 and gold plated RF30 samples. Once again, it is evident that the protective coating has resulted in large specular reflections for the XUZB11, while the RF30 sample has almost no specular reflection. However, there is significant "bloom" about $\theta_r = 0$ with the RF30. This is most likely due to the light transmitted through the gold plating. Once transmitted, the light bounces inside the reflector making it appear to glow.

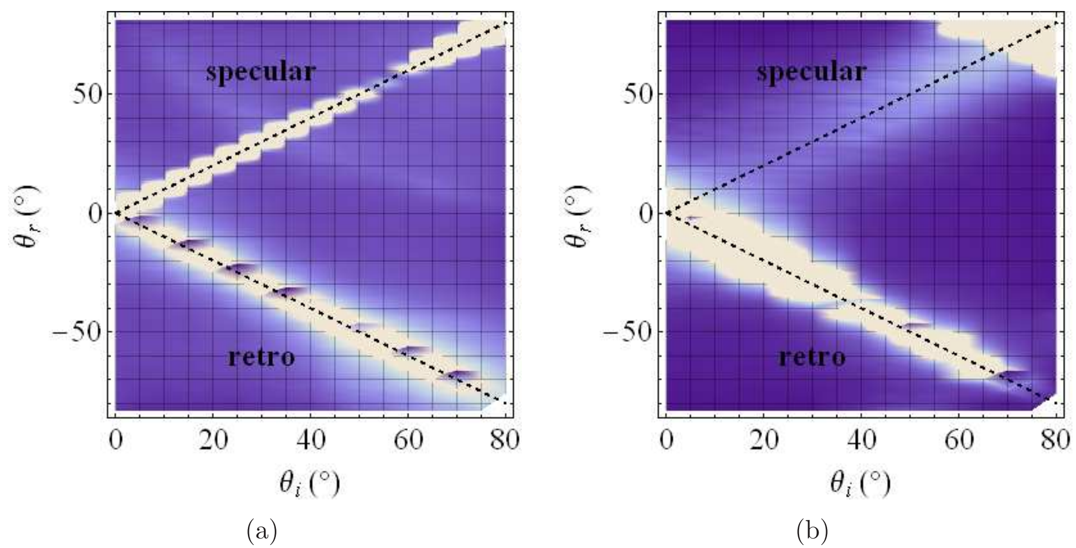

Figure 4.10: BRDF density plots of (a) Telemecanique RF7590 and (b) RF7610 retroreflective tapes. Although both tapes are made with spherical reflectors, RF7590 has a protective polymer coating which results in a larger specular reflection.

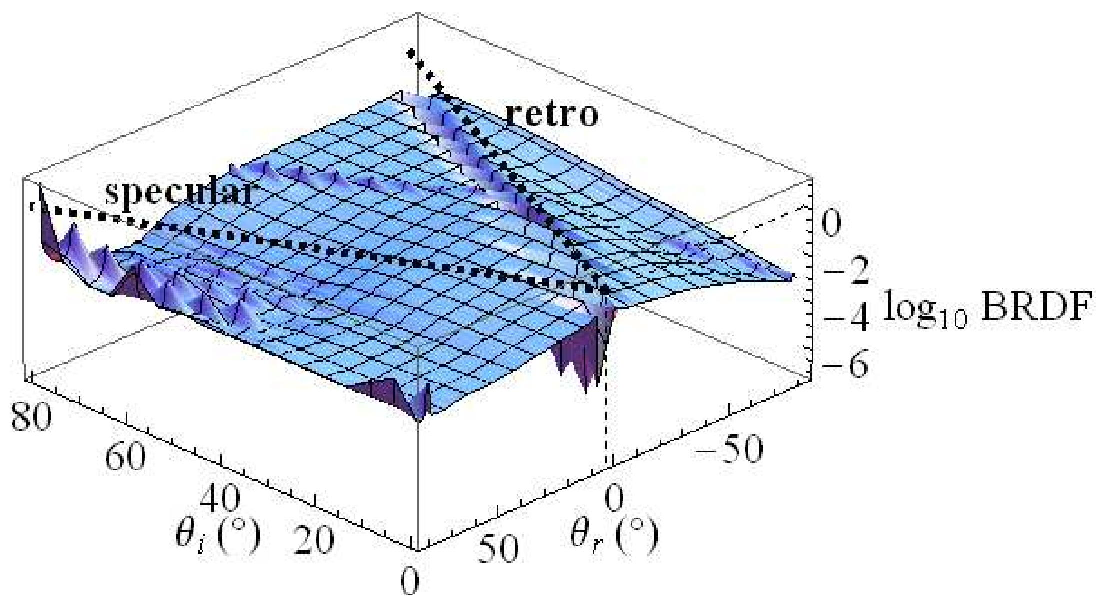

Figure 4.11: BRDF of Telemecanique RF30 reflector sputter-coated with gold.

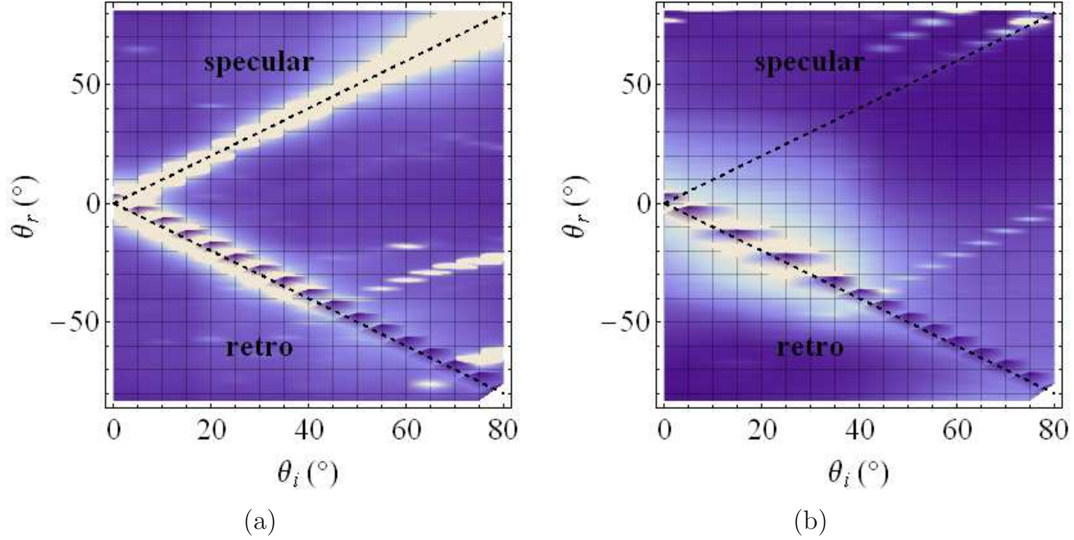

Figure 4.12: BRDF density plots of (a) Telemecanique XUZB11 reflective tape and (b) gold coated RF30 reflector. Although both the XUZB11 and the RF30 are made with corner reflectors, XUZB11 has a protective polymer coating which results in a larger specular reflection.

4.4.3 BRDF of PolyMUMPs^{TM} Corner Reflector. As mentioned previously, assembling an array of MUMPs© corner reflectors was not practical. A single assembled MUMPs© corner reflector was too small to be measured with the CASI. Therefore, no BRDF measurements were produced for the MUMPs© corner reflector.

4.4.4 BRDF of SOI Triangular Corner Reflectors. Fabrication of the SOI corner reflector array was not completed. No BRDF measurements for the SOI triangular corner reflectors were made.

4.5 Analysis of the Retroreflective Tape Protective Coatings

The reduced reflection at $\theta_r = 55°$ in Figure 4.10(a) can be described by Fresnel reflectance. When light travels from a medium with refractive index n_1 to a medium with refractive index n_2, reflection and transmission can occur. Reflectance, R, is the amount of power that is reflected at the interface, while transmittance, T, is the amount of power transmitted (R+T=1). Both reflectance and transmittance are dependent on the polarization of the incident light with respect to the interface. If the

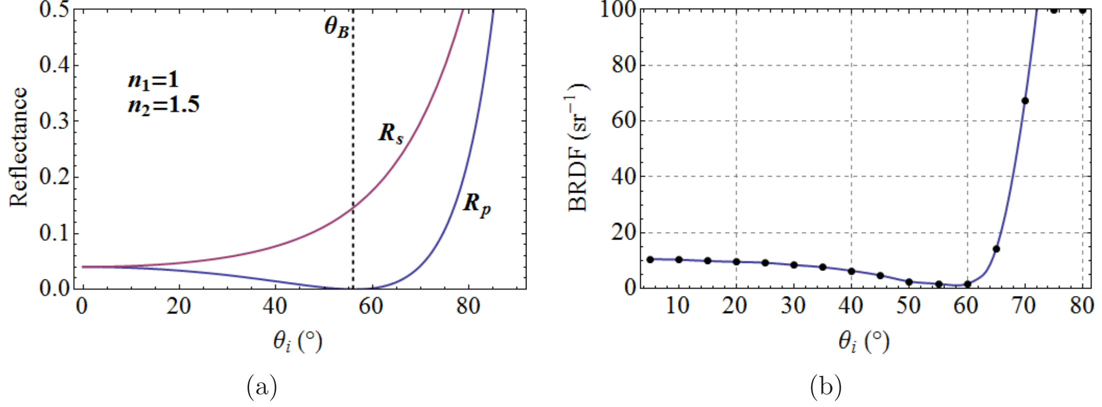

Figure 4.13: (a) Fresnel reflectance curves. (b) Maximum BRDF specular reflection curve for RF7590. The CASI laser used to measure BRDF for this test was p-polarized, resulting in a specular reflectance curve which resembles the Fresnel reflectance curve for R_p.

incident light is polarized with the electric field perpendicular to the interface plane, then it is s-polarized. The reflectance for s-polarized light, R_s, is given by

$$R_s = \left[\frac{n_1 \cos\theta_i - n_2 \sqrt{1 - (\frac{n_1}{n_2} \sin\theta_i)^2}}{n_1 \cos\theta_i + n_2 \sqrt{1 - (\frac{n_1}{n_2} \sin\theta_i)^2}} \right]^2 \tag{4.3}$$

where θ_i is the angle of the incident ray from the surface normal. If polarized with the electric field parallel to the interface plane, the light is p-polarized. The reflectance for p-polarized light, R_p is given by

$$R_p = \left[\frac{n_1 \sqrt{1 - (\frac{n_1}{n_2} \sin\theta_i)^2} - n_2 \cos\theta_i}{n_1 \sqrt{1 - (\frac{n_1}{n_2} \sin\theta_i)^2} + n_2 \cos\theta_i} \right]^2 \tag{4.4}$$

Unpolarized light is a combination of s- and p-polarized light with reflectance $R = (R_s + R_p)/2$. Figure 4.13(a) shows R_s and R_p as a function of incident beam angle for an interface where $n_1 = 1$ and $n_2 = 1.5$. For p-polarized light, the reflectance drops to zero at Brewster's angle, θ_B. This can also be seen in the specular return of the RF7590 sample, seen in Figure 4.13(b). This data shows that the CASI laser was p-polarized for these tests.

Table 4.2: Observed specular reflectance and corresponding indexes of refraction for retroreflective tape protective coatings ($\lambda = 544$ nm).

Sample	Observed Specular Reflectance at Normal Incidence (± 0.05%)	Index of Refraction (± 0.01)
Telemecanique RF3870	5.43	1.61
Telemecanique RF7590	1.58	1.29
Telemecanique XUZB11	3.17	1.43
3M 3000X	3.50	1.46

As the incident light approaches the surface normal ($\theta_i = 0$), the reflectance can be written as

$$R = R_s = R_p = \left(\frac{n_1 - n_2}{n_1 + n_2}\right)^2 \tag{4.5}$$

This equation can be used to determine the refractive index of the retroreflective tape protective coatings. An approximate value for R can be determined from the specular spikes seen at normal incidence in the OCS measurements. The specular reflected power is found by taking the power detected at normal incidence and then subtracting the power detected at $\theta_i = \pm\ 2°$. The total power incident upon the target sample can be modeled as the incident irradiance multiplied by the area of the sample ($\Phi_{tar} = E_{e-tar}\ A_{tar}$). The reflectance at normal incidence due to the reflective coating is then

$$R_{spec} = \frac{\Phi_{spec}}{\Phi_{tar}} = \frac{\Phi_{\theta_i=0} - \Phi_{\theta_i=\pm 2°}}{E_{e-tar}\ A_{tar}} \tag{4.6}$$

The index of refraction for the protective coating of a sample can then be found by solving Equation 4.5 for n_2. Table 4.2 shows the observed specular reflectance at normal incidence for each sample, as well as the corresponding refractive index for its protective coating. These values correspond to typical refractive indexes for polymers, which generally range from $n = 1.3$ to $n = 1.7$ [30].

4.6 Chapter Summary

This chapter presented the results of all tests performed on the retroreflectors discussed in this thesis. Curvature measurements of the MUMPs© mirrors (with and without the PolyMUMPs™ Metal layer) were displayed, as well as roughness measurements of the sputter coated gold and PolyMUMPs™ Metal layers. OCS and BRDF measurement data was then presented, which led to an analysis of the protective polymer coating used on most of the retroreflective tape samples.

V. Conclusions

This chapter presents the conclusions reached during this research. Included are thoughts on the manufacturing and testing methods used, as well as a recommendation as to which retroreflector solution best meets the sponsor's needs. In addition, suggestions for follow-on work in this area are provided.

5.1 Conclusions

Much of the work in this research was focussed on fabrication of the SOI corner reflector design. Fabrication was repeatedly delayed by unavailability of the DRIE at AFRL. The DRIE was installed at AFRL in November 2008, and took some time to configure and characterize. After this, the DRIE was generally unreliable, often etching through the oxide layer in the SOI wafers. These problems were resolved by the end of this research period, but only two wafers were successfully etched to create mirror structures in the device layer. Photoresist hinges were placed on these structures and then released. However, self-assembly of these devices did not occur.

The design of the SOI corner reflectors appears valid. With the DRIE now working properly, it would be possible to create and test more of these structures. Once assembled, a gold layer could be deposited on the SOI corner reflector array. The device could then be tested using the OCS and BRDF measurement techniques discussed in this thesis.

A MUMPs© corner reflector was successfully assembled, but the assembly process was difficult and time consuming. It would be unfeasible to create a MUMPs© corner reflector array large enough for use with the PDV. Additionally, the fabrication process is relatively expensive, and is often prone to manufacturing delays.

The optical testing performed in this research was successful, providing valid retroreflectivity measurements. Retroreflectivity information as a function of incident beam angle can be acquired using the OCS setup described in this thesis. The CASI scatterometer was also used to obtain BRDF measurements, which describe a sample's specular and diffuse components. In their current configurations, both the OCS and

BRDF test setups have shortfalls. The OCS setup only provides retroreflectivity data, while the BRDF setup provides everything but retroreflectivity data. However, performing both OCS and BRDF tests provides an accurate description of a sample's retro-, specular, and diffuse reflectivity.

Finally, the retroreflective tapes tested appear to offer an unbeatable mix of retroreflectivity and value. Unfortunately, the specular coating applied to most of these tapes render them unusable in a triaxial PDV setup. One tape sample, Telemecanique RF7610, did not have a protective coating. This tape provided a constant reflectance in the incident beam direction of approximately 20% over a range of ±25°. At the same time, the specular reflection from this tape was essentially zero. This makes it an optimal retroreflector for photonic Doppler velocimetry.

5.2 Follow-on Work

There are many ways in which this research can be expanded upon to provide a better retroreflector solution. First, additional retroreflective tapes without any type of protective coating should be investigated. As of now, these tapes offer the best combination of high retroreflectivity, minimal specular reflection, and low cost.

The SOI design could be improved in a number of ways. One modification can be borrowed from radar cross section measurement techniques. When calculating the expected radar echo from a triangular-faced trihedral, it is necessary to find its effective area. This effective area includes only portions of the surface that participate in the three-bounce effect of the corner reflector. When viewed normal to the axis of symmetry perpendicular to the trihedral aperture (normal to the wafer surface in the SOI design), the effective area is a hexagon [21]. Figure 5.1(a) shows an illustration of this effective area. This effect can be seen in the corner element retroreflective tapes as shown in Figure 5.1(b). In this microscope image, light can only be seen in the effective area of each corner reflector (the dark area in the center of each triangle is

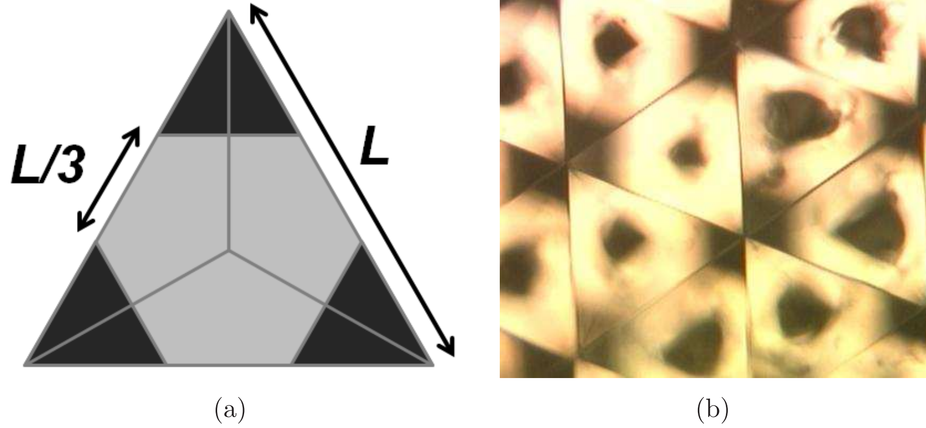

(a) (b)

Figure 5.1: (a) Effective area of a triangular-faced trihedral corner reflector when viewed perpendicular to the axis of symmetry. (b) The effective area can be witnessed in microscope images of the 3M 3000X retroreflective tape. The light from the microscope is only seen in the effective area of the corner reflectors.

due to deformation of the plastic corner tip). Removing these unlit corners in the SOI design would reduce the torque required to rotate the mirror plates out of plane.

An optimized size for the triangle anchor in the center of the SOI corner reflector is also needed. The anchor used in the current design was made large enough to ensure the photoresist hinges could supply more than enough torque to rotate the mirrors. However, this anchor reduces the effective area of the corner reflector by reducing the size of each rotating mirror. This anchor could be made smaller and still accommodate photoresist hinges large enough to supply the required torque. However, if the anchor is made too small it could detach during the release process.

The layout of the SOI corner reflector array could also be improved. The current array configuration was not designed to maximize the effective area of the array. The placement of individual corner reflectors could be optimized to increase the fill factor of the array. In addition, varying sizes of corner reflectors could be used, placing smaller corner reflector designs in open areas too small to fit a larger design.

Shock testing of a completed corner reflector array should be conducted. If the array is to be used in PDV measurements of small detonators, it will be exposed to

large acceleration pulses. The reflector array must not only survive these accelerations, but continue to provide accurate retroreflection to the PDV detectors. Modal analysis should also be performed to determine the properties of these corner reflectors under vibrational excitation. Robustness of the device might be improved by applying a thick layer of photoresist to the wafer after assembly of the corner reflectors. This photoresist could then be patterned so that only the mirror structures are visible. The remaining photoresist would help reinforce the existing structures.

Bibliography

1. Abel, N. J. *Effects of abberations on optical cross section measurements*. Masters thesis, Air Force Institute of Technology, 2004.
2. Arenberg, J. *Optical Cross Section Primer*. Technical Report 726210/294, Raytheon, February 1989.
3. Barker, L. M. and R. E. Hollenbach. "Laser interferometer for measuring high velocities of any reflecting surface". *Journal of Applied Physics*, 43(11):4669–4675, November 1972.
4. Barton, D. K. *Modern Radar System Analysis*. 1988. ISBN 089006170X, 9780890061701.
5. Bennett, J. M. and L. Mattsson. *Introduction to Surface Roughness and Scattering*. Optical Society of America, 1989. ISBN 1557521085.
6. Bowden, M. D., M. P. Maisey, W. J. Thomes, Jr., and F. M. Dickey. "The development of a heterodyne velocimeter system for use in sub-microsecond time regimes". *Optical Technologies for Arming, Safing, Fuzing, and Firing III*, volume 6662, 66620B–12. SPIE, San Diego, CA, USA, 2007.
7. Cahn, R. W., P. Haasen, and E. J. Kramer. *Materials Science and Technology: A Comprehensive Treatment*, volume 12. Wiley-VCH Verlag GmbH, 1993. ISBN 3527268138.
8. Dereniak, E. L. and G. D. Boreman. *Infrared Detectors and Systems*. Wiley-Interscience, April 1996. ISBN 0471122092.
9. Dollhous. "RIE Diagram", May 2007. URL `http://upload.wikimedia.org/wikipedia/en/c/c1/Riediagram.gif`.
10. Goldstein, J., D. E. Newbury, P. Echlin, C. E. Lyman, D. C. Joy, E. Lifshin, L. C. Sawyer, and J. R. Michael. *Scanning Electron Microscopy and X-ray Microanalysis*. 2003. ISBN 0306472929, 9780306472923.
11. Goodman, J. W. *Introduction to Fourier Optics*. Roberts & Company Publishers, 3rd edition, December 2004. ISBN 0974707724.
12. Guckel, H. "High-aspect-ratio micromachining via deep X-ray lithography". *Proceedings of the IEEE*, 86(8):1586–1593, 1998.
13. Haade. "Solid_Angle", February 2007. URL `http://commons.wikimedia.org/wiki/File:Solid_angle.png`.
14. He, X. D., P. O. Heynen, R. L. Phillips, K. E. Torrance, D. H. Salesin, and D. P. Greenberg. "A fast and accurate light reflection model". *Proceedings of the 19th annual conference on Computer graphics and interactive techniques*, 253–254. ACM, 1992. ISBN 0-89791-479-1. URL `http://portal.acm.org/citation.cfm?id=134073`.

15. Heller, A. *This Instrument Keeps the Beat*. Technical report, 2004.

16. Hodgin, R., C. May, R. Hanks, D. Hansen, T. Whitworth, and T. Strand. "Fabry-Perot / PDV Comparison", May 2007.

17. Hong, Y. K., R. R. A. Syms, K. S. J. Pister, and L. X. Zhou. "Design, fabrication and test of self-assembled optical corner cube reflectors". *Journal of Micromechanics and Microengineering*, 15(3):663–672, 2005. ISSN 0960-1317.

18. Hsu, V. S., J. M. Kahn, and K. S. J. Pister. "MEMS Corner Cube Retroreflectors for Free-Space Optical Communications". *University of California Publication*, 1–53, 1999.

19. Jaeger, R. C. *Introduction to Microelectronic Fabrication*. Prentice Hall, 2nd edition, October 2001. ISBN 0201444941.

20. Knott, E. F. *Radar Cross Section Measurements*. SciTech Publishing, 2006. ISBN 1891121553.

21. Knott, E. F., M. T. Tuley, and J. F. Shaeffer. *Radar Cross Section*. SciTech Publishing, 2nd edition, 2004. ISBN 1891121251.

22. Koester, D., A. Cowen, R. Mahadevan, M. Stonefield, and B. Hardy. "PolyMUMPs Design Handbook". *MEMSCAP*, 2003.

23. Lowry, M. E., N. E. Molau, P. D. Sargis, O. T. Strand, and D. Sweider. *Photonic doppler velocimetry*. Technical report, United States, 1999.

24. Macikunas, A., S. Haykin, and T. Greenlay. "Trihedral radar reflector", June 1989. U.S. Classification: 342/7 ; International Classification: H01Q 1518.

25. Maisey, M. P., M. D. Bowden, F. M. Dickey, and R. A. Beyer. "Characterization of detonator performance using photonic Doppler velocimetry". *Optical Technologies for Arming, Safing, Fuzing, and Firing IV*, volume 7070. SPIE, San Diego, CA, USA, 2008.

26. Mattopia. "Sputtering", November 2005. URL http://upload.wikimedia.org/wikipedia/en/7/72/Sputtering.gif.

27. May, G. S. and S. M. Sze. *Fundamentals of Semiconductor Fabrication*. Wiley, April 2003. ISBN 0471232793.

28. McMillan, C. F., D. R. Goosman, N. L. Parker, L. L. Steinmetz, H. H. Chau, T. Huen, R. K. Whipkey, and S. J. Perry. "Velocimetry of fast surfaces using Fabry–Perot interferometry". *Review of Scientific Instruments*, 59(1):1–21, 1988.

29. NASA. "UAVSAR - Instrument: Calibration", April 2007. URL http://uavsar.jpl.nasa.gov/rosamond.html.

30. Parker-TexLoc. "Refractive Index of Polymers/Haze Value", October 2008. URL http://www.texloc.com/closet/cl$_refractiveindex.html$.

31. Paschotta, R. "Encyclopedia of Laser Physics and Technology - interferometers, Mach-Zehnder, Michelson, Fabry-Prot, Common-Path", 2008. URL `http://www.rp-photonics.com/interferometers.html`.

32. Quest Research Corporation. *Standard Optical Augmentation Measurement Methodology*. Technical report, March 1986.

33. Rauwendaal, R. "BRDFs", 2004. URL `graphics.cs.ucdavis.edu/ bcbudge/ecs298_2004/BRDF.ppt`.

34. Rusinkiewicz, S. "Local Illumination, Reflection, and BRDFs", 2002. URL `www.cs.princeton.edu/courses/archive/fall02/cs526/lectures/radiometry.pdf`.

35. Starman, L. A. "Micro-Electro-Mechanical Systems (MEMS)", 2008.

36. Strand, O. T., L. V. Berzins, D. R. Goosman, W. W. Kuhlow, P. D. Sargis, T. L. Whitworth, D. L. Paisley, S. Kleinfelder, D. R. Snyder, and B. J. Thompson. "Velocimetry using heterodyne techniques". *26th International Congress on High-Speed Photography and Photonics*, volume 5580, 593–599. SPIE, Alexandria, VA, USA, March 2005.

37. Stringer, J. P. *The Air Force Institute of Technology (AFIT) Micro Electromechanical Systems (MEMS) Interferometric Gyroscope (MiG)*. Masters thesis, Air Force Institute of Technology, March 2000.

38. Sweatt, W. C, P. L Stanton, and O. B. Jr Crump. "Simplified Velocity Interferometer System for Any Reflector (VISAR) system". United States, 1990. ISBN SAND-90-2419C; CONF-900756–43;.

39. Syms, R. R. A., C. Gormley, and S. Blackstone. "Physical : Improving yield, accuracy and complexity in surface tension self-assembled MOEMS". *Sensors and Actuators A*, 88(3):273–283, 2001.

40. Syms, R.R.A. "Equilibrium of hinged and hingeless structures rotated using surface tension forces". *Journal of Microelectromechanical Systems*, 4(4):177–184, 1995. ISSN 1057-7157.

41. Syms, R.R.A. "Surface tension powered self-assembly of 3-D micro-optomechanical structures". *Journal of Microelectromechanical Systems*, 8(4):448–455, 1999. ISSN 1057-7157.

42. Syms, R.R.A. and E.M. Yeatman. "Self-assembly of three-dimensional microstructures using rotation by surface tension forces". *Electronics Letters*, 29(8):662–664, 1993. ISSN 0013-5194.

43. Syms, R.R.A., E.M. Yeatman, V.M. Bright, and G.M. Whitesides. "Surface tension-powered self-assembly of microstructures - the state-of-the-art". *Journal of Microelectromechanical Systems*, 12(4):387–417, 2003. ISSN 1057-7157.

44. Tien, C. H. and C. H. Lee. "Optical Properties of Surface Micromachining with Randomly Distributed Etch Holes". *Japanese Journal of Applied Physics*, 45:1015–1017, 2006. ISSN 0021-4922.

45. Ultrasil Corporation. "Ultrasil SOI Wafer Technology - Frequently Asked Questions", 2007. URL `http://www.ultrasil.com/cms.aspx?ID=4`.

46. Veeco Instruments Inc. "SPM Training Notebook", October 2003.

47. Wynn, C. "An Introduction to BRDF-Based Lighting". *nVidia Developer Relations*, 2005–05, 2001.

REPORT DOCUMENTATION PAGE	*Form Approved* *OMB No. 074-0188*

The public reporting burden for this collection of information is estimated to average 1 hour per response, including the time for reviewing instructions, searching existing data sources, gathering and maintaining the data needed, and completing and reviewing the collection of information. Send comments regarding this burden estimate or any other aspect of the collection of information, including suggestions for reducing this burden to Department of Defense, Washington Headquarters Services, Directorate for Information Operations and Reports (0704-0188), 1215 Jefferson Davis Highway, Suite 1204, Arlington, VA 22202-4302. Respondents should be aware that notwithstanding any other provision of law, no person shall be subject to an penalty for failing to comply with a collection of information if it does not display a currently valid OMB control number.
PLEASE DO NOT RETURN YOUR FORM TO THE ABOVE ADDRESS.

1. REPORT DATE *(DD-MM-YYYY)*	**2. REPORT TYPE**	**3. DATES COVERED** *(From – To)*
26-03-2009	Master's Thesis	June 2008 - March 2009

4. TITLE AND SUBTITLE

Retroreflector for Photonic Doppler Velocimetry

5a. CONTRACT NUMBER
DACA99-99-C-9999

5b. GRANT NUMBER

5c. PROGRAM ELEMENT NUMBER

6. AUTHOR(S)

Thomas J. Lagoski, Capt, USAF

5d. PROJECT NUMBER
07-141

5e. TASK NUMBER

5f. WORK UNIT NUMBER

7. PERFORMING ORGANIZATION NAMES(S) AND ADDRESS(S)

Air Force Institute of Technology
Graduate School of Engineering and Management (AFIT/EN)
2950 Hobson Way
WPAFB OH 45433-7765 DSN: 785-3636

8. PERFORMING ORGANIZATION REPORT NUMBER

AFIT/EO/ENG/09-02

9. SPONSORING/MONITORING AGENCY NAME(S) AND ADDRESS(ES)
Air Force Research Laboratory, Munitions Directorate, Fuzes Branch
306 W. Eglin Blvd., Bldg. 432
Eglin AFB, FL 32542-5430

POC: Dr. Jason Foley; DSN: 875-0584; email: jason.foley@eglin.af.mil

10. SPONSOR/MONITOR'S ACRONYM(S)
AFRL/RWMF

11. SPONSOR/MONITOR'S REPORT NUMBER(S)

12. DISTRIBUTION/AVAILABILITY STATEMENT

Approved for public release; distribution unlimited

13. SUPPLEMENTARY NOTES

14. ABSTRACT
In order to meet the goals of the Department of Defense (DoD) for smaller and more accurate weapons, the Munitions Directorate of the Air Force Research Laboratory (AFRL/RW) has numerous projects investigating the miniaturization of weapons and munition fuze components. One of these efforts is to characterize the performance of small detonators. The velocity of the flyer, the key component needed to initiate a detonation sequence, can be measured using a photonic Doppler velocimeter (PDV). The purpose of this research was to develop a microelectromechanical system (MEMS) device that would act as an optimal retroreflective surface for the PDV. Two MEMS solutions were explored: one using the PolyMUMPs^{TM} fabrication process and one in-house fabrication design using silicon on insulator (SOI) wafers. The in-house design consisted of an array of corner reflectors created using an SOI wafer. Each corner reflector consisted of three separate mirror plates which were self-assembled by photoresist pad hinges. When heated to a critical temperature (typically 140-160 °C), the photoresist pads melted and the resulting surface tension caused each mirror to rotate into place. The resulting array of corner reflectors was then coated with a thin layer of gold to increase reflectivity. Despite the successful assembly a PolyMUMPs^{TM} corner reflector, assembling an array of these reflectors was found to be unfeasible. Although the SOI corner reflector design was completed, these devices were not fabricated in time for testing during this research. However, the bidirectional reflectance distribution function (BRDF) and optical cross section (OCS) of commercially available retroreflective tapes were measured. These results can be used as a baseline comparison for future testing of a fabricated SOI corner reflector array.

15. SUBJECT TERMS
photonic Doppler velocimetry, retroreflector, etch hole diffraction, optical cross section (OCS), bidirectional reflectance distribution function (BRDF)

16. SECURITY CLASSIFICATION OF:			**17. LIMITATION OF ABSTRACT**	**18. NUMBER OF PAGES**	**19a. NAME OF RESPONSIBLE PERSON**
REPORT	**ABSTRACT**	**c. THIS PAGE**			Lt Col Ronald A. Coutu, Jr.
U	U	U	UU	114	**19b. TELEPHONE NUMBER** *(Include area code)* (937) 255-3636, ext7230; email: ronald.coutu@afit.edu

Standard Form 298 (Rev: 8-98)
Prescribed by ANSI Std. Z39-18